FATIGUE BEHAVIOR OF AN ADVANCED MELT-INFILTRATED SIC/SIC COMPOSITE WITH ENVIRONMENTAL BARRIER COATING AT 1200°C IN AIR AND IN STEAM

THESIS

Thaddeus M. Williams, B.S.

AFIT-ENY-MS-20-M-287

DEPARTMENT OF THE AIR FORCE
AIR UNIVERSITY

AIR FORCE INSTITUTE OF TECHNOLOGY

Wright-Patterson Air Force Base, Ohio

AFIT-ENY-MS-20-M-287

FATIGUE BEHAVIOR OF AN ADVANCED MELT-INFILTRATED SIC/SIC COMPOSITE WITH ENVIRONMENTAL BARRIER COATING AT 1200°C IN AIR AND IN STEAM

THESIS

Presented to the Faculty

Department of Aeronautical and Astronautical Engineering

Graduate School of Engineering and Management

Air Force Institute of Technology

Air University

Air Education and Training Command

In Partial Fulfillment of the Requirements for the

Degree of Master of Science in Material Science and Engineering

Thaddeus M. Williams, B.S.

March 2020

AFIT-ENY-MS-20-M-287

FATIGUE BEHAVIOR OF AN ADVANCED MELT-INFILTRATED SIC/SIC COMPOSITE WITH ENVIRONMENTAL BARRIER COATING AT 1200°C IN AIR AND IN STEAM

Thaddeus M. Williams, B.S.

Committee Membership:

Marina B. Ruggles-Wrenn, PhD
Chair

Thomas Eason, PhD
Member

Eric Jones, PhD
Member

Abstract

Advanced aerospace applications such as aircraft turbine engine components, hypersonic flight vehicles, and spacecraft reentry thermal protection systems require structural materials that have superior long-term mechanical properties under high temperature, high pressure, and varying environmental factors, such as moisture. Because of their low density, high strength and fracture toughness at high temperatures SiC fiber-reinforced SiC matrix composites are being evaluated for aircraft engine hot-section components. In these applications the composites will be subjected to various types of mechanical loadings at elevated temperatures in oxidizing environments. Because their constituents are intrinsically oxidation-prone, the most significant problem hindering SiC/SiC composites is oxidation embrittlement. Typically the embrittlement occurs once oxygen enters through the matrix cracks and reacts with the fibers and the fiber coatings. The degradation of fibers and fiber coatings is generally accelerated in the presence of moisture. Environmental Barrier Coatings (EBC) were developed specifically to address degradation of CMCs due to oxidation by protecting the composite surface from the oxidizing environment. Before ceramic matrix composites with EBCs can be used in aerospace applications, their structural integrity and long-term environmental durability must be assured. A thorough understanding of the mechanical behavior of the candidate CMC with EBC at relevant service temperatures is critical to design with and life prediction for these materials. Tension-tension fatigue performance of a SiC/SiC composite with an EBC was investigated at 1200°C in laboratory air and in steam. The composite has a melt-infiltrated (MI) matrix consolidated by combining CVI-SiC with

SiC particulate slurry and molten Si infiltration and is reinforced with laminated woven SiC (Hi-Nicalon™) fibers. The EBC consists of a Si bond coat (targeted at 127 μm) and an Ytterbium disilicate ($Yb_2Si_2O_7$) top coat (targeted at 254 μm). The EBC was applied via Air Plasma Spraying (APS). Basic tensile properties of the composite with the EBC were evaluated at 1200°C. Tension-tension fatigue was examined for maximum stresses ranging from 110 to 140 MPa in air and in steam. To assess the efficacy of the EBC, experimental results obtained for the coated composite are compared to the results obtained for a control composite without the EBC. The presence of the EBC had a moderately beneficial effect on the composite performance. Fatigue run-out defined as survival of 200,000 cycles was achieved at 120 MPa in air and in steam for the EBC containing composite, but only at 110 MPa for the uncoated CMS. The retained properties of all specimens that achieved fatigue run-out were characterized. Composite microstructure, as well as damage and failure mechanisms were investigated. A sharp decrease in cyclic lifetimes with increasing maximum stress observed for both the coated CMC and the control CMC is attributed to significant processing defects present in both composites.

Acknowledgments

I would like to thank Dr. Marina Ruggles-Wrenn for her passion for science, dedication to discovery, and wisdom in teaching. This research would not have been possible without her composite expertise and material testing and evaluation guidance. I would also like to thank Mike Ranft and Jamie Smith for their support in the advanced materials testing laboratory along with Major Ryan Kemnitz and Mike Velez for their microscopy support and training.

Table of Contents

List of Figures

List of Tables

FATIGUE BEHAVIOR OF AN ADVANCED MELT-INFILTRATED SIC/SIC COMPOSITE WITH ENVIRONMENTAL BARRIER COATING AT 1200°C IN AIR AND IN STEAM

Chapter 1 Introduction

1.1 Background

Modern and future aircraft jet engines require increased thermal efficiency to extract the necessary energy during fuel consumption for high velocity flight. One way of improving engine efficiency is through the increase of the turbine's temperature gradient or the difference between the hottest and coldest temperatures in the engine during operation. The deficiencies of nickel-based superalloys or high-performance alloy materials in turbine engine technologies has grown apparent as modern turbine engine hot section operating temperatures exceed these material's stable operating ranges. Any additional cooling to the current systems to prevent melting of the superalloys would detrimentally lower the thermal gradient of the engine. For this reason, novel high temperature materials which do not require extensive cooling are necessary for the improvement of turbine engine technologies.

Ceramic matrix composite (CMC) materials have been developed as successors to superalloys. These composites maintain their properties at high temperatures due to the nature of the constituent ceramic materials while also benefiting from a reinforcement phase which increases toughness compared to a monolithic or bulk ceramic. Figure 1.1 shows general regions of operating temperatures and specific strengths for comparison of superalloys, CMCs, and various other materials. The weak bonding between the matrix

and reinforcement phases of CMCs prevents brittle, catastrophic failure exhibited in a bulk ceramic due to deceleration of crack propagation and a simulated ductile region caused by matrix failure prior to reinforcement failure.

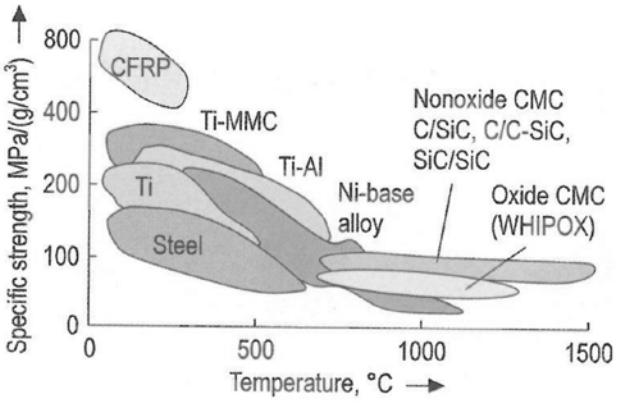

Figure 1.1: Material Strengths at Various Temperatures - Specific strength comparison between a variety of materials including nickel-based superalloys and CMCs in terms of operating temperature ranges [1]

The complexities of composite production compared to alloy or monolithic ceramic production lend these materials to extensive characteristic variation between processing techniques. Each variation of material constituent and processing technique must be characterized to adequately understand the composite. Additionally, due to oxidation-prone constituents which hinder the composite through oxidation embrittlement and surface recession, environmental barrier coatings have been developed to protect the composite surface. This research has been limited to identification and characterization of a single CMC composed of silicon carbide matrix and Hi-Nicalon^{TM} silicon carbide reinforcement fibers processed through melt-infiltration (SiC/SiC – MI) with a boron nitride (BN) interphase for weak fiber-matrix bonding. Additionally, the specimens have been grit-blasted and coated with a silicon (Si) bond coat and an ytterbium disilicate ($Yb_2Si_2O_7$) environmental barrier coating. Ten EBC/Hi-N/MI-SiC specimens were

subjected to cyclic fatigue testing at various maximum stress levels to determine fatigue life of the specimens in air and steam at 1200°C along with the retention of tensile properties if run-out (200,000 cycles) was achieved. This data was compared to prior research on a set of identical but uncoated CMC specimens.

1.2 Material Selection

A SiC/SiC composite was selected for research due to the thermal, mechanical, and chemical stability of silicon carbide. Thermally, as shown in Figure 1.1, this CMC maintains adequate strength at elevated temperatures which surpasses competing materials. Mechanically, the composite exhibits a nearly ductile region prior to failure despite a fully ceramic composition. This stems from the prevention of instantaneous catastrophic failure through crack prevention. Chemically, silicon carbide creates a natural protective oxidation layer at high temperatures but suffers from oxidation degradation at temperatures below 1000°C [2]. To stymie this material degradation, an EBC was applied to all specimens composed of a 5 mil Si bond coat and a 10 mil $Yb_2Si_2O_7$ topcoat. Application of the coating may have other benefits such as filling pores remaining from the melt-infiltration process. The EBC is assumed to maintain a uniform dry film thickness and infinitesimal load carry. Finally, SiC has a high strength to density ratio which is ideal for any aircraft application due to weight reduction without sacrificing strength [3].

The melt-infiltration processing technique is performed by passing a slurry of the matrix material, in this research SiC, through a fiber preform weave which composes the reinforcement phase. The matrix is then consolidated, and pores are removed through hot

pressing to complete fabrication. The primary benefit of melt-infiltration is matrix formation through a single processing step which leads to lower costs [4].

1.3 Research Methodology

The results produced in this thesis are from qualitative experimental research methods. Namely, tension-tension cyclic fatigue testing was performed on all specimens to determine fatigue life at an elevated temperature using a tensile test apparatus and furnace. Cyclic fatigue testing is performed by cycling maximum and minimum constant stress levels to the material specimen until failure through fracture or 200,000 cycles referred to as run-out [5]. Tension-tension loading means that the maximum and minimum stresses are both greater than zero; this testing technique is used due to the poor performance of composites under compression. Figure 1.2 illustrates the cyclic loading nature of tension-tension testing with a sinusoidal load application. Fatigue strength is determined as the stress amplitude corresponding to a number of cycles [5].

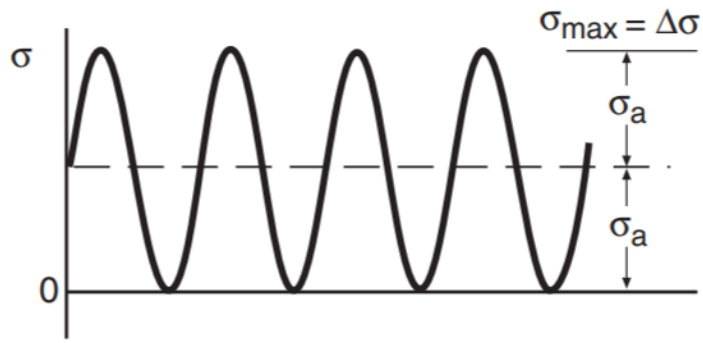

Figure 1.2: Cyclic stress application schematic for tension-tension fatigue testing [5]

The material test specimens were produced in the shape of a dog bone as shown in Figure 1.3. This shape is used to provide gripping areas on the ends where stress concentrations will be localized and prevented from impeding on the gage section in the center. If failure is reached, it will occur in the gage section.

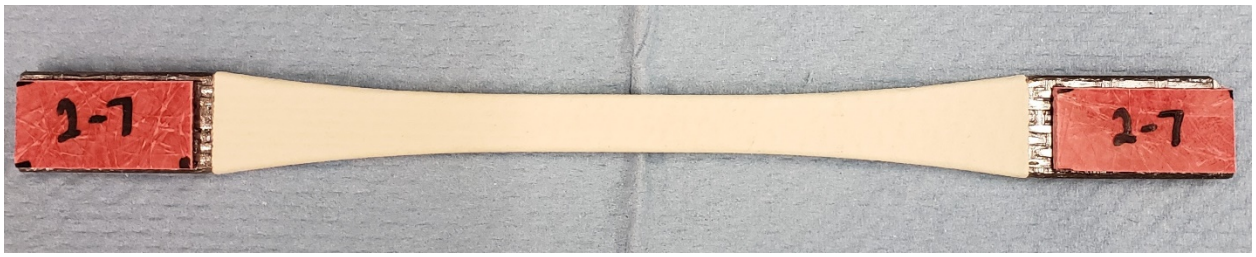

Figure 1.3: Dog bone shaped specimen used in fatigue testing.

Data during testing is collected and stored by the tensile test machine's controlling computer and associated sensors. This data includes time, cycles, temperature, temperature command, strain, load, load command, and displacement. From the measured data and the results calculated from this data, failure fatigue curves were generated for comparison to competitive materials. If fatigue failure did not occur after 200,000 cycles, a monotonic tension test to failure was performed which provided further data on retained tensile properties after cyclic loading. Following data collection, the specimens were examined through observation to determine failure mechanisms, oxidation, and microcracking primarily using scanning electron microscopy.

Chapter 2 Literature Review

2.1 Introduction

Ceramic matrix composite (CMC) materials, such as the ones used in this experimental research, are complex combinations of materials which require background, understanding of materials science principles, and previous research to grasp the experimental justification and data analysis in the following chapters. The materials described herein are relevantly reported in increasing complexity to develop a clear understanding of the composite tested during this research, EBC/Hi-N/MI-SiC. Finally, a description and summary of previous research on closely related composite materials is presented at the end of this chapter. The scope was limited to CMCs of similar construction, processing, and components.

Preliminary Definitions

Constituent – a distinct phase making up a portion of a composite material.

Matrix – a composite constituent made up of a continuous uniform phase [5].

Reinforcement – a composite constituent composed of continuous or discontinuous fibers/whiskers bound together by the matrix phase [5].

Crystal Lattice – a distinct arrangement of atoms held together by interatomic forces.

Thermal Expansion Coefficient – a constant coefficient that expresses the extent of a material to expand while subjected to temperature.

2.2 Engineering Ceramics

Engineering ceramics are ceramic materials used in technical applications such as high temperature structural load bearing systems and aerospace system development

industries [6]. They are often composed of simple combinations of metals, metalloids, and inorganics such as aluminum, silicon, carbon, nitrogen, oxygen, and boron.

Ceramics have multiple beneficial properties that make them candidates for use as composite constituents. Often considered the most important benefit, engineering ceramics are excellent at maintaining their material properties at elevated or extreme temperatures. The strong ionic-covalent bonding of light atoms allows for high frequency atomic vibrations with minimal change in the crystal lattice leading to high melting temperatures [7]. Additionally, the chemical stability or inertness of these materials provides corrosion and oxidation resistance resulting in the retardation of material degradation [8]. Finally, the high hardness and strength of ceramics leads to excellent wear and abrasion resistance [9].

The prevalent use of bulk ceramics in all technical applications is stymied by the detrimental properties of these materials. Ceramics are extremely brittle; the ionic bonding of ceramics prevents large-scale dislocation motion causing these materials to exhibit catastrophic brittle failure when the ultimate tensile strength is reached. Dislocation motion is the movement of line defects in the atomic crystal structure which causes plastic deformation or geometry alteration that remains after the applied stress is removed [5]. The directionality of bonding exhibited by silicon, other intermetallic compounds, and ceramics prevents dislocation motion except when the material is operating above half of its melting temperature where minor dislocation motion occurs [5]. A schematic of a dislocation in the atomic structure is shown in Figure 2.1.

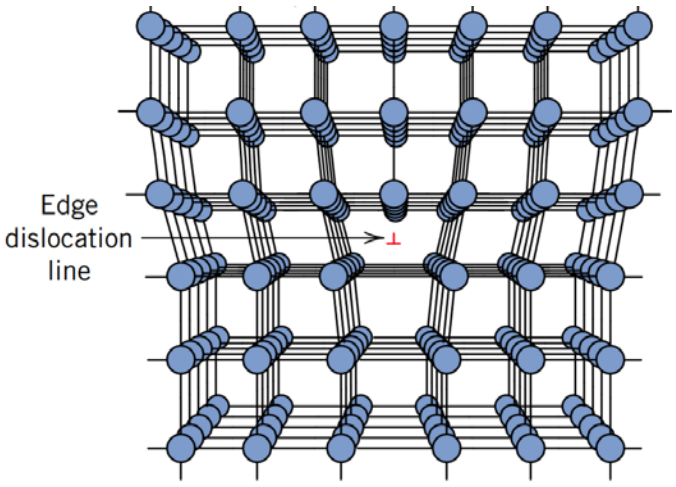

Figure 2.1: Edge Dislocation Schematic - A schematic of the atomic crystal lattice deformation due to a half-plane dislocation of atoms. Dislocation motion is essential for plastic deformation not found in bulk ceramics [10]

Due to the low ductility of engineering ceramics, they have a low fracture toughness compared to metals used in similar applications. Since there is no plastic deformation to operate as a crack diversion mechanism, small voids and flaws act as stress raisers or points of stress amplification which decrease the ceramic's ability to resist fracture also referred to as fracture toughness [10]. Equation 2.1 mathematically represents fracture toughness where Y is a dimensionless geometric parameter, σ is applied stress, and a is the length of a surface crack.

$$K_{I_c} = Y\sigma\sqrt{\pi a} \qquad (2.1)$$

Advanced ceramics are processed in a pure state that cannot occur naturally, which allows for refinement of material properties over their unrefined counterparts. Some of these fabrication techniques include hydroplastic forming, slip casting, and powder pressing. Hydroplastic forming is an extrusion process which geometrically forms the ceramic system by forcing the material through a die orifice and densifying

through removal of air in a vacuum [10]. Slip casting is performed by layering a mold with a ceramic/water suspension until the desired layer thickness is achieved and the water has been absorbed by the mold [10]. Powder pressing occurs when a powdered ceramic mass of coarse and fine particles is compacted with a binder at high temperatures to create the desired shape and minimize void space [10].

2.3 Composites

A composite is the combination of two or more distinct phases which are bonded together while maintaining their integrity. They often exhibit properties superior to the individual parts or constituents. The variety in matrix, reinforcement, processing technique, and constituent materials allows composites to be used in highly specific applications. There are three constituents which compose the composite. The first and second components are identified as a continuous uniform matrix phase surrounding a dispersed reinforcement phase. A third constituent, which is not always present, is an interphase between the reinforcement and the matrix [5]. As seen in Figure 2.2, the reinforcement phase can take on various forms primarily particulates, continuous fibers/whiskers, or discontinuous fibers/whiskers. Due to the directionality of the reinforcement phase, composites have varying levels of anisotropy. General anisotropy can be defined as a material without any symmetric planes of properties. Accordingly, particulates are the least anisotropic and unidirectional continuous fibers are the most anisotropic.

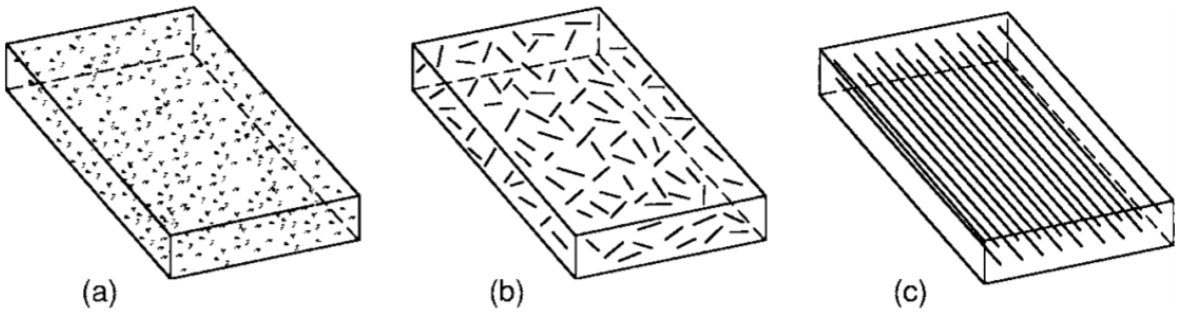

Figure 2.2: Composite Reinforcement Schematic - Composites reinforced by (a) particles, (b) chopped fibers or whiskers, and (c) continuous fibers [5]

Not all composite types exhibit the same benefits. Polymer-matrix composites (PMC) are created to increase polymer strength by transferring load to the reinforcement phase composed commonly of glass, carbon, or aramid. To transfer the load to the fibers and increase the tensile strength of the composite, a strong bonding between the reinforcement and matrix phase must be present. Metal-matrix composites (MMC) increase the viable operating temperature that an individual metal would fail to withstand while also increasing toughness, specific strength, creep resistance, and thermal conductivity [10]. Ceramic matrix composites (CMC) are manufactured to increase ceramic toughness. A weak bond between matrix and fiber increases the fracture toughness of the ceramic by slowing catastrophic failure through energy dissipating mechanisms.

Within composites, bundles of reinforcement fibers referred to as tows are woven together to create various types of weaves such as plain or satin as shown in Figure 2.3. The lengthwise tow is referred to as the warp while the transverse tow is the weft or fill. Depending on the weave, different properties may be present. For instance, a plain weave exhibits little slippage and uniform strength while also suffering from porosity.

Alternatively, a satin weave exhibits pliability for use with complex geometry [4]. The weave is stacked in multiple layers or plies to complete the reinforcement construction.

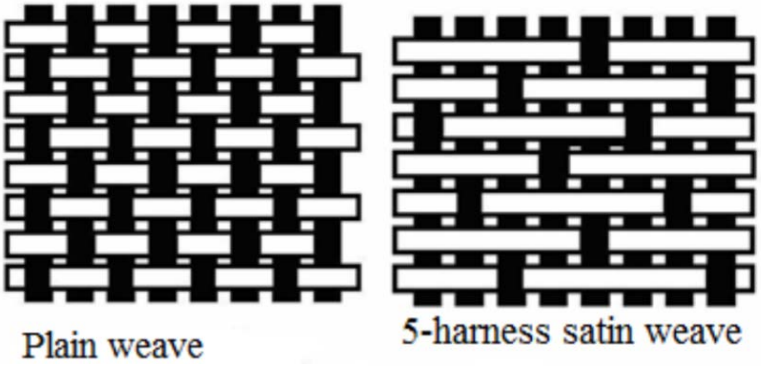

Figure 2.3: Fiber Reinforcement Weaves - Two examples of reinforcement weaves: plain and satin [11]

2.4 Ceramic Matrix Composites

A ceramic matrix composite (CMC) is a classification of composite which contains both matrix and reinforcement phases of ceramic materials. Advanced ceramics such as oxides, nitrides, and carbides of various elements are used to create CMCs as opposed to the conventional ceramics like brick and tile [4]. As ceramic materials are the only viable options for high-temperature application, they are specifically prevalent in the aerospace industry. CMCs were developed with the benefit of high temperature structural application of ceramics and the increased fatigue strength of composites [12], [13]. Additionally, CMCs have low density, thermal expansion coefficient, and thermal conductivity [4]. The thermal expansion coefficient is a value that represents how a material will expand following heating. Ceramics detrimentally exhibit low fracture toughness; a key aspect of the development of CMCs is to increase material toughness while maintaining excellent property retention at elevated temperatures. By increasing fracture toughness, catastrophic failure of the material is minimized [4]. The low

toughness of ceramics increases the sensitivity of the material to flaws such as cracks and voids which lowers the overall strength of the material [4]. These flaws occur due to processing, design, and service. The reinforcement phase of CMCs is not intended to increase strength which is why CMCs often have similar or identical matrix and reinforcement phases. Rather, the fiber is intended to slide in the matrix to decrease the strain energy release and exhibit a quasi-ductile behavior.

The interface between matrix and fiber critically dictates the behavior a CMC will exhibit. A weak bonding between fiber and matrix in a CMC is beneficial to prevent cracks in the matrix from propagating through the fibers like a bulk ceramic material [14]. Ideally, an initiated crack in the matrix progresses around the fiber and leaves the fiber intact as opposed to immediately bridging the fiber-matrix interface and continuing through the fiber [4], [15]. This phenomenon leads to a non-catastrophic failure as seen in Figure 2.4. The weak interface bond leads to energy-absorption mechanisms beyond crack propagation and brittle failure including debonding, crack deflection, crack bridging, fiber fracture, and fiber pullout [4]. All these phenomena increase the fracture toughness of the material.

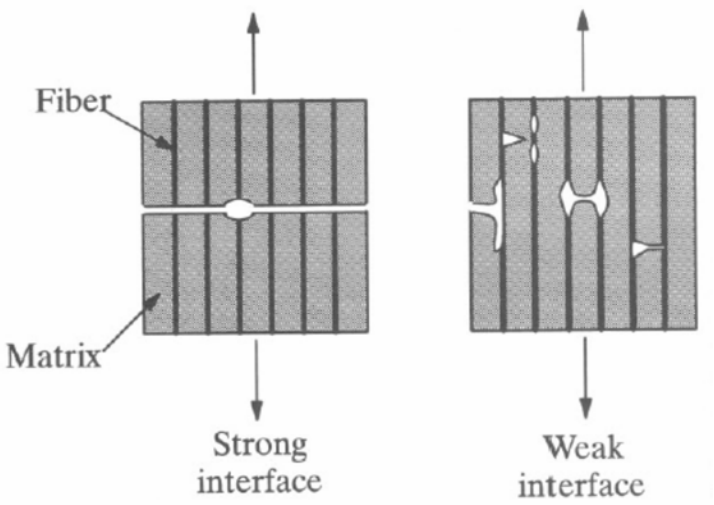

Figure 2.4: Composite Interfaces - Schematic of composites with differing strong and weak interfaces. A strong bonding leads to catastrophic failure of the material while a weak bonding exhibits more energy dissipating mechanisms prior to failure [4]

An alternative to a weakly bonded interface is the addition of a third phase between dense matrix and reinforcement, the interphase. An interphase like boron nitride (BN) is applied as a fiber coating which affects the energy release mechanisms of crack deflection and propagation. The interphase causes a double deflection of the propagating crack as it passes through the matrix and the interphase before reaching the fiber. Improved crack deflection occurs in a composite material when the interface between the reinforcing fiber and interphase has a low toughness [16].

There are many variations of fabrication techniques for CMCs but only the two most relevant processes for this research will be discussed – chemical vapor deposition (CVD) and melt infiltration (MI). When CVD is used to impregnate matrix material into fibrous preforms, layers of stacked woven plies, it is referred to as chemical vapor impregnation (CVI). A compound in vapor form decomposes around a heated fibrous preform and deposits the material as solid phases on and around the fibers [4]. As it is based on diffusion, CVI is a slow process and forces closure of surface pores on the

substrate preventing complete infiltration. This leads to a decrease in matrix density which is detrimental to the overall composite strength [4]. Melt Infiltration (MI) of silicon carbide matrices is performed through the introduction of silicon slurry into a woven preform at elevated temperatures to infiltrate the preform and react with carbon to create the matrix [17]. The initial preform is molded in an autoclave and then pyrolyzed or decomposed at a high temperature into a porous preform. Finally, a molten silicon slurry is passed into the pores by capillary forces to build the SiC matrix [17]. Depending on the constituent types and materials used, the microstructure of the MI composite varies significantly as seen in Figure 2.5.

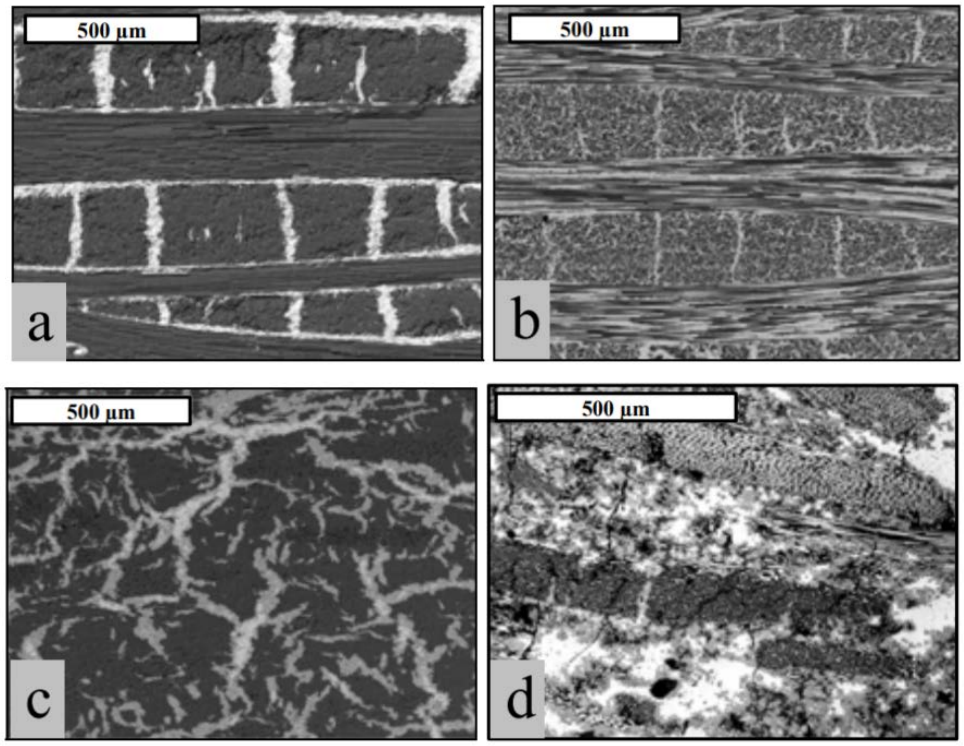

Figure 2.5: Composite Microstructure Microscopy - Microstructure of various MI fabricated composites (a) fabric based C/C-SiC imbedded in SiC matrix (b) high density C/C-SiC (c) short fiber C/C-SiC (d) short fiber Sigrasic 6010 [17]

The benefits of MI are the single processing step to create the matrix and the homogeneous matrix obtained following completion of fabrication. Unfortunately, there are also downsides to MI. First, the high melting temperatures of ceramics increases the likelihood of chemical reaction between the slurry and the reinforcement. Second, the high melt viscosities of ceramics increase the difficulty of slurry infiltration in the porous preform. Third, if constituent materials of varying thermal expansion coefficients are used, the preform is likely to crack from shrinkage when the processing heat is removed. This can be remedied by using similar or identical compounds for reinforcement and matrix [4].

2.5 Environmental Barrier Coating

As the primary development purpose of CMCs such as SiC/SiC-MI composites are for structural application at elevated temperatures, environmental barrier coatings (EBC) are implemented on the surface of the CMCs for protection against oxidation and adverse environmental effects. At ambient temperatures, a naturally occurring layer of Silica (SiO_2) develops on SiC which provides excellent oxidation resistance [18]. However, at elevated temperatures, silicon-based composites suffer from volatilization of silica in the presence of water vapor and therefore exhibit rapid surface recession [19]. EBCs are necessary to prevent oxidation and recession as hot sections of turbine engines continue to increase in temperature and pressure with increasing efficiency.

Prominent 1st generation EBCs developed by NASA for SiC/SiC CMCs are composed of silicon mullite and barium strontium aluminasilicate (BSAS). The density and chemical compatibility of silicon mullite with SiC improves the adhesion properties of the BSAS topcoat which is more porous and has superior crack resistance [18]. Although this EBC is a successful protection scheme for SiC/SiC composites, 2nd generation EBCs have been developed with improved characteristics for operating at higher temperatures.

The 2nd generation EBCs composed of monosilicates and disilicates that are applied to modern CMCs benefit from chemical compatibility and similar coefficients of thermal expansion (CTE) to SiC along with high melting points. Monosilicates are more recession resistant than disilicates but are more prone to cracking from thermal cycling due to higher CTEs [18]. These EBCs are usually applied as topcoats over silicon bond coats. Silicon is used as a bond coat because it undergoes less oxidation damage than SiC

and therefore provides additional protection to the composite [20]. The primary issue with 2nd generation EBCs is due to spallation that occurs when H_2O passes through the topcoat and reacts with the silicon bond coat to create an SO_2 thermally grown oxide (TGO) [18]. Figure 2.6 displays the TGO formation on a micrograph of an EBC composed of an $Yb_2Si_2O_7$ topcoat and a Si bond coat.

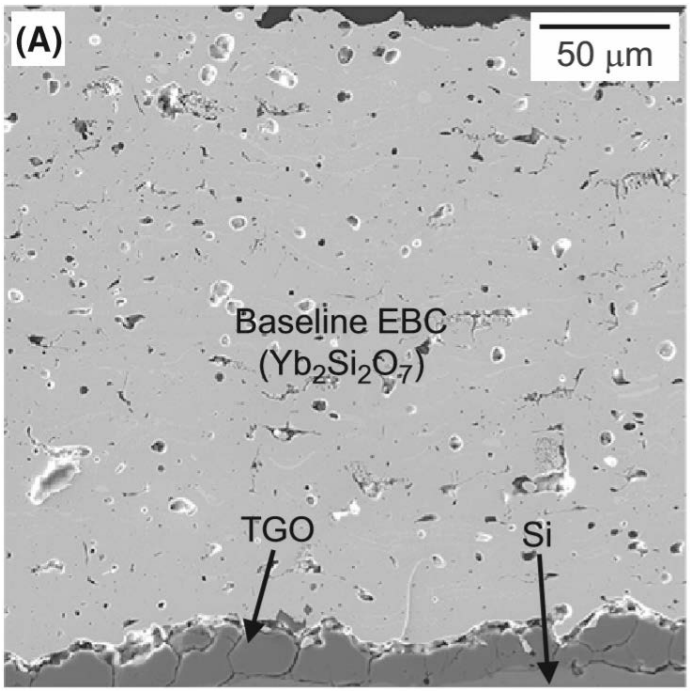

Figure 2.6: EBC Micrograph - TGO formation on a micrograph of an EBC composed of an $Yb_2Si_2O_7$ topcoat and a Si bond coat [21]

Along with providing increased stability of the CMC exposed to harsh environments, it is also hypothesized that the application of an EBC may fill surface flaws in excessively porous CMCs to increase the strength and toughness of the material.

2.6 Previous Research

Research on SiC/SiC ceramic matrix composites has been completed in the past using a similar methodology outlined in this document. Like the current research,

SiC/SiC CMCs of various fabrication techniques and coating applications were mechanically tested under fatigue to determine performance characteristics.

Investigations of Hi-Nicalon/SiC-B_4C composites processed through chemical vapor infiltration were performed by Delapasse [22] and Lee [23]. This composite consisted of a variant of SiC fibers, Hi-Nicalon, in an eight-harness satin weave surrounded by a matrix of alternating layers of silicon carbide and boron carbide. The boron carbide layers were intended to prevent oxidation of the matrix. This matrix employs self-healing through the creation of fluid oxides when exposed to oxygen which leads to crack sealing and oxygen entrapment in glassy phases that do not impede the fibers. The weak bonding between matrix and reinforcement was ensured by coating the fiber preforms with a carbon coating to decrease bond strength. Delapasse [22] researched tension-tension fatigue testing of the composite at 1200°C in air and in steam while Lee [23] performed similar experimentation at an elevated temperature of 1300°C. A summary of the results of this research is found in Table 2.1.

Further research by Christensen [24] was performed as high temperature tensile test experimentation on a different SiC/SiC CMC that was also processed through CVI. This composite used a fiber coating of boron nitride (BN) to adequately weaken the bonding of fiber and matrix. Additionally, fatigue testing at 1200°C air and steam was conducted on this composite at varying loading frequencies. It was concluded that the failure mechanism of these composites in air and in steam originated from oxidation-assisted cracking of the matrix. A summary of the results of this research is found in Table 2.1.

Boucher [25] performed high temperature fatigue testing at 1200°C on a melt infiltrated SiC/SiC CMC that is identical to the material used in this document's research apart from an environmental barrier coating. Once again, this composite contains a reinforcement of Hi-Nicalon SiC fibers infiltrated with SiC slurry and molten silicon to form the matrix. The reinforcement is composed of ten plies of fibers woven in a five-harness satin weave. The mechanism used to prevent strong bonding between matrix and reinforcement is a fiber coating of boron nitride (BN) applied through CVD. A summary of the results of this research is found in Table 2.1 showing the improved fatigue results of the composite with melt-infiltrated matrix over those with chemical vapor infiltrated matrix.

Table 2.1: Previous Research Material Properties - Summary of material property results of closely related SiC/SiC CMCs [25]

	Christensen	Delapasse	Lee	Boucher
Material	Hi-Nicalon/BN/CVI-SiC	Hi-Nicalon/SiC-B4C	Hi-Nicalon/SiC-B4C	Hi-Nicalon/BN/MI-SiC
Test Temperature (°C)	1200	1200	1300	1200
Thermal Expansion Coefficient (1/C)	6.06E-06	4.82E-06	4.74E-06	4.25E-06
Average UTS (MPa)	217	306.8	311	238
Average Elastic Modulus (GPa)	246.5	206.3	180	228
Strain at Failure (%)	0.25	0.69	0.57	0.52
Proportional Limit (MPa)	110	116	117	135
Fatigue Limit, Air, 1.0 Hz (MPa)	100	100	70	120
Fatigue Limit, Steam, 1.0 Hz (MPa)	80	100	100	110

2.7 Conclusion

To fully understand the reasoning behind the methodology presented in Chapter 3 and the failure mechanisms of interest analyzed in Chapter 4, it is imperative to have a

grasp of the composite structure and ceramic properties laid out in this chapter. It should now be clear that CMCs are the bridge between the property retention at high temperatures of ceramics and the quasi-ductile behavior of engineering alloys. The combination of these two properties makes CMCs an excellent candidate for aerospace applications but the variability of each CMC layup requires extensive testing following any major or minor change to the composite for determination of material properties. Therefore the fatigue life testing of EBC/Hi-N/MI-SiC CMCs at elevated temperatures is necessary; the methodology of which is described in Chapter 3 Methodology. The following chapter provides and describes the data collected through experimentation and the methods used to analyze the data.

Chapter 3 Methodology

3.1 Introduction

The variability of ceramic matrix composites (CMC) in fabrication techniques, processing, constituent material, weave, reinforcement type, and coating requires characterization of fatigue behavior for each instance of CMC material at elevated temperature. High temperature cyclic fatigue data is imperative to determine CMC component behavior and life prediction due to common use in the aerospace turbine engine industry where the materials are subjected to repeated loads at high temperatures. The purpose of this investigation was to determine the lifetime of a silicon-carbide/silicon-carbide CMC with a boron nitride (BN) fiber coating processed through melt infiltration and coated with an ytterbium disilicate environmental barrier coating (EBC/Hi-N/MI-SiC) while subjected to a cyclic load of various maximum stress levels to determine fatigue life. All testing was performed at 1200°C with half of the specimens exposed to air and the other half exposed to steam to simulate a highly oxidizing environment. The following methodology describes field data acquired, results gleaned, materials and equipment utilized, and procedures and processes followed.

3.2 Theory

Fatigue testing is performed to determine the lifecycle of a material when subjected to cyclic loading of various maximum stress values the material would realistically experience. The two most common types of tests are strain controlled low cycle fatigue and load controlled high cycle fatigue. High cycle fatigue is considered to be greater than 10,000 applied cycles and is relevant to the study of CMCs due to the material's primarily elastic behavior which can be better represented over thousands of

cycles. Load controlled high cycle fatigue is selected for this investigation due to the anticipated high cycling of stress experienced in turbine engines where CMC components are utilized. Additionally, load control is superior to strain control in high temperature testing environments due to the thermal strains that arise in the specimen which adversely affect the strain control method [26].

Fatigue testing is also subdivided into stress application type including tension-tension, tension-compression, and compression-compression. This naming convention describes the maximum and minimum stress levels. For instance, in tension-compression fatigue testing, maximum stress is tensile and minimum stress is compressive. Tension-tension stress application is selected due to the poor performance of CMCs when subjected to compressive loads (Figure 3.1). The stress ratio (R) is also relevant to fatigue testing and is defined as the ratio between the minimum and maximum applied stresses.

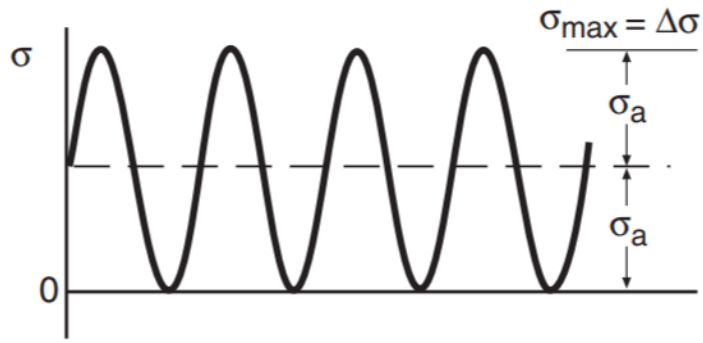

Figure 3.1: Fatigue Cycles - Cyclic stress application schematic for tension-tension fatigue testing. The stress never goes below zero and is therefore always in tension [15]

3.3 Laboratory Data

A large set of quantitative field data is collected for each test run. A test run is completed by subjecting a specimen to cyclic loading until failure is reached or runout ($2x10^5$ cycles) is achieved. Some measurements are used for final result calculations and

figure plotting while others are used to ensure the test was completed accurately and successfully. Data collected and used for results analysis include time (s), cycle number, load (N), strain (mm/mm), and displacement (mm). Additionally, prior to experimental testing, it is necessary to measure the specimen gage section cross-sectional area and estimated coating thickness of each individual specimen. Material specimen temperature (°C) and thermocouple temperature command (°C) data are collected to ensure the entire test is successfully performed at 1200°C without any major variations in temperature.

The field data collected from preliminary tensile tests and fatigue tests is synthesized into a set of plots for analysis including monotonic tensile stress-strain (σ-ε) curve, cyclic hysteresis stress-strain (σ-ε) curve, fatigue maximum stress-cycle (S-N) curve, thermal strain curve, strain-cycles (ε-N) curve, and normalized modulus-cycles (E/E_0-N) curve. Since some of the data required to create these plots is not directly measured, stress and modulus is calculated using equations 3.1 and 3.2, respectively.

$$\sigma = \frac{F}{A} \tag{3.1}$$

where σ is stress, F is load or force, and A is cross-sectional area.

$$E = \frac{\Delta\sigma}{\Delta\varepsilon} \tag{3.2}$$

where E is modulus of elasticity, $\Delta\sigma$ is the change in stress in the elastic region, and $\Delta\varepsilon$ is the change in strain in the elastic region.

3.4 Materials and Equipment

The material specimens investigated in this research were fabricated, cut, and coated by Hyper-Therm HTC a subsidiary of Rolls-Royce. Test specimens are silicon-carbide/silicon-carbide (SiC/SiC) ceramic matrix composites (CMC) consisting of ten

0/90 plies of Hi-Nicalon^{TM} SiC fibers woven in a five harness satin weave. Chemical vapor infiltration (CVI) was used to apply a boron nitride coating for a weak fiber-matrix interphase and to apply an initial layer of SiC matrix to the fiber tows. Melt infiltration (MI) of SiC particulate slurry and molten Si into the composite completed the matrix phase. The composite specimens were then cut in to dog bone shapes and received an environmental barrier coating (EBC) over their entire surface area besides the gripping ends. The EBC consists of a Si bond coat and an ytterbium disilicate ($Yb_2Si_2O_7$) top coat applied via air plasma spray (APS). The composite microstructure and cross-section is shown in Figure 3.2.

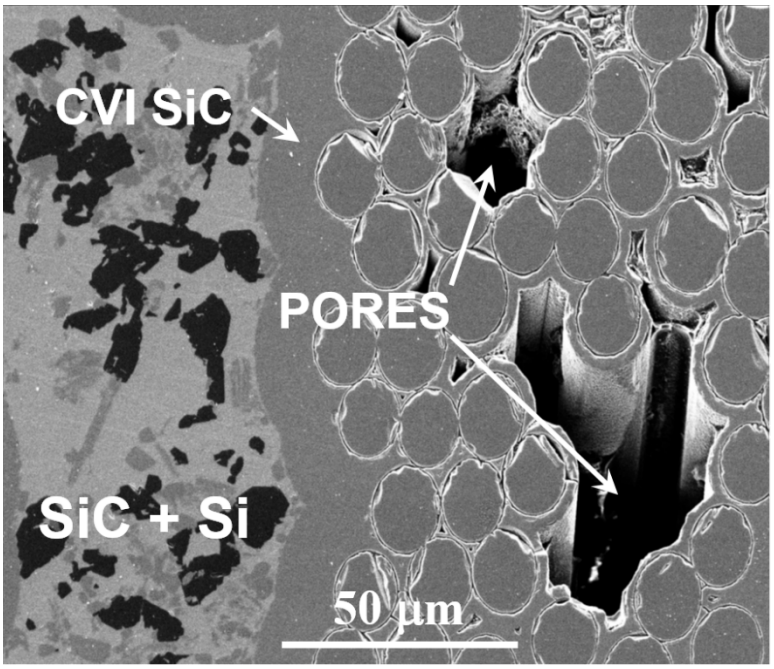

(a)

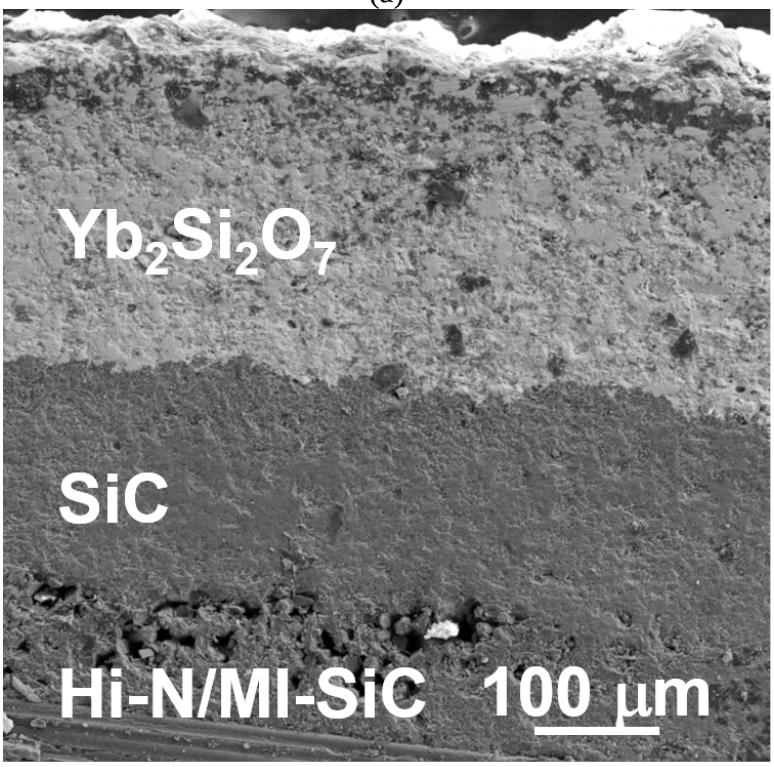

(b)

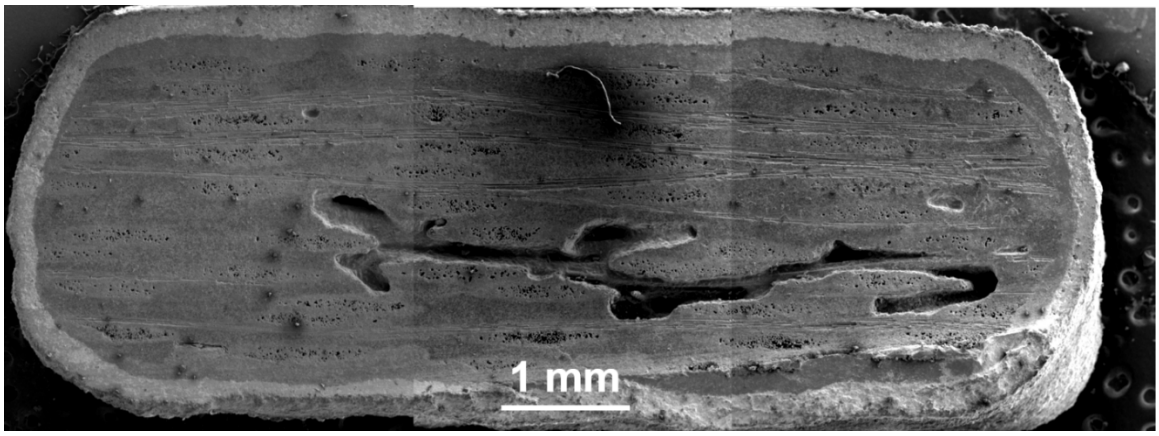

(c)

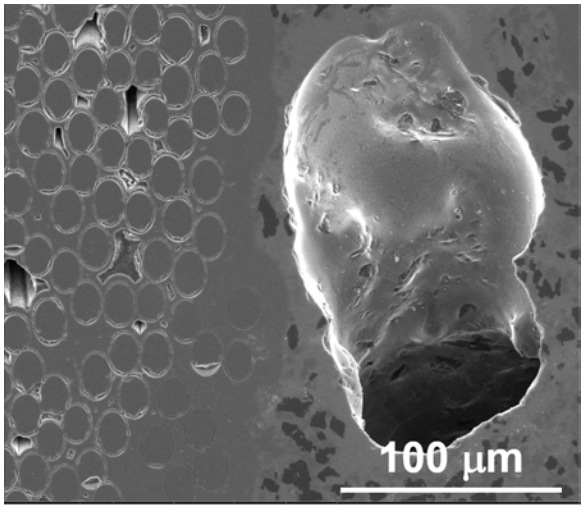

(d)

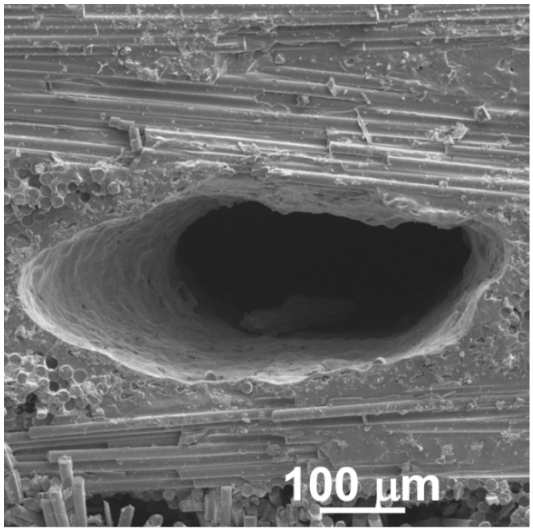

(e)

Figure 3.2: Images showing: (a) representative microstructure of Hi-Nicalon™/MI-SiC, (b) microstructure of the Si bond coat and $Yb_2Si_2O_7$ top coat, (c) test specimen cross-section with a large interior void, (d)-(e) interior voids in the EBC/Hi-N/MI-SiC composite.

Ten EBC/Hi-N/MI-SiC test specimens were examined in this research with one of the specimens used for temperature calibration elaborated upon in section 3.5. An additional two specimens of identical composition and one specimen that was grit-blasted but not coated with an EBC were subjected to monotonic tensile testing by Minor [27] prior to this research. The geometric dog bone shape of the specimens ensures failure in the smaller cross-sectional area gage length as opposed to the gripped ends which suffer

from stress concentrations from clamping. To minimize composite damage caused by the grips, fiberglass tabs were applied to both sides of the gripping areas using M-Bond 200 Adhesive.

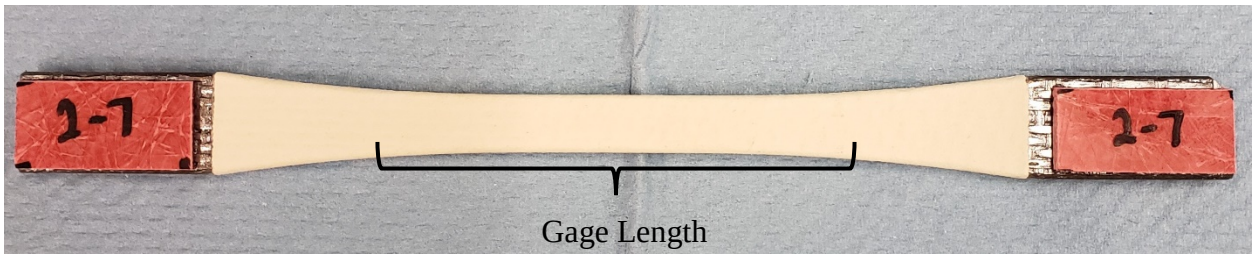

Figure 3.3: Dog Bone Specimen Geometry – Picture of dog bone shaped specimen subjected to fatigue testing. Red tabs are epoxied to the ends of the composite specimen for gripping by the MTS tension machine. Under the red tabs, the bare composite is seen while the white area of the specimen is coated by the environmental barrier coating.

The width and thickness of the gage length, including the coating, was measured for each specimen as shown in Table 3.1. Accounting for the estimated coating thickness, the load-bearing area was calculated.

Table 3.1: EBC/Hi-N/MI-SiC specimen dimension summary.

Specimen Designation	**Gage Width (mm)**	**Gage Thickness (mm)**	**Gage Cross Section (m^2)**	**Estimated Coating Thickness (mm)**	**Gage Cross Section without EBC (m^2)**
P15001-12	8.59	3.54	3.04E-05	0.381	2.18E-05
P15001-13	8.52	3.51	2.99E-05		2.13E-05
P15002-5	8.54	3.65	3.11E-05		2.24E-05
P15002-7	8.52	3.69	3.15E-05		2.27E-05
P15004-7	8.60	3.69	3.18E-05		2.30E-05
P15004-8	8.61	3.72	3.20E-05		2.32E-05
P15005-2	8.66	3.67	3.18E-05		2.30E-05
P15005-3	8.65	3.60	3.12E-05		2.67E-05
P15005-4	8.65	3.70	3.20E-05		2.31E-05
P15005-5	8.62	3.72	3.21E-05		2.33E-05
P15006-12	8.54	3.57	3.05E-05		2.18E-05
P15006-13	8.61	3.50	3.01E-05		2.15E-05

Tensile and fatigue tests were performed with an MTS monotonic and cyclic tension hydraulic load frame controlled through MTS TestSuite™ Multipurpose Software. The apparatus clamps the specimen vertically between an upper and lower grip and cyclically loads maximum and minimum stress levels. Elevated temperatures are reached and maintained by a mounted furnace controlled by a temperature controller and monitored by thermocouples. The furnace is composed of two sides which slide apart during specimen mounting and slide closed, covering most of the specimen gage length, during operation. Each half of the furnace contains a thermocouple to monitor temperature. The furnace is wrapped in insulating silica wool to maintain the elevated temperature. A cylindrical alumina susceptor is used to enclose and conduct heat to the specimen while inside the furnace. A steam generator is mounted on the test frame for application of steam inside the furnace when highly oxidizing conditions are desired during testing. The steam is passed directly onto the specimen through a hole in the susceptor. Finally, an extensometer measures the strain imposed on the specimen; both thermal strains from heating and mechanical strains from load application are measured by the extensometer. This equipment is shown in Figure 3.4.

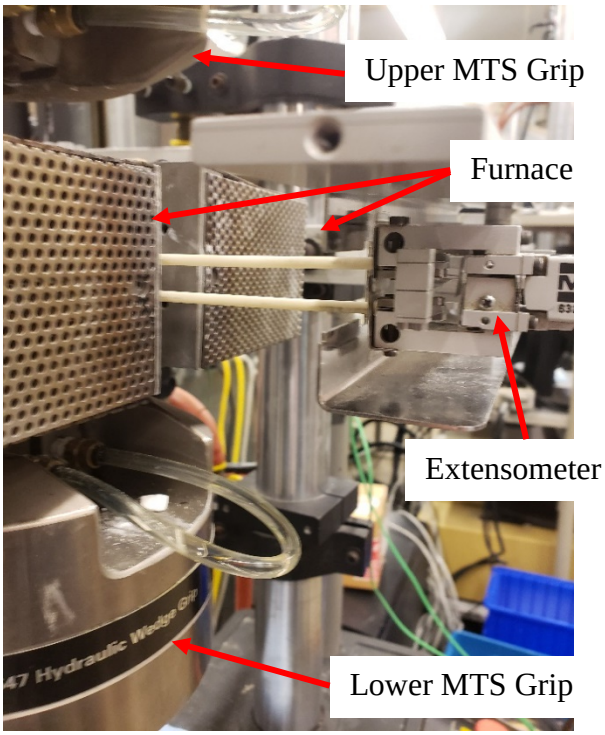

Figure 3.4: MTS Tension Test Apparatus and Equipment – MTS hydraulic load frame with labeled upper and lower grips. Mounted, two-sided furnace and extensometer for strain measurement also shown.

The test specimen fracture surfaces were evaluated using two analysis techniques: optical microscopy and scanning electron microscopy (SEM). The low magnification of optical microscopy allows simple measurement of the coating thickness and fracture surface voids. Additionally, the color and manually adjustable lighting provides an effective way to locate fiber pullout. The optical microscope used was a ZEISS SteREO Discovery.V20 light microscope. A TESCAN MAIA3 Triglav SEM was used as a more powerful analysis tool to examine and capture images of features that cannot be captured by an optical microscope including microcracks and crack initiation sites. The SEM microscopy was also used for image capture of oxidation regions on the fracture surfaces.

3.5 Procedures and Processes

3.5.1 Temperature Calibration

Temperature calibration was performed prior to testing in air and again in steam. This process is necessary since the temperature measured by the furnace thermocouples is not the same as the temperature of the specimen. To complete temperature calibration, thermocouples were placed directly in contact with a test specimen mounted on the MTS tensile test apparatus. With no load applied, the furnace temperature was raised until the thermocouples on the specimen measured 1200°C at which point the associated furnace temperature was recorded and used for subsequent tests. Performing this process at a controlled zero load allows thermal expansion to occur without subjecting the specimen to compressive forces. Due to changes of heating elements, this process was conducted multiple times. The furnace temperature setpoints are shown in Table 3.2.

Table 3.2: Temperature setpoints for furnace calibration

Test Environment	Left Set Point (°C)	Right Set Point (°C)
Air	1264	1283
	1292	1320
Steam	1220	1228
	1290	1298

3.5.2 Monotonic Tension Tests

Minor [27] performed monotonic tension tests on two EBC/Hi-N/MI-SiC specimens to determine the modulus of elasticity (E), yield stress (Y), and ultimate tensile strength (UTS) of the CMC. These tests were performed on the MTS tensile test apparatus at 1200°C by applying an increasing load until catastrophic failure was reached. The modulus of elasticity was determined as the average slope of the elastic

region of the two tensile tests. The yield stress was determined as the stress value at the onset of quasi-ductile deformation averaged between the two tests. Finally, the ultimate tensile strength was the maximum stress value reached averaged between the two tests. Additionally, a similar tensile test was performed a EBC/Hi-N/MI-SiC specimen which received grit-blasting but was not coated with an EBC.

3.5.3 Fatigue Tests

Tension-tension fatigue testing was performed on ten EBC/Hi-N/MI-SiC specimens at 1200°C on the same MTS tension test apparatus used for monotonic tensile testing. Five specimens were exposed to air and the remaining five were exposed to steam to simulate a highly oxidizing environment. A cyclic tensile load was applied to the specimen at a cyclic frequency of 1 Hz until the material failed or run-out ($2x10^5$ cycles) was achieved. If the specimen reached run-out, a monotonic tensile test was performed immediately following the fatigue test to determine retained material properties. Maximum stresses applied to the specimens were selected from similar investigations on this CMC completed by Boucher [25]. The maximum stresses applied in air were 110 MPa, 110 MPa, 120 MPa, 130 MPa, and 140 MPa. The maximum stresses applied in steam were 120 MPa, 130 MPa, 135 MPa, 135 MPa, and 140 MPa. The minimum stress of each test run was the maximum stress multiplied by a factor of 0.05. This R ratio was used to ensure the specimen would not enter compression.

3.5.4 Microstructural Characterization

Requiring no specimen preparation, a ZEISS SteREO Discovery.V20 light microscope was used to capture each fracture surface. The microstructure of both tensile specimens and six fatigue specimens was characterized with a TESCAN MAIA3 Triglav

scanning electron microscope (SEM). Fatigue specimens in air and steam with very short life, moderate life, and run-out life were selected. Specimens were cut with a diamond saw 1-2 cm behind the fracture surface of the lower half of the dog bone. The fracture surface on the lower half of the clamped specimen was characterized since it was only briefly exposed to the heating elements after fracture before it was removed from the furnace. The cut sections were mounted on ½ inch aluminum stubs affixed with carbon dots. A 5 nm iridium (Ir) coating was sputtered onto the mounted fracture surface to provide a thin layer of conductive material which improves beam resolution, reduces surface charging, and reduces beam damage [28].

3.6 Conclusion

Great care is taken in the accuracy and repeatability of the test processes described herein and large sets of data are taken to monitor the environmental conditions and material responses. Chapter 4 Results describes the synthesis of the laboratory data and discusses the significance of the measurements, calculations, and final results.

Chapter 4 Results

4.1 Results Overview

The following chapter discusses the results of high temperature monotonic tension testing and tension-tension fatigue testing along with considerations such as thermal expansion and EBC effects on EBC/Hi-N/MI-SiC. The tensile test data was collected by Minor [27] in a preliminary study to determine tensile properties of coated and uncoated specimens. Additionally, this chapter discusses the retained tensile properties of specimens which achieve run-out set at $2x10^5$ cycles. Table 4.1 summarizes the data produced from the tensile and fatigue tests where all specimens are held at 1200º C. Although all monotonic tensile tests were performed in laboratory air, the fatigue tests were split between air and steam environments.

Table 4.1: Summary of data collected from monotonic tensile tests and tension-tension fatigue tests in air and in steam at 1200º C on EBC/Hi-N/MI-SiC CMC specimens

Specimen	Test Environment	Maximum Stress (MPa)	Elastic Modulus (GPa)	Cycles to Failure (N)	Time to Failure (h)	Failure Strain (%)
			Tensile Test			
P15001-12	Laboratory Air	181	144.0	-	-	0.550
P15005-3	Laboratory Air	219	95.18	-	-	0.345
			Tension-Tension Fatigue Test			
P15004-8	Laboratory Air	110	132.8	29547	9.46	0.661
P15006-13	Laboratory Air	110	180.6	200000	55.6	0.376
P15002-5	Laboratory Air	120	306.3	100128	30.3	0.153
P15002-7	Laboratory Air	130	133.5	8869	6.33	0.619
P15004-7	Laboratory Air	140	165.7	627	1.43	1.832
P15005-5	Steam	120	108.9	200000	55.6	0.759
P15006-12	Steam	130	120.2	46674	14.2	1.034
P15005-2	Steam	135	109.7	200000	55.6	0.907
P15005-4	Steam	135	172.4	19781	6.75	0.562
P15001-13	Steam	140	179.9	342	1.35	0.481

4.2 Thermal Effects

Solid materials geometrically expand from heating based on their linear coefficient of thermal expansion, a material property having units of reciprocal temperature [10]. Heating of the material increases the atoms' vibrational energy which increases the average interatomic distance causing expansion. Although volume change due to heating effects occurs, only the linear thermal strain in the direction of loading is relevant to this study. The linear coefficient of thermal expansion (α_l) is calculated by equation 4.1 where ΔT is temperature change (ºC) and ϵ is thermal strain.

$$\alpha_l = \frac{\epsilon}{\Delta T} \tag{4.1}$$

The thermal strain was measured after the furnace had been held at 1200ºC for 45 minutes to ensure uniform heating of the specimen throughout the gage section. The thermal strain of the EBC/Hi-N/MI-SiC composite varied between 0.381% and 0.706% with an average of 0.505%. The average thermal strain compared closely with the uncoated Hi-N/MI-SiC composite reported by Boucher [25] as 0.498%. The average CTE of the EBC/Hi-N/MI-SiC composite was calculated as 4.29 x 10^{-6} 1/ºC which is only slightly greater than the average CTE of the Hi-N/MI-SiC composite at 4.25 x 10^{-6} 1/ºC. The EBC application shows negligible effects on the measured thermal strains and the calculated CTEs.

Table 4.2: Summary of thermal strain and linear coefficient of thermal expansion for EBC/Hi-N/MI-SiC

Specimen	Thermal Strain (%)	Coefficient of Linear Thermal Expansion (10^{-6} / °C)
P15001-12	0.706	6.00
P15005-3	0.620	5.27
P15004-8	0.485	4.12
P15006-13	0.390	3.31
P15002-5	0.495	4.21
P15002-7	0.661	5.61
P15004-7	0.466	3.96
P15005-5	0.529	4.49
P15006-12	0.456	3.87
P15005-2	0.419	3.56
P15005-4	0.455	3.87
P15001-13	0.381	3.24
Average	0.505	4.29
Std. Dev.	0.105	0.89

4.3 Monotonic Tension Test

Monotonic tension testing at 1200ºC was performed on two EBC/Hi-N/MI-SiC specimens and one grit-blasted Hi-N/MI-SiC specimen. The uncoated specimen was included in the study to examine the effects of grit-blasting prior to EBC application on the tensile properties of the composite. Some variation in tensile properties between the two coated specimens was present so the elastic modulus, proportional limit, ultimate tensile strength (UTS), and failure strain were taken as average values between the two tests. These average values are then used to determine retained tensile properties in section 4.5. The proportional limit was determined by generating a line over the elastic region of the response with the same slope and visually determining where the line and the response deviate.

Using ten data points along the elastic region of the response the elastic modulus or the slope of the linear portion of the stress-strain curve of the EBC/Hi-N/MI-SiC and grit-blasted Hi-N/MI-SiC specimens was calculated as a significantly lower value than the composite studied by Boucher [25] which did not receive grit-blasting. This means that the grit-blasted specimens developed matrix cracks at a lower load application. The standard Hi-N/MI-SiC composite also displayed a greater proportional limit and UTS compared to the grit-blasted counterparts. The proportional limit is the maximum stress at which the stress-strain curve is linear in the elastic region and the UTS is the maximum stress the material reaches before failure. The failure strain is relatively uniform across tensile tests with the EBC/Hi-N/MI-SiC composite having a failure strain of 0.448% and the grit-blasted specimen with no EBC having a failure strain of 0.345%. The test results summarized in Table 4.3 confirm that it is grit-blasting that alters the tensile results and the EBC has a negligible effect on the tensile properties.

The lower tensile properties of the grit-blasted specimens were anticipated due to the nature of the process. The pressurized stream of ceramic grits which impinge on the surface of the specimen damages and weakens the exterior of the composite. This is specifically apparent in the values of elastic modulus and UTS when compared to virgin specimens.

Table 4.3: Summary of tensile properties of Hi-N/MI-SiC with grit-blasting and EBC, grit-blasting only, and a virgin specimen

Material	Elastic Modulus (GPa)	Proportional Limit (MPa)	UTS (MPa)	Failure Strain (%)
EBC/Hi-N/MI-SiC	119.6	119	200	0.448
Hi-N/MI-SiC Grit-Blasted	120.9	110	181	0.345
Hi-N/MI-SiC	217.1	135	239	0.412

Figure 4.1 compares the stress-strain curves for EBC/Hi-N/MI-SiC and grit-blasted Hi-N/MI-SiC specimens and displays the bilinear behavior exhibited by ceramic matrix composites. Following the linear elastic region, the curves enter a second linear portion of decreased slope indicative of matrix cracking. Although the individual tensile properties vary, each curve assumes this bilinear curvature. Figure 4.2 shows the superior tensile test results of a specimen not subjected to grit-blasting.

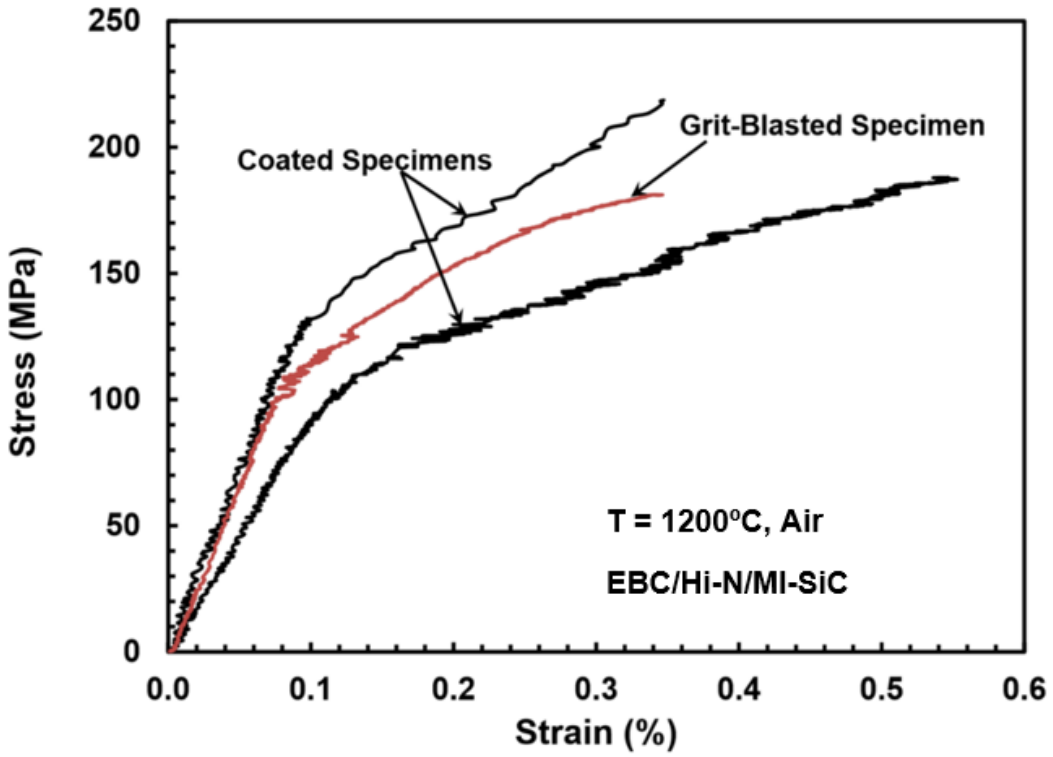

Figure 4.1: Monotonic tension test stress-strain curve for EBC/Hi-N/MI-SiC and grit-blasted Hi-N/MI-SiC [27]

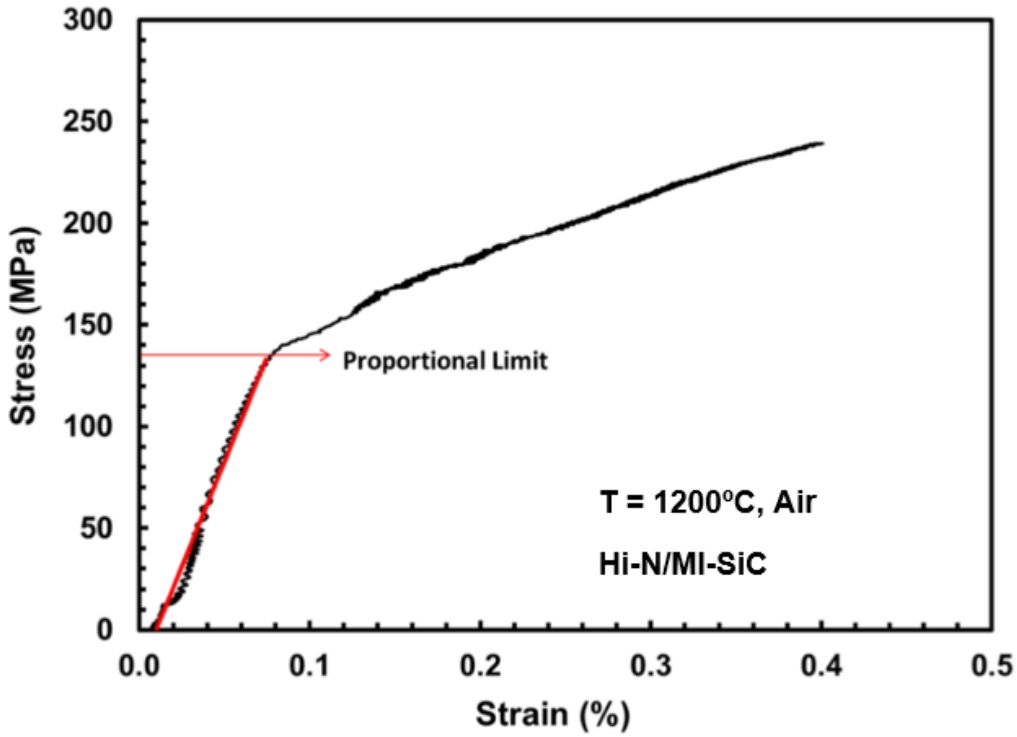

Figure 4.2: Monotonic tension test stress-strain curve for Hi-N/MI-SiC [25]

4.4 Tension-Tension Fatigue Test

Tension-tension fatigue testing was performed on ten EBC/Hi-N/MI-SiC composite specimens at 1200ºC, five in laboratory air and five in steam. Cyclic loading was applied at a frequency of 1 Hz with maximum load values calculated from the specimen cross-sectional area and maximum stresses selected according to previous work on the uncoated CMC [25] to provide comparative data. The maximum stresses were 110 MPa, 120 MPa, 130 MPa, and 140 MPa in air and 120 MPa, 130 MPa, 135 MPa, and 140 MPa in steam. Irregular data was produced by the initial fatigue tests with maximum stresses of 110 MPa in air and 135 MPa in steam so these tests were repeated. The minimum load was determined by using a multiplying factor, R=0.05. The specimens were subjected to fatigue testing until failure or run-out was achieved. In this examination, run-out was defined as $2x10^5$ cycles. Following run-out of a specimen, a tensile test was performed to

determine the retained tensile properties. The specimens which achieved run-out were those tested with a maximum stress of 110 MPa in air, 120 MPa in steam, and 135 MPa in steam.

Table 4.4: Summary of tension-tension fatigue test results of EBC/Hi-N/MI-SiC

Specimen	Test Environment	Maximum Stress (MPa)	Elastic Modulus (GPa)	Cycles to Failure (N)	Time to Failure (h)	Failure Strain (%)
P15004-8	Laboratory Air	110*	132.8	29547	9.46	0.661
P15006-13	Laboratory Air	110*	180.6	200000	55.6	0.376
P15002-5	Laboratory Air	120	306.3	100128	30.3	0.153
P15002-7	Laboratory Air	130	133.5	8869	6.33	0.619
P15004-7	Laboratory Air	140	165.7	627	1.43	1.832
P15005-5	Steam	120	108.9	200000	55.6	0.759
P15006-12	Steam	130	120.2	46674	14.2	1.034
P15005-2	Steam	135	109.7	200000	55.6	0.907
P15005-4	Steam	135	172.4	19781	6.75	0.562
P15001-13	Steam	140	179.9	342	1.35	0.481

*Maximum stresses below the measured proportional limit (119 MPa)

The presence of steam did not detrimentally affect the coated CMC as Table 4.4 shows superior results under the steam condition. At a maximum stress of 120 MPa, there was a 50% decrease in fatigue life in the air condition compared to the steam condition. Similarly, at a maximum stress of 130 MPa, there was an 81% decrease in fatigue life between steam and air conditions. Specimens P15005-2 and P15005-4 were subjected to the same maximum stress and environmental condition but exhibited drastically different results. This is partially due to the variability of the number and size of interior voids but specimen P15005-4 displays fracture surface oxidation which is not present on P15005-2.

Figure 4.3 displays maximum stresses versus cycles to failure for each test run. As expected, besides the two irregular data sets mentioned previously, an increase in maximum stress caused a decrease in the number of cycles to failure in both air and

steam. It was anticipated that the harsher steam environment would lead to a significant decrease in fatigue life compared to the specimens tested in air, but the small sample size of data does not show this correlation. Instead, the specimens tested in steam performed similar to the tests in laboratory air at high maximum stresses and superior in low maximum stresses. This is shown in the divergence of the trendlines of Figure 4.3. Additionally, run-out was achieved under the steam condition at a higher maximum stress value than in air. The effect of the air and steam environment was normalized with the presence of the EBC as the EBC prevented water from penetrating into the composite. Steam was able to deeply penetrate the composite surface of the uncoated specimens due to macroscopic voids that are not open to the environment on specimens coated with an EBC.

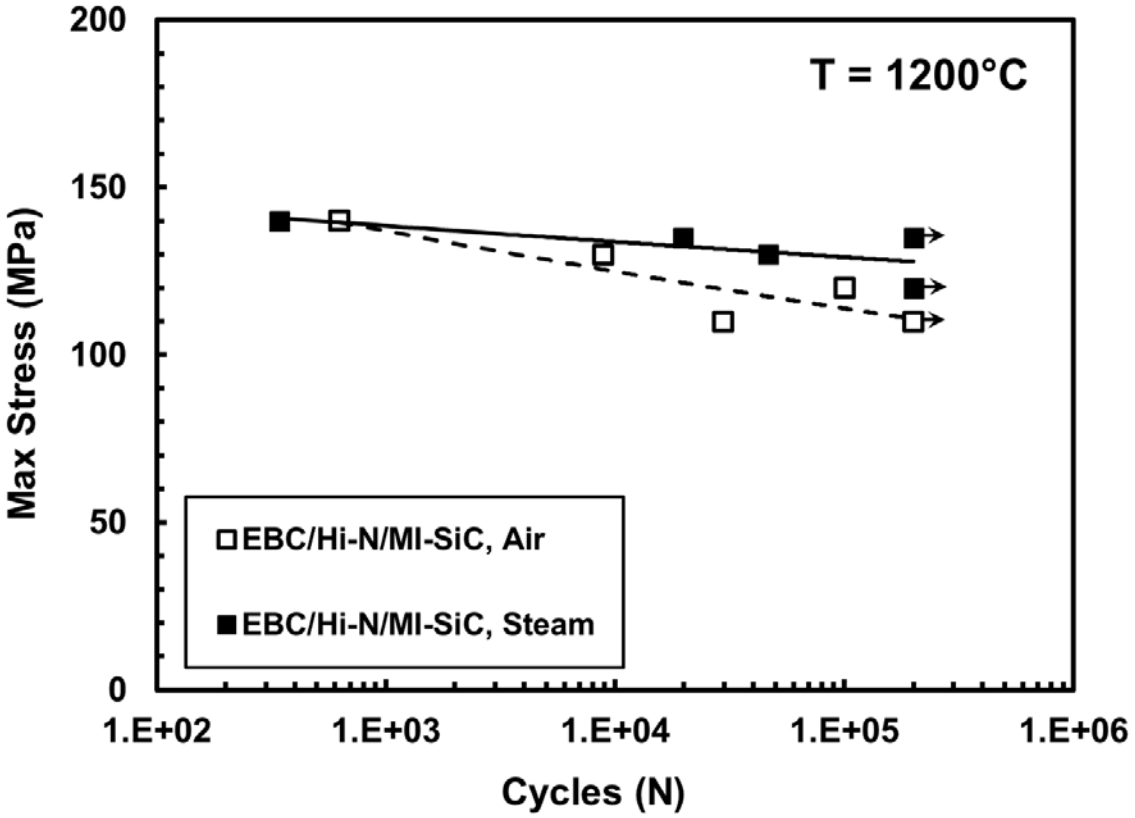

Figure 4.3: S-N curve with trendlines for EBC/Hi-N/MI-SiC composite specimens in air and in steam at 1200ºC

Table 4.5 compares the number of cycles to failure in air and in steam of coated and uncoated Hi-N/MI-SiC at similar maximum stress values. Both sets of data show a smaller variation of life between environmental conditions at high maximum stress values than at low. However, EBC/Hi-N/MI-SiC specimens have a more fluctuating change in life in steam compared to the uniform decrease in life of the Hi-N/MI-SiC specimens. This is also shown in Figure 4.4 where Boucher's fatigue results of Hi-N/MI-SiC are plotted against EBC/Hi-N/MI-SiC on an S-N curve. The uncoated specimens tested in air consistently last longer than those in steam creating nearly parallel trendlines, a behavior the coated specimens do not display.

Table 4.5: Fatigue results of EBC/Hi-N/MI-SiC and Hi-N/MI-SiC at comparative maximum stress values

Maximum Stress (MPa)	Cycles to Failure (N)		Change in Life in Steam (%)
	Air	**Steam**	
EBC/Hi-N/MI-SiC			
120	100128	200000	100
130	8869	46674	426
140	627	342	-45
Hi-N/MI-SiC			
120	200000	5311	-97
130	4506	3201	-29

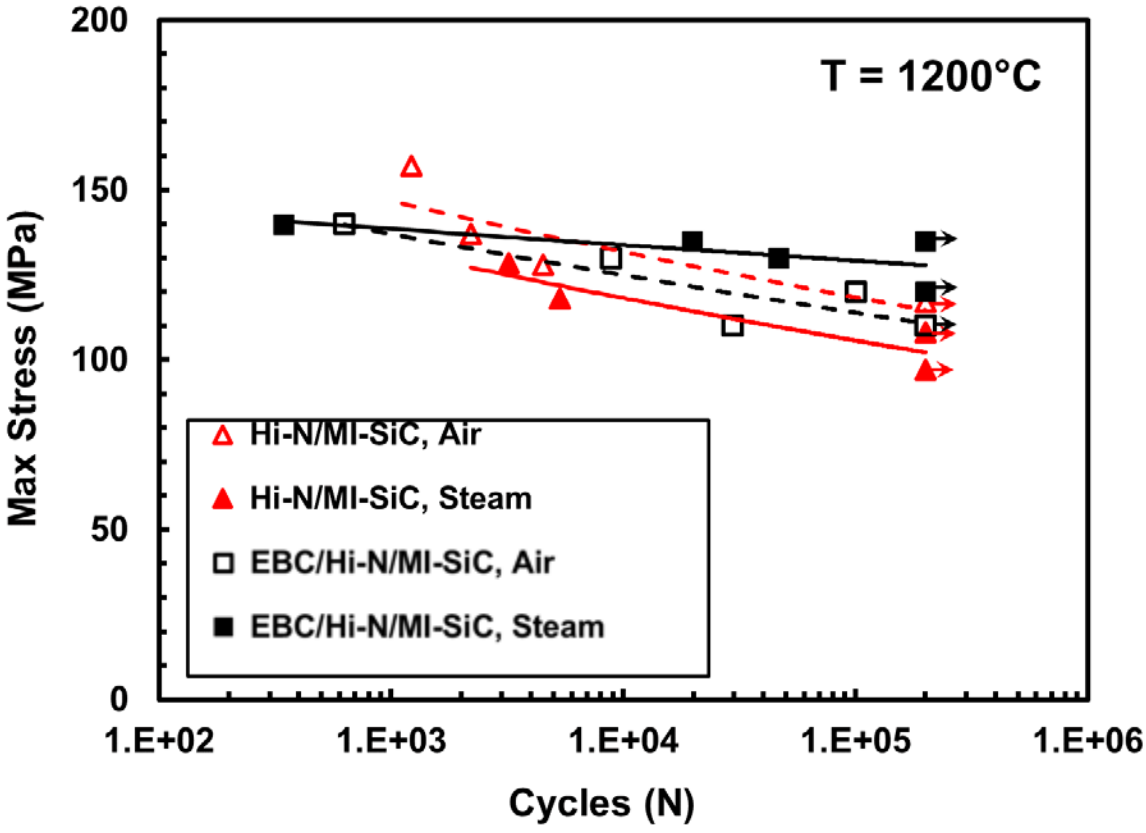

Figure 4.4: S-N curve with trendlines for EBC/Hi-N/MI-SiC and Hi-N/MI-SiC composite specimens in air and in steam at 1200ºC

Figure 4.5 displays a similar S-N curve where maximum stress is replaced by percent of ultimate tensile strength (%UTS). From this perspective the coated specimens perform superior to the uncoated specimens through the composite lifecycle.

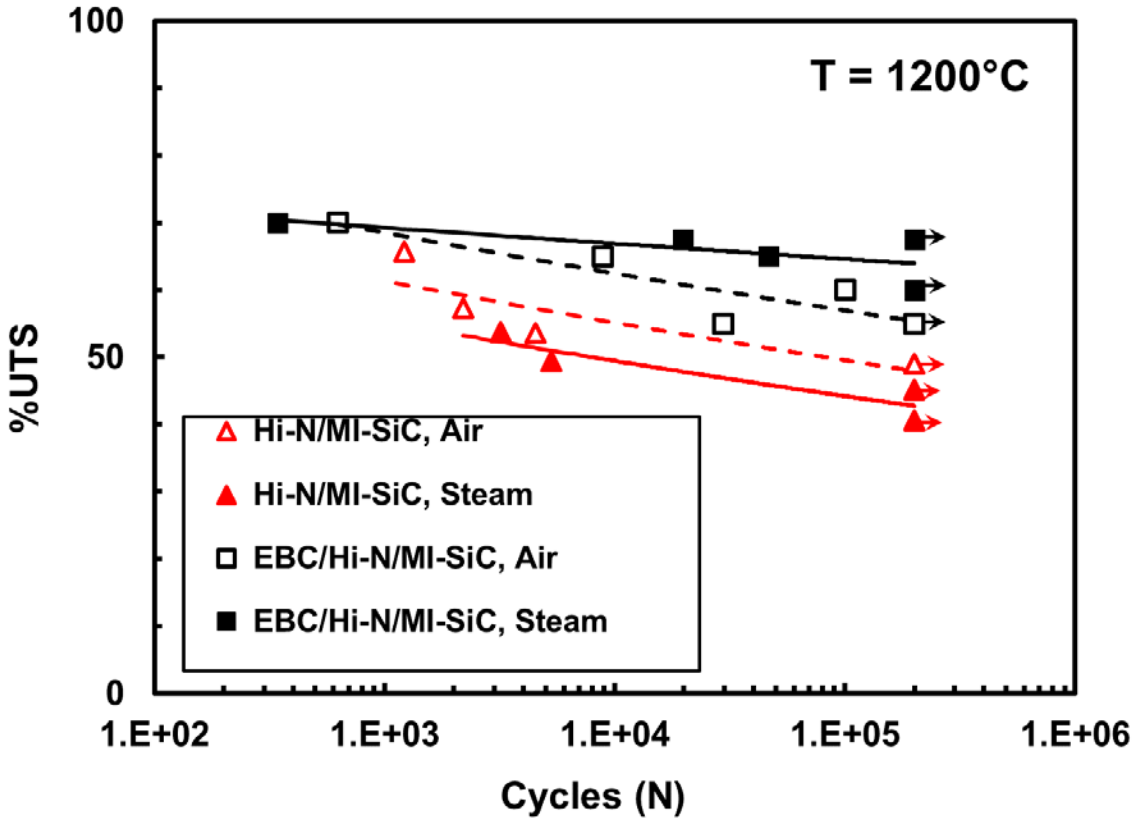

Figure 4.5: %UTS vs cycles with trendlines for EBC/Hi-N/MI-SiC and Hi-N/MI-SiC composite specimens in air and in steam at 1200ºC

Regarding the fatigue life of Hi-N/MI-SiC, Boucher [25] discovered that the fatigue life of the composite decreased by nearly two orders of magnitude when the maximum stress was raised above the run-out stress. According to fracture mechanics, it is postulated that the large surface voids in the composite serve as crack initiation sites when a sufficiently large stress range is applied. The stress intensity range ΔK is dependent upon flaw geometry, size, and remotely applied stress range. Since all

specimens were similarly processed, it is assumed that the largest flaw geometry and size are constant across fatigue tests. This leaves the remotely applied stress range as the determining factor for ΔK_{TH} or the threshold stress intensity range below which crack propagation in a fatigue test is stymied. Figure 4.6 shows the three regions of typical fatigue crack growth with varying slope: primary, secondary, and tertiary. Boucher's results show that ΔK_{TH} occurs just above the run-out maximum stresses of 110 MPa in air and 120 MPa in steam. The results show an immediate drastic decrease in fatigue life above run-out correlating to a very small secondary region of constant slope.

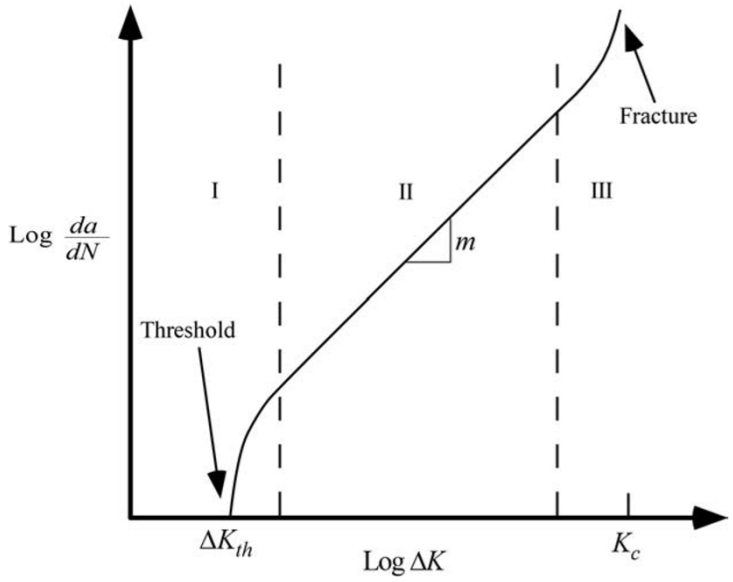

Figure 4.6: Typical fatigue crack growth where da/dN is crack growth rate and ΔK is stress intensity factor range [29]

The fatigue results of EBC/Hi-N/MI-SiC do not exhibit the same sharply decreasing fatigue life behavior above run-out maximum stresses of the uncoated specimens. This is seen in Figure 4.4 as there are multiple intermediate data points between fatigue run-out at low maximum stresses and extremely short fatigue life at high

maximum stresses. This is most likely caused by EBC filling the composite's largest surface voids and therefore altering the threshold stress intensity range ΔK_{TH} or increasing the size of the secondary region of fatigue crack growth shown in Figure 4.6. However, this benefit is not enough to overcome the damage caused by grit-blasting and the EBC does not benefit the composite's fatigue life. The coated specimens had shorter fatigue life in air and in steam than uncoated specimens tested at similar maximum stresses and run-out was achieved at higher maximum stresses in the steam environment.

The normalized modulus variation with an increase in cycles shows the damage development of the material over time. Figure 4.7 and Figure 4.8 display the change in normalized modulus of EBC/Hi-N/MI-SiC at various cycle intervals to map the retention of elasticity over time in air and in steam respectively. The normalized modulus is the ratio between the hysteresis modulus of a cycle and the modulus of the first cycle where the modulus is the difference between the maximum and minimum stress-strain data. Each data set cycles between an increasing and decreasing normalized modulus but trends toward an overall decrease in modulus prior to failure which physically manifests as a weaker elastic response. Two specimens tested in air exhibit an increasing modulus during early cycles which may be caused by hysteresis error in data collection when the composite matrix has not yet developed significant damage which would reduce the normalized modulus. Prior to failure, specimens tested in air with maximum stresses of 110 MPa and 130 MPa show an increasing behavior in modulus. This may be due to matrix cracking around fibers but fibers remaining intact until final failure which would alter the perceived elastic behavior of the material.

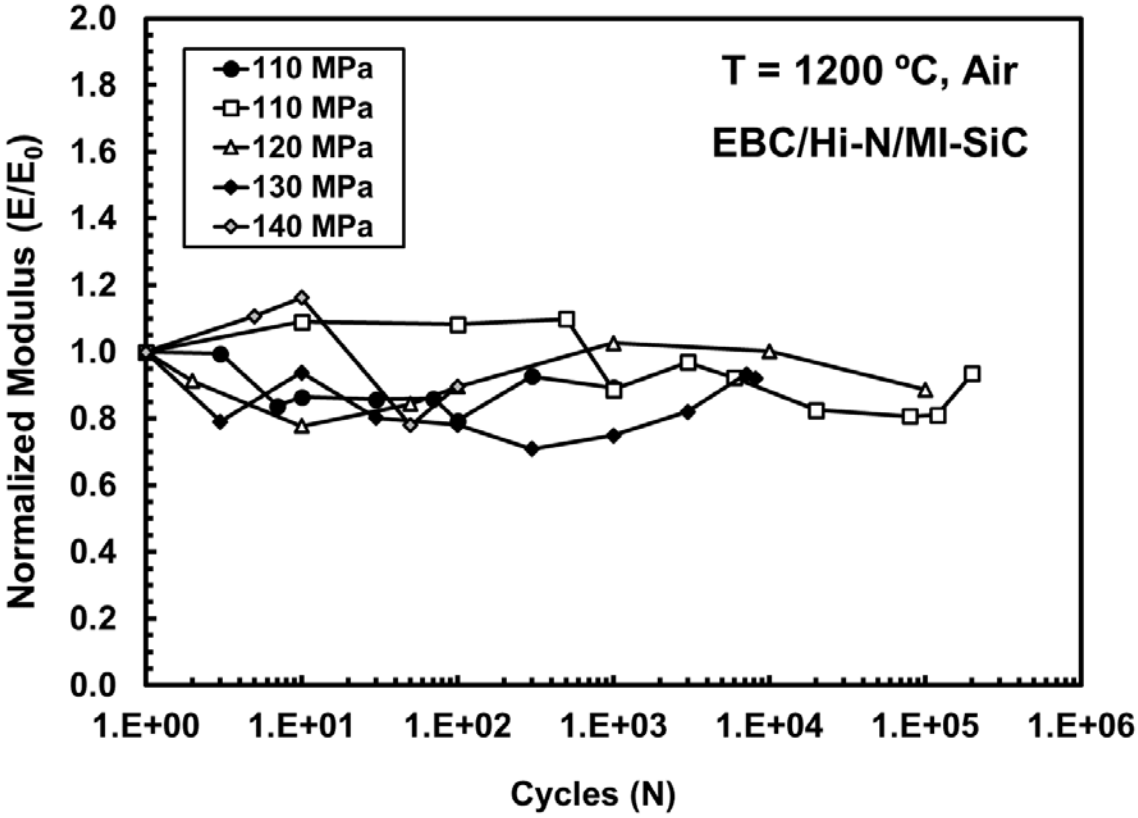

Figure 4.7: Normalized modulus versus cycles for EBC/Hi-N/MI-SiC composite specimens in air at 1200ºC

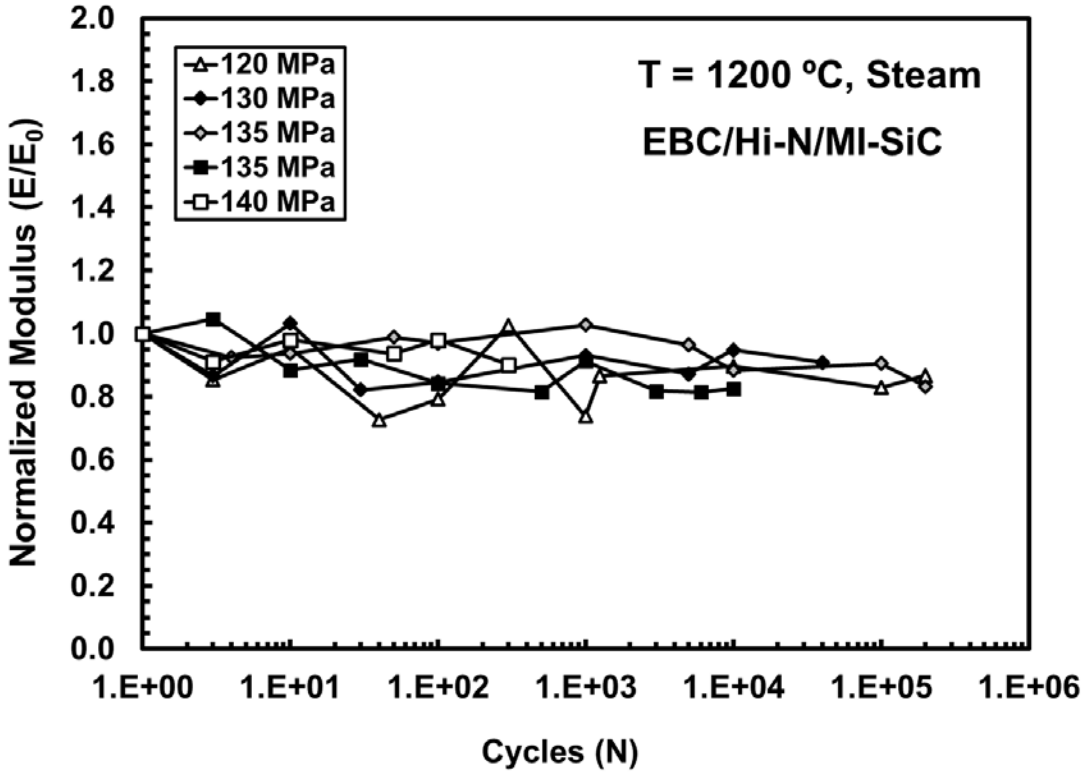

Figure 4.8: Normalized modulus versus cycles for EBC/Hi-N/MI-SiC composite specimens in steam at 1200ºC

Figure 4.9 and Figure 4.10 display the similitude of the variation of normalized modulus between the coated specimens of this research and the uncoated specimens of Boucher's [25] research. The normalized modulus in air remains closely linked varying between 0.9-1.1 for the uncoated specimens and 0.8-1.2 for those with an EBC. Additionally, the data collected in steam for the coated and uncoated specimens shows a very similar trend with normalized modulus varying between 0.75-1.05.

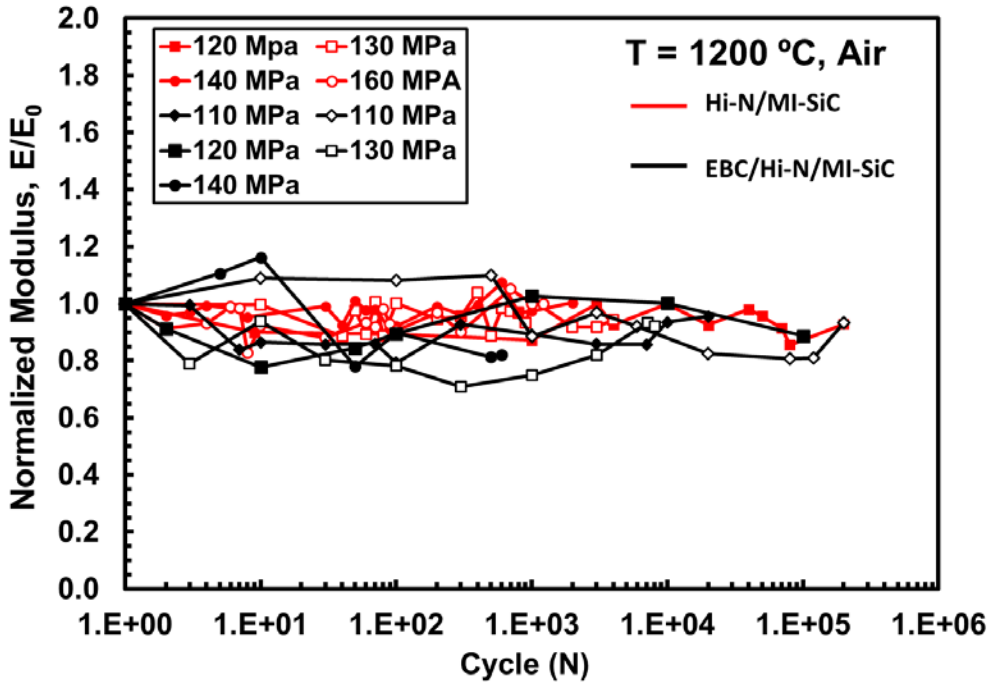

Figure 4.9: Normalized modulus versus cycles for EBC/Hi-N/MI-SiC and Hi-N/MI-SiC composite specimens in air at 1200ºC

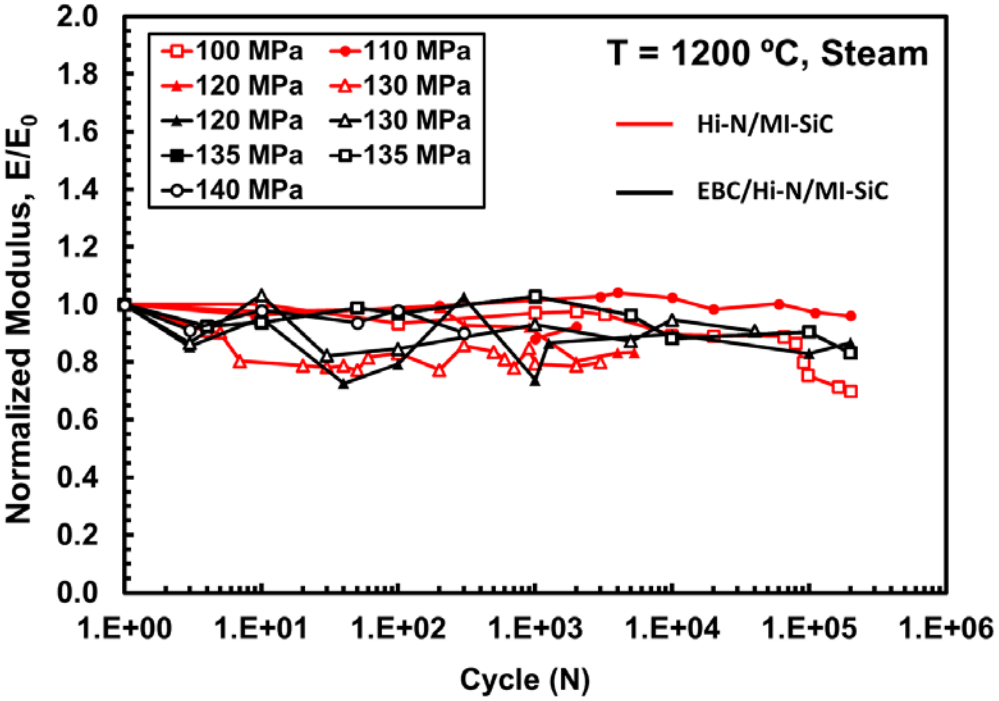

Figure 4.10: Normalized modulus versus cycles for EBC/Hi-N/MI-SiC and Hi-N/MI-SiC composite specimens in steam at 1200ºC

Accumulated strain was measured as a way to determine elongation deformation of the composite specimens during cycling or strain ratchetting. Recorded strains were taken at the minimum stress value of the particular cycle. Figure 4.11 and Figure 4.12 show accumulated strain versus cycles in air and in steam at 1200ºC. In air, strain accumulation is more erratic with the high maximum stress of 140 MPa resulting in a large strain on the initial cycle followed by multiple steps of rapidly increasing strain until failure. This same fast strain accumulation is also present in the 120 MPa test until the rate increase nearly ceases at 10^3 cycles. The two 110 MPa tests and the 130 MPa test display strain ratchetting at a slower pace similar to their specimen counterparts subjected to steam. In steam, as shown in Figure 4.12, strain ratchetting is consistent and nearly linear on the log scale until 10^4 cycles where a nonlinear increase begins until failure or run-out is reached.

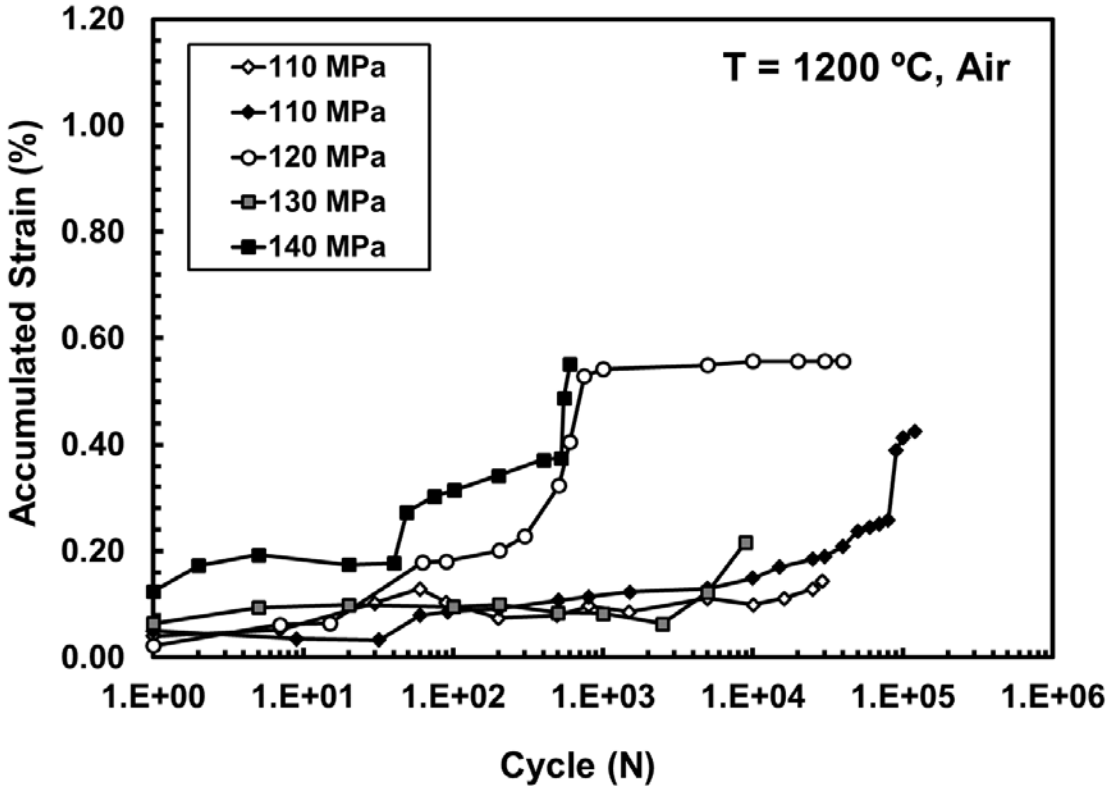

Figure 4.11: Accumulated strain versus cycles for EBC/Hi-N/MI-SiC at 1200ºC in air

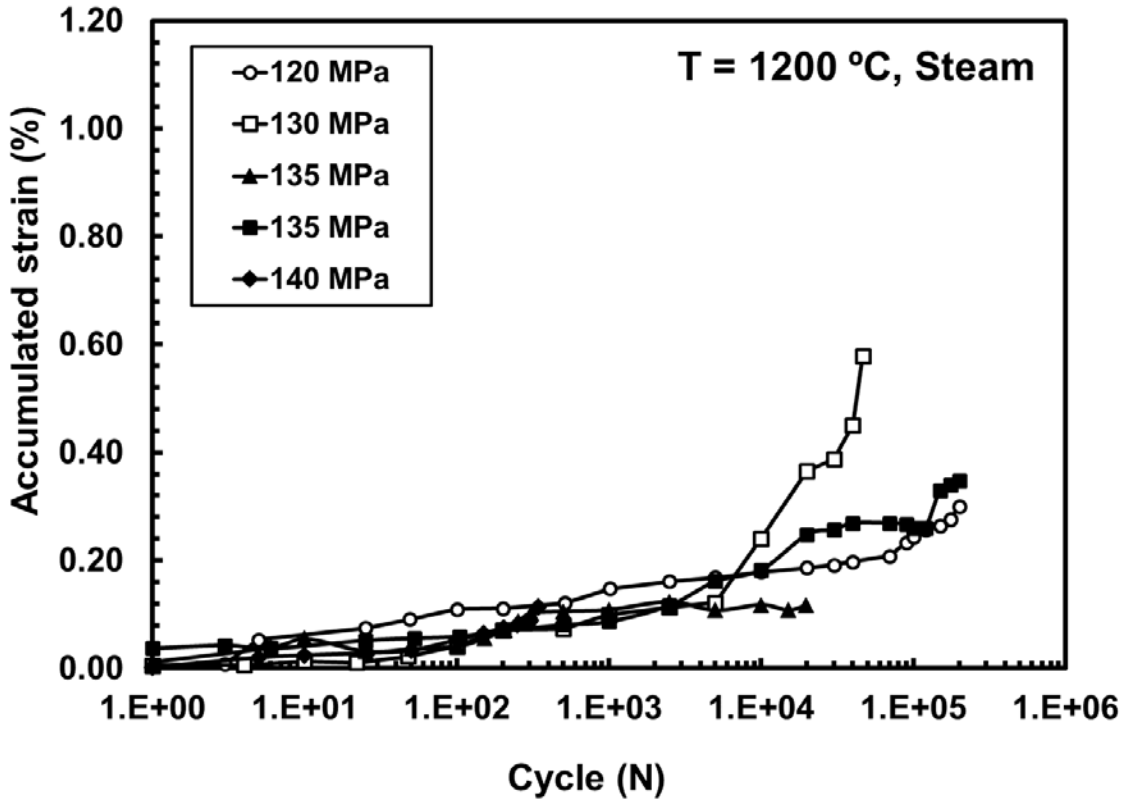

Figure 4.12: Accumulated strain versus cycles for EBC/Hi-N/MI-SiC at 1200ºC in steam

In Figure 4.13 and Figure 4.14, strain accumulation versus cycles of EBC/Hi-N/MI-SiC is compared to the results of Hi-N/MI-SiC [25] and Hi-Nicalon^{TM}/B_4C [22] both of which do not have an EBC. Strain accumulation of the coated specimens is significantly larger than the uncoated Hi-N/MI-SiC. Interestingly, the data conforms closer to a similar but different uncoated CMC studied previously by Delapasse, Hi-Nicalon^{TM}/B_4C [22]. Although the microstructure of the two different composites varied, the benefits of the self- healing matrix in Hi-Nicalon^{TM}/B_4C and the coating on EBC/Hi-N/MI-SiC exhibited similar behaviors in strain accumulation due to oxidation prevention.

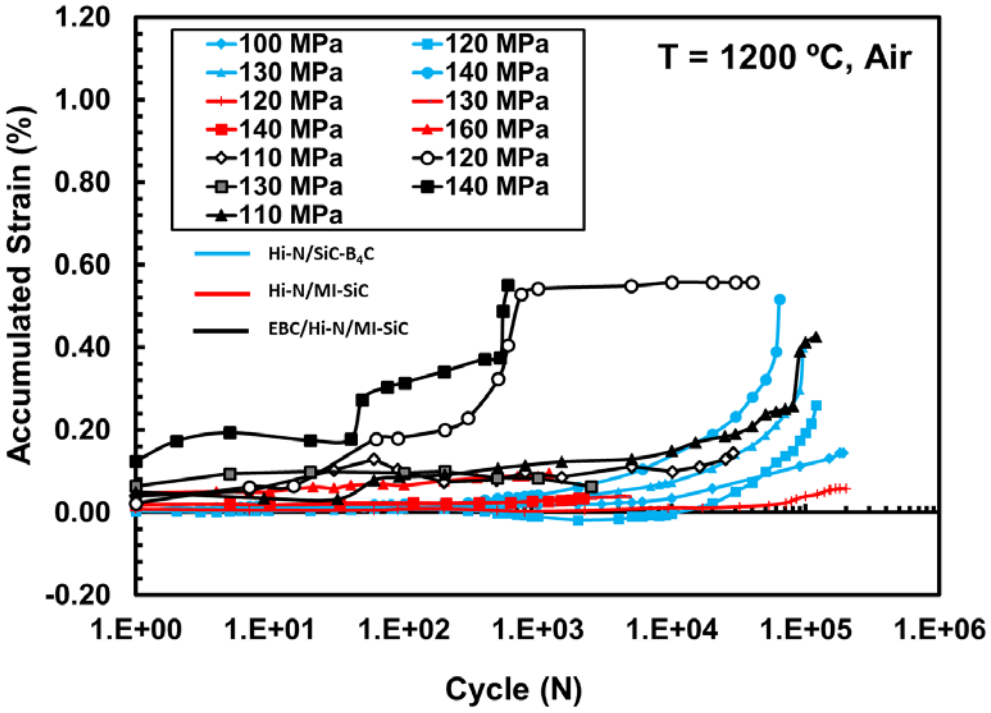

Figure 4.13: Accumulated strain versus cycles for EBC/Hi-N/MI-SiC, Hi-N/MI-SiC [25], and Hi-Nicalon^{TM}/B_4C [22] at 1200ºC in air

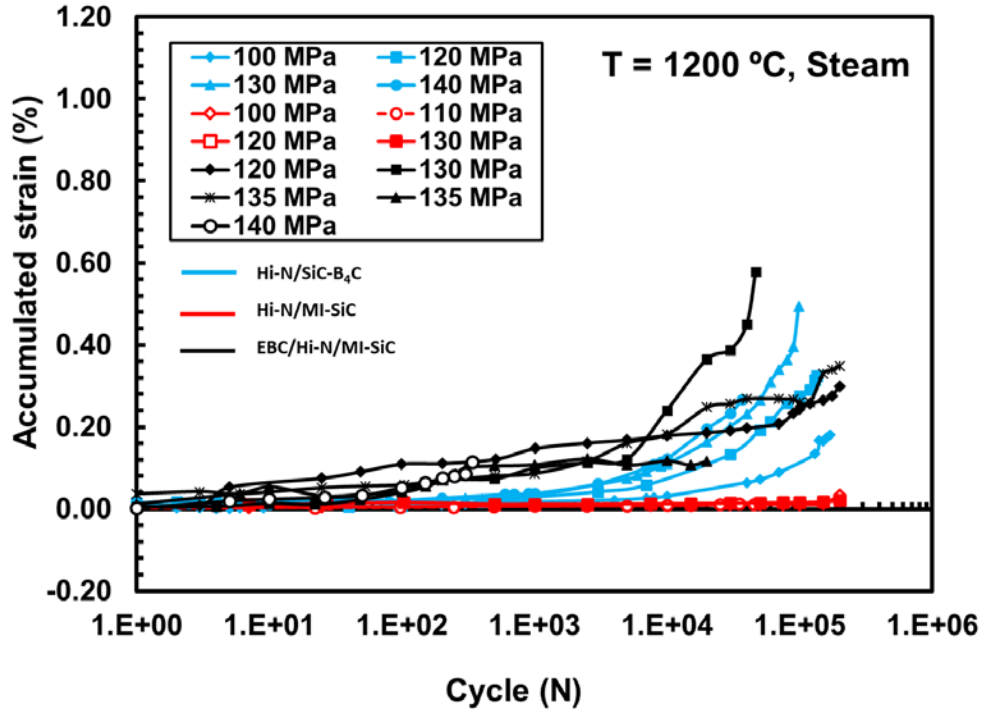

Figure 4.14: Accumulated strain versus cycles for EBC/Hi-N/MI-SiC, Hi-N/MI-SiC [25], and Hi-Nicalon^{TM}/B_4C [22] at 1200ºC in steam

4.5 Retained Tensile Properties

Tension-tension fatigue specimens which reached $2x10^5$ cycles at 1200ºC were subjected to a monotonic tension test immediately following run-out to determine the retained tensile properties of the composite. Three EBC/Hi-N/MI-SiC specimens reached run-out, one in air and two in steam. The tension test results are summarized in Table 4.6. EBC/Hi-N/MI-SiC displayed excellent UTS and modulus retention in both air and steam. The specimen which achieved run-out in air maintained ~100% of its UTS and measured a greater modulus than the tensile test of the virgin material. Similarly, the average retained strength of the two run-out specimens in steam is ~99%. The specimen which achieved run-out in steam at a high maximum stress (σ_{max} = 135 MPa) showed significant softening as the retained modulus was only 35% and the failure strain was a high 1.02%.

Table 4.6: Retained tensile properties of EBC/Hi-N/MI-SiC

Fatigue Stress (MPa)	Test Environment	Retained Strength (MPa)	Strength Retention (%)	Retained Modulus (GPa)	Modulus Retention (%)	Failure Strain (%)
110	Laboratory Air	199	100	196.1	164	0.23
120	Steam	180	90	131.8	109	0.14
135	Steam	217	109	66.9	31	1.02

The retained tensile properties of the coated EBC/Hi-N/MI-SiC composite are compared to Hi-N/MI-SiC in Table 4.7. Both coated and uncoated specimens were successful in retaining their strengths. Coated samples performed better when analyzed as a retained percentage of UTS (%). However, the virgin specimen tensile tests of the uncoated Hi-N/MI-SiC displayed superior UTS values (MPa) which is still present after 200,000 cycles of fatigue testing. The coated specimens maintained superior modulus retention (%) although the retained modulus values (GPa) were very similar. This is due

to the decrease in initial modulus values following grit-blasting and coating. In both research cases, the run-out specimens with the lowest retained modulus resulted in the largest failure strain due to material softening; both cases occurred in the steam environment.

Table 4.7: Comparison of the retained tensile properties of EBC/Hi-N/MI-SiC versus Hi-N/MI-SiC [25]

Fatigue Stress (MPa)	Test Environment	Retained Strength (MPa)	Strength Retention (%)	Retained Modulus (GPa)	Modulus Retention (%)	Failure Strain (%)
EBC/Hi-N/MI-SiC						
110	Laboratory Air	199	99.5	196.1	164	0.232
120	Steam	180	90.1	131.8	109	0.144
135	Steam	217	108.6	66.9	31	1.025
Hi-N/MI-SiC						
120	Laboratory Air	231	96.7	140	64.6	0.395
100	Steam	216	90.4	83	38.2	0.402
110	Steam	198	82.8	195	89.8	0.350

4.6 Composite Microstructure

4.6.1 Coating Thickness Microscopy

A section of EBC/Hi-N/MI-SiC specimen P15001-13 which was subjected to tension-tension fatigue testing in steam at 140 MPa until failure at 342 cycles was cut with a diamond saw approximately 2.5 cm behind the fracture surface. The cut specimen is within the gauge section but just outside the furnace during fatigue testing making it nearly unaffected by the elevated temperatures. SEM microscopy of the mounted surface shown in Figure 4.15 provides insight on the EBC thickness and CMC processing flaws. Correspondence with the CMC manufacturer provided estimated thicknesses of 254 μm and 127 μm for the topcoat and the bond coat, respectively. Measurements of the EBC on specimen P15001-13 showed an average topcoat thickness of 225 μm and a bond coat

thickness of 160 μm. Although these individual thicknesses vary from the estimated values, there is only a 1.13% difference between the total EBC coating thickness. Overall, the shorter sides of the specimen tended toward a thinner coating while the EBC thickness was greatest on the longer sides. An internal processing flaw is clearly present in Figure 4.15 which extends across approximately three-quarters of the gauge width. These types of flaws drastically reduce the possible lifetime of the specimen.

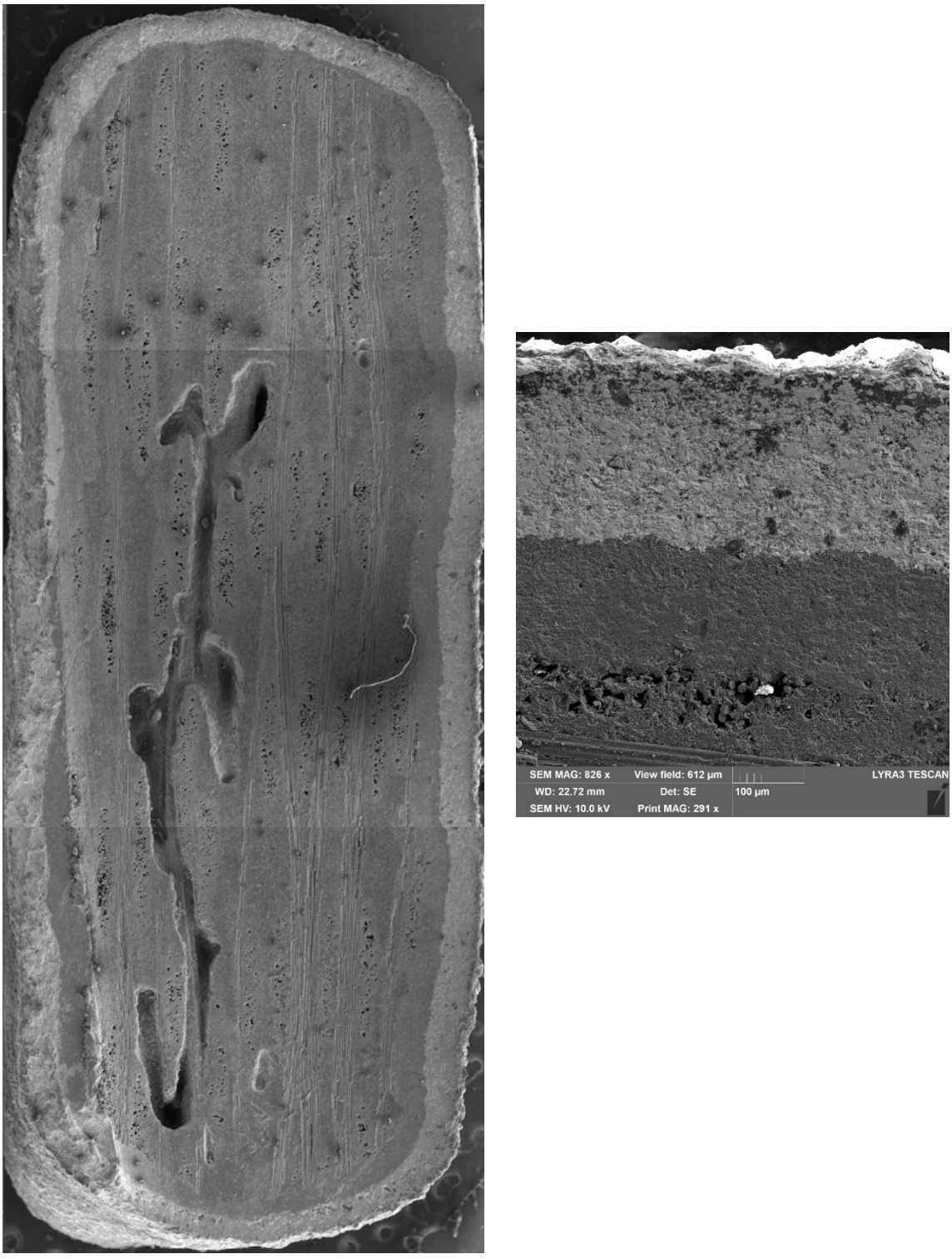

Figure 4.15: EBC/Hi-N/MI-SiC specimen P15001-13, 2.5 cm below the lower fracture surface

4.6.2 Tensile Test Specimen Microscopy

The micrographs of tensile test specimens P15006-4 and P15001-12 were compared to examine the effects of grit-blasting and the combination of grit-blasting and coating. Both CMCs exhibit similar significant fiber pullout. These phenomena are expected since the short duration of a tensile test does not provide enough time for significant oxidation. Internal flaws are also present in each specimen which is expected since they were similarly processed and the EBC does not fill internal voids. An item of interest on coated specimen P15001-12 is the apparent filling of a surface void with the EBC.

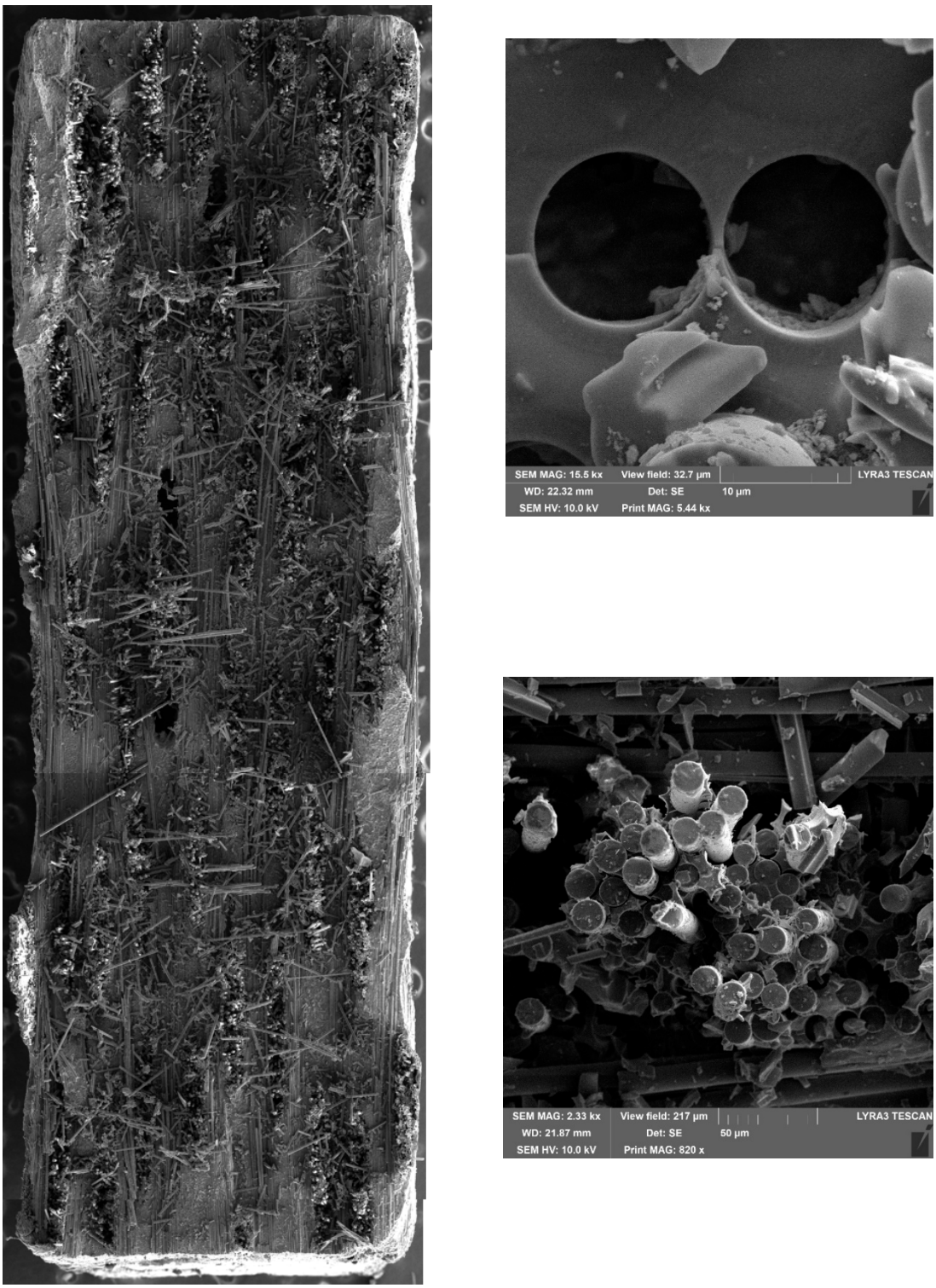

Figure 4.16: Hi-N/MI-SiC/Grit-Blasted specimen P15006-4, Tensile Test. Micrographs show significant fiber pullout with little oxidation.

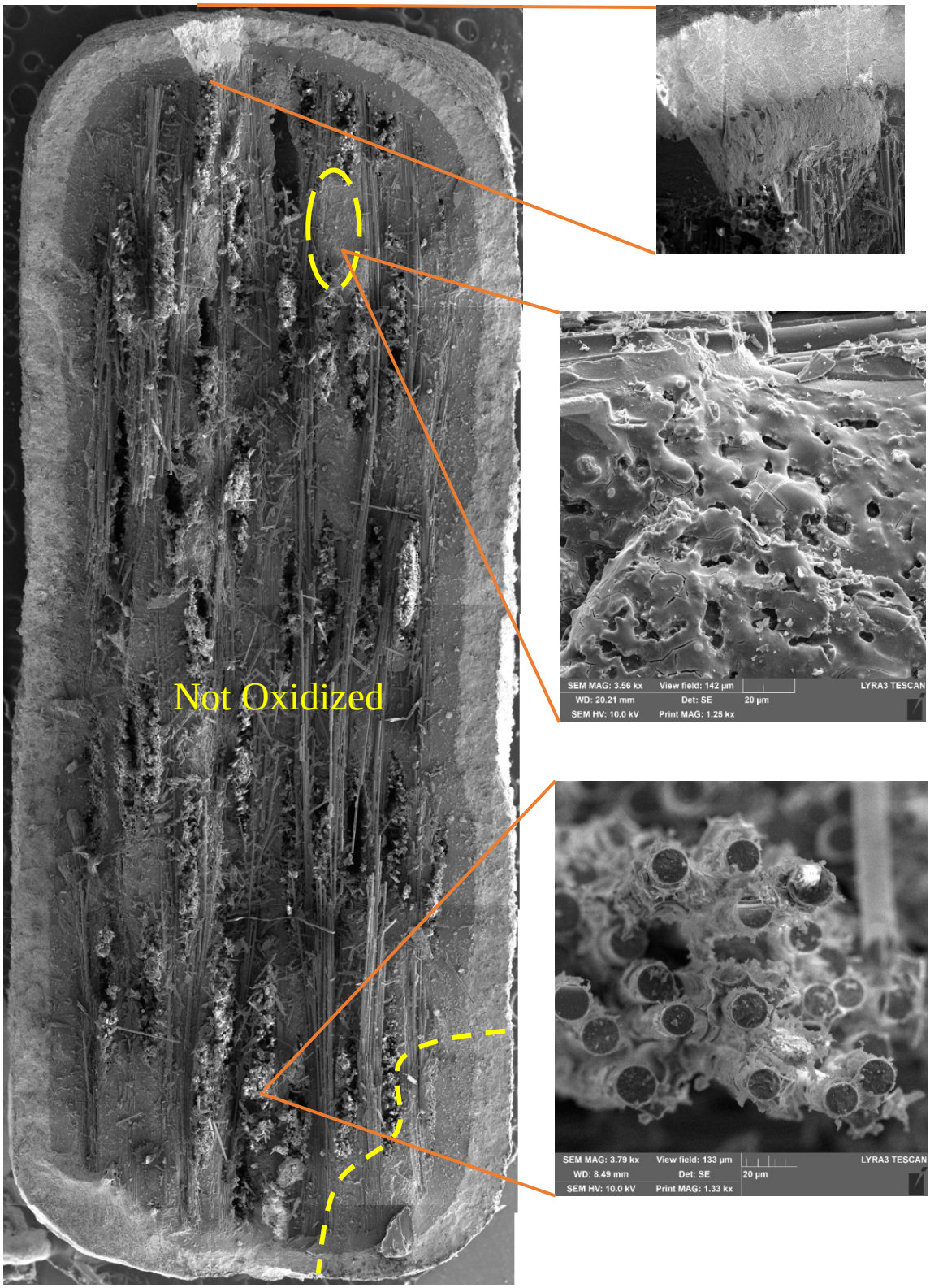

Figure 4.17: EBC/Hi-N/MI-SiC specimen P15001-12, tensile test in air at 1200ºC. Micrographs show significant fiber pullout with little oxidation but some matrix rich areas. The EBC is also shown filling a surface flaw.

4.6.3 Fatigue Test Specimen Microscopy

The following section discusses the basic fracture surface topography and standard features of specimens which survived until run-out and specimens which fractured during fatigue testing. Both air and steam conditions are represented. All fracture surfaces shown are the lower half of the dog bone composite which was removed from the furnace following failure to prevent prolonged exposure to the highly oxidizing environment.

Optical and SEM micrographs for specimen P15002-7 which was subjected to tension-tension fatigue testing to failure after 8,869 cycles at 1200ºC in air with a maximum stress of 130 MPa are shown in Figure 4.18 and Figure 4.19. Intermittent fiber pullout is present, but the fibers are fractured very low to the surface appearing as a nearly monolithic ceramic fracture surface when viewed optically. The surface shows multiple large internal surface flaws due to poor processing; four flaws are within close proximity which further weakens the material. The surface shows very little oxidation of fibers but suffers from large matrix rich areas between fiber brushes.

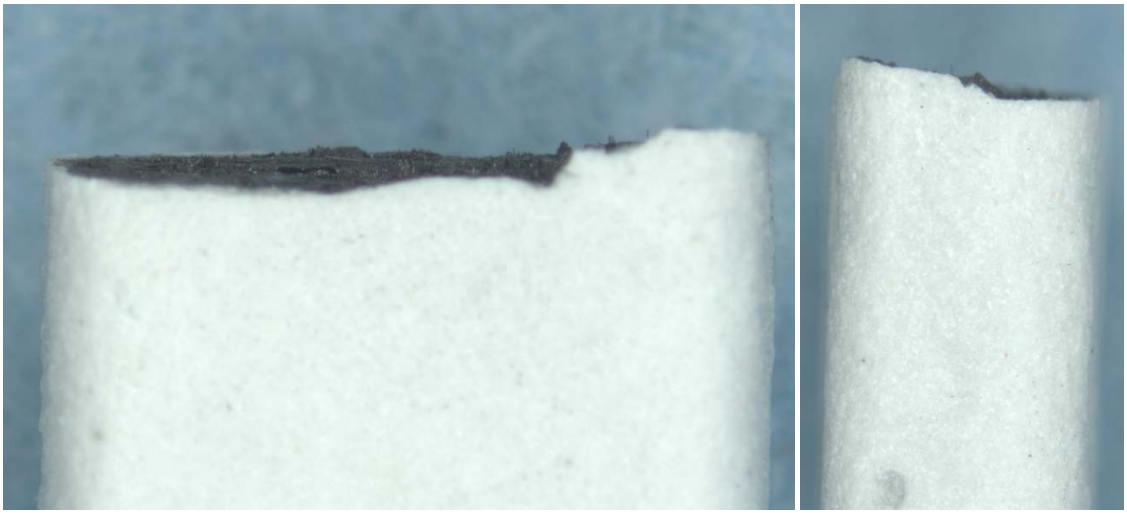

Figure 4.18: Optical micrograph of specimen P15002-7 subjected to tension-tension fatigue testing to failure at 1200ºC in air. σ_{max} = 130 MPa, N_f = 8,869 cycles

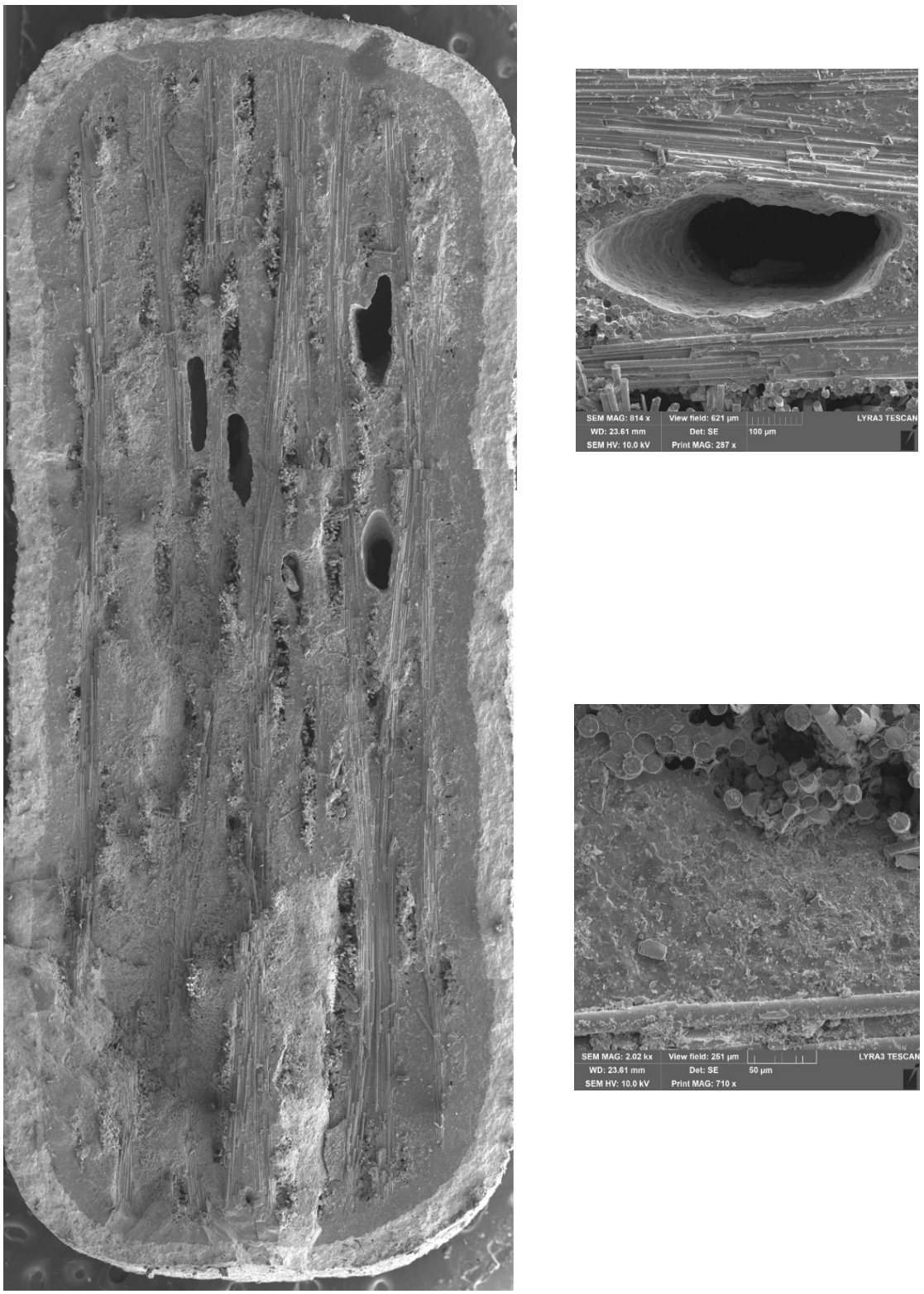

Figure 4.19: SEM micrograph of specimen P15002-7 subjected to tension-tension fatigue testing to failure at 1200ºC in air. σ_{max} = 130 MPa, N_f = 8,869 cycles

Optical and SEM micrographs for specimen P15006-13 which was subjected to tension-tension fatigue testing to run-out at 200,000 cycles at 1200ºC in air with a maximum stress of 110 MPa are shown in Figure 4.20 and Figure 4.21. Fiber pullout is present across the entire fracture surface and is far more pronounced than specimen P15002-7 which did not reach run-out. The fracture surface internal voids are also smaller and less localized than P15002-7 since they are mostly caused by fiber pullout as opposed to processing. Large matrix rich areas can be seen close to the interface of the composite and bond coat but become less common further into the material. As expected, microcracks are present throughout the matrix phase.

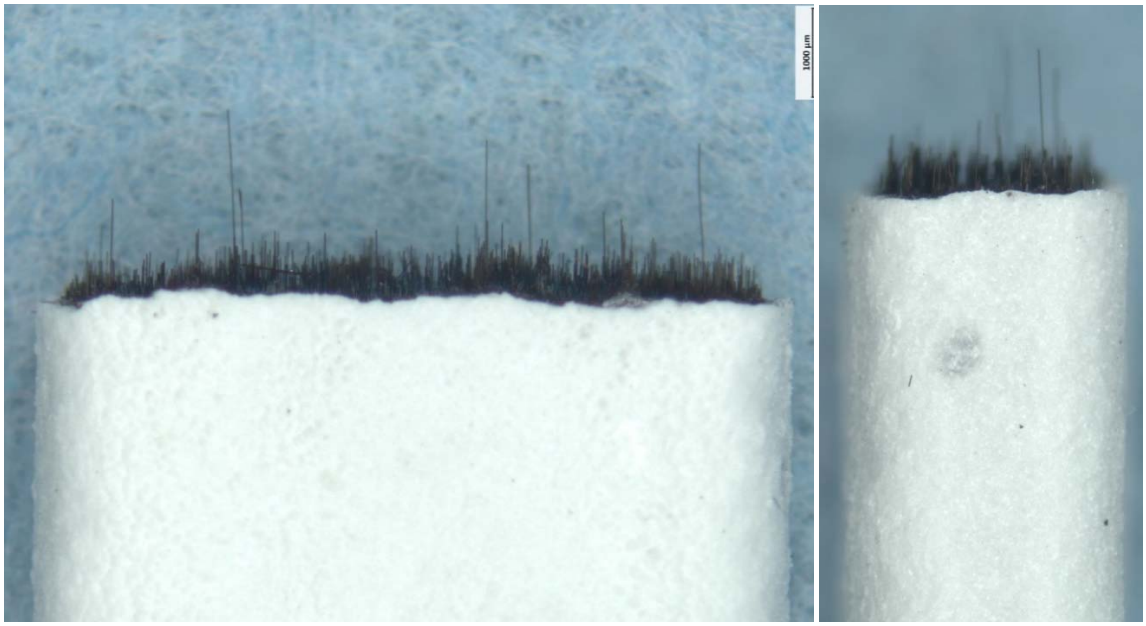

Figure 4.20: Optical micrograph of specimen P15006-13 subjected to tension-tension fatigue testing to run-out at 1200ºC in air. Specimen brought to failure by a monotonic tension test following run-out. σ_{max} = 110 MPa, N_f > 200,000 cycles

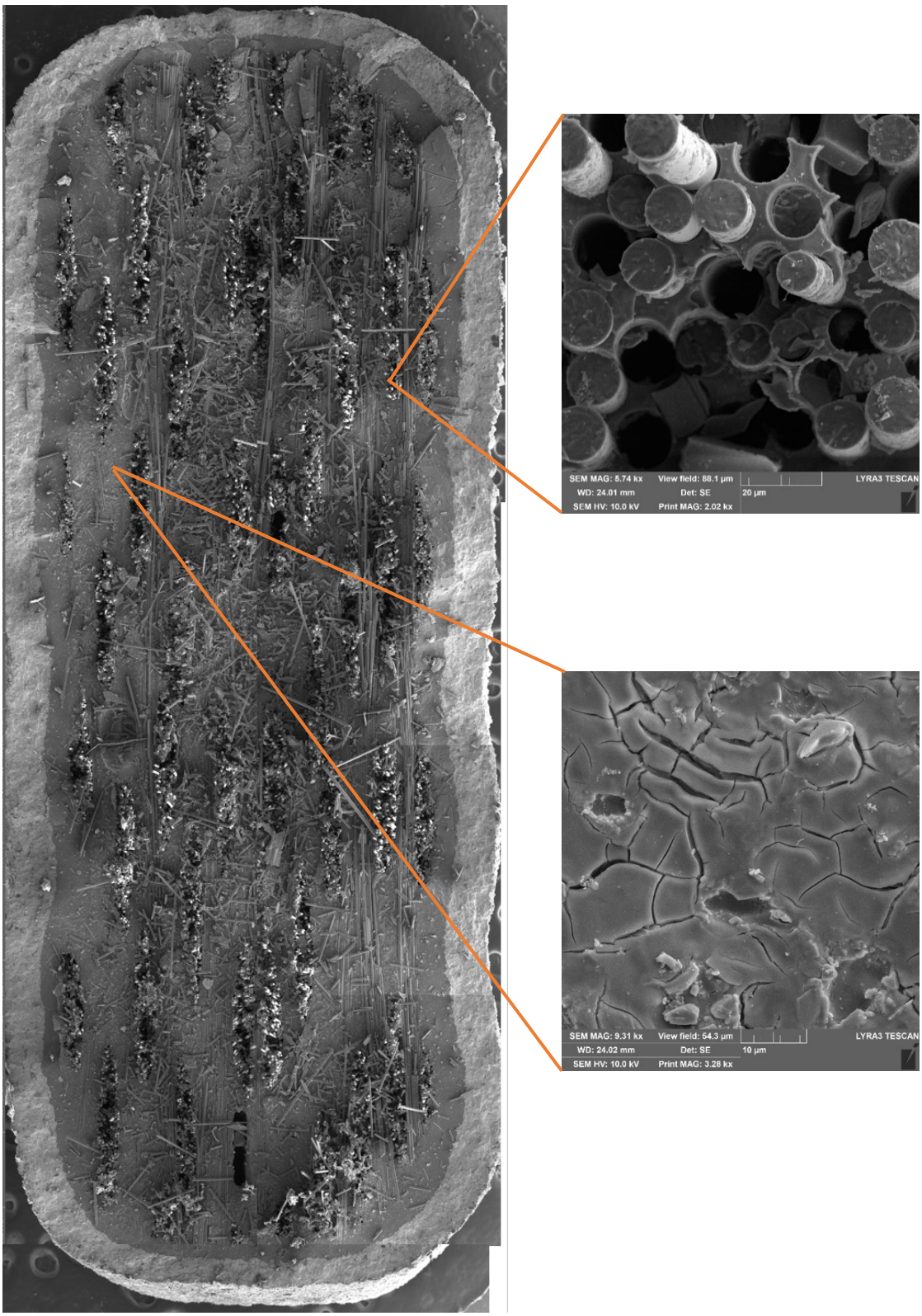

Figure 4.21: SEM micrograph of specimen P15006-13 subjected to tension-tension fatigue testing to run-out at 1200ºC in air. Specimen brought to failure by a monotonic tension test following run-out. σ_{max} = 110 MPa, N_f > 200,000 cycles

Optical and SEM micrographs for specimen P15005-4 which was subjected to tension-tension fatigue testing to failure after 19,781 cycles at 1200ºC in steam with a maximum stress of 135 MPa are shown in Figure 4.22 and Figure 4.23. Considerable fiber pullout is present on the surface. The SEM micrograph highlights the intermittent pullout surrounded by matrix rich areas. Additionally, a portion of the fracture surface has oxidized. Multiple processing flaws are present in the interior of the CMC around the fibrous fracture. The fiber pullout is straight and linear causing minimal debris when compared to specimens such as P15006-13.

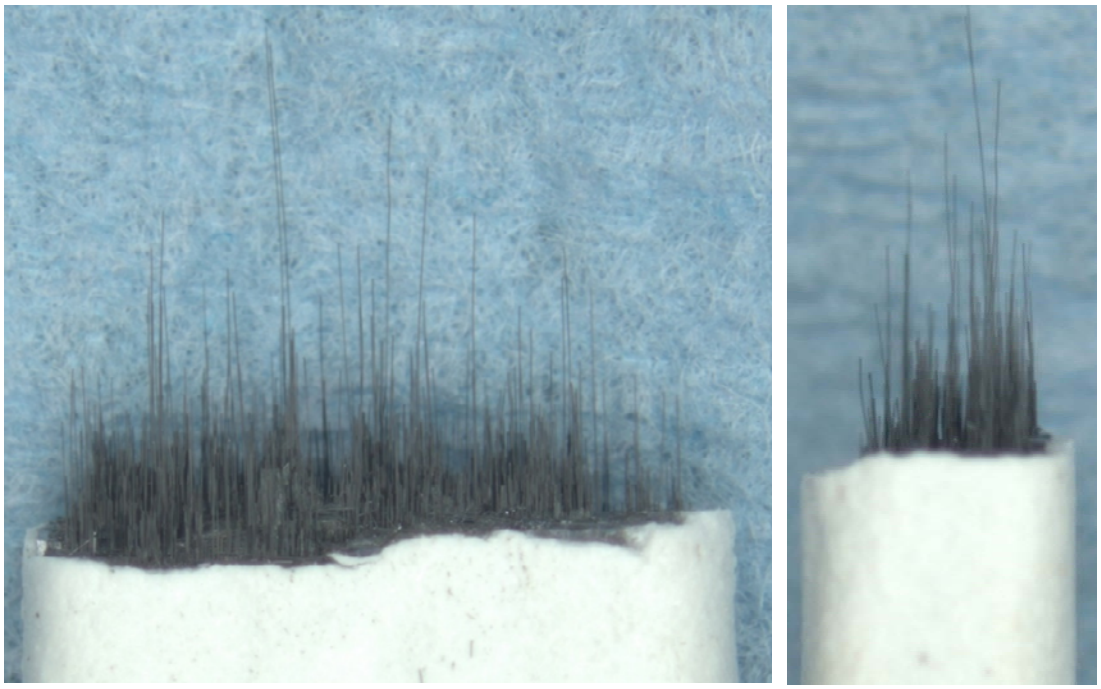

Figure 4.22: Optical micrograph of specimen P15005-4 subjected to tension-tension fatigue testing to failure at 1200ºC in steam. σ_{max} = 135 MPa, N_f = 19,781 cycles

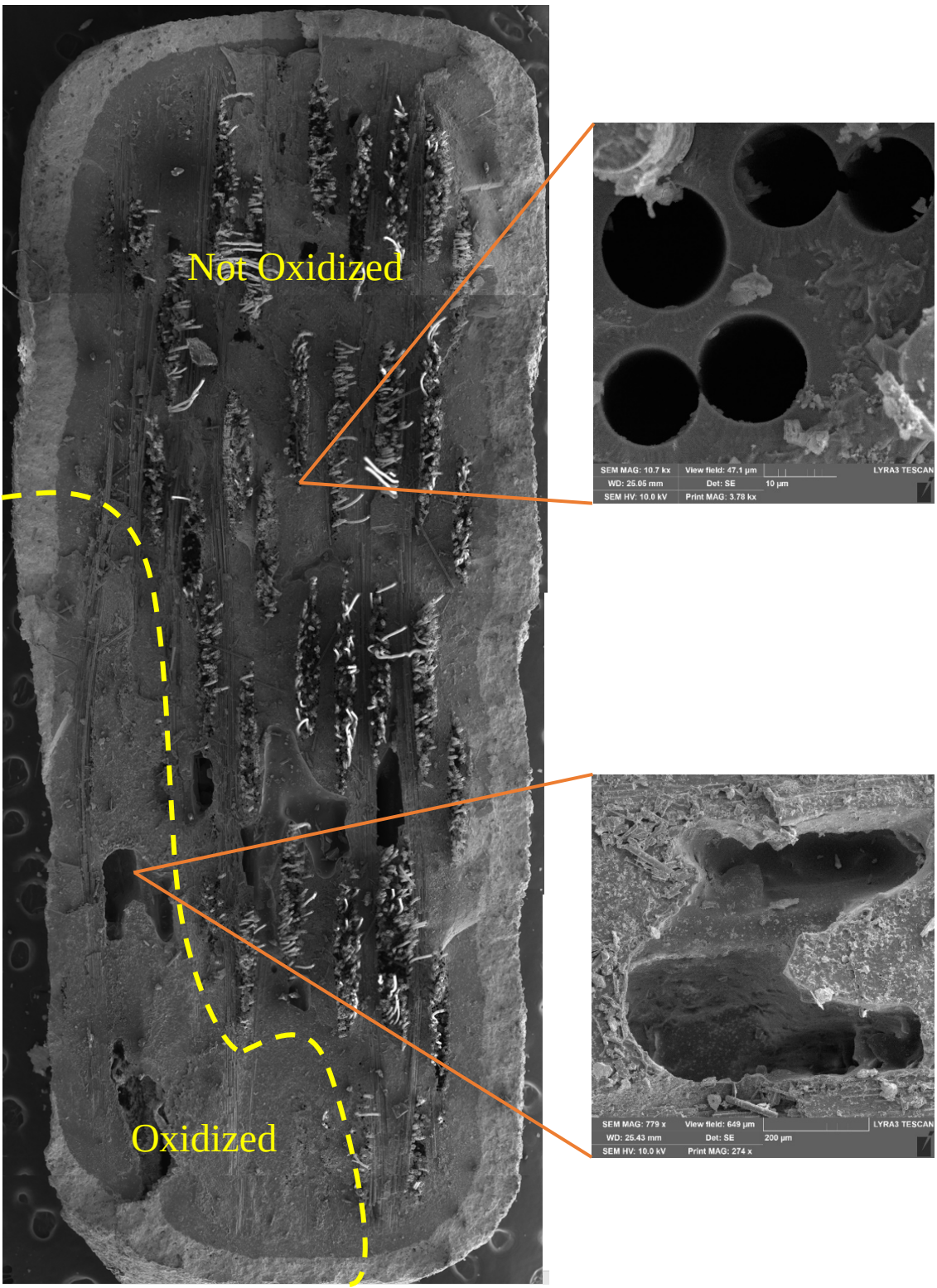

Figure 4.23: SEM micrograph of specimen P15005-4 subjected to tension-tension fatigue testing to failure at 1200ºC in steam. σ_{max} = 135 MPa, N_f = 19,781 cycles

Optical and SEM micrographs for specimen P15005-5 which was subjected to tension-tension fatigue testing to run-out at 200,000 cycles at 1200ºC in steam with a maximum stress of 120 MPa are shown in Figure 4.24 and Figure 4.25. The fracture surface resembles specimen P15005-4 in multiple ways including significant fiber pullout. However, P15005-5 has more localized and isolated areas of oxidation on the fracture surface and benefits from fewer matrix rich areas. The fracture surface also displays internal voids of similar size and frequency to the previously examined specimens.

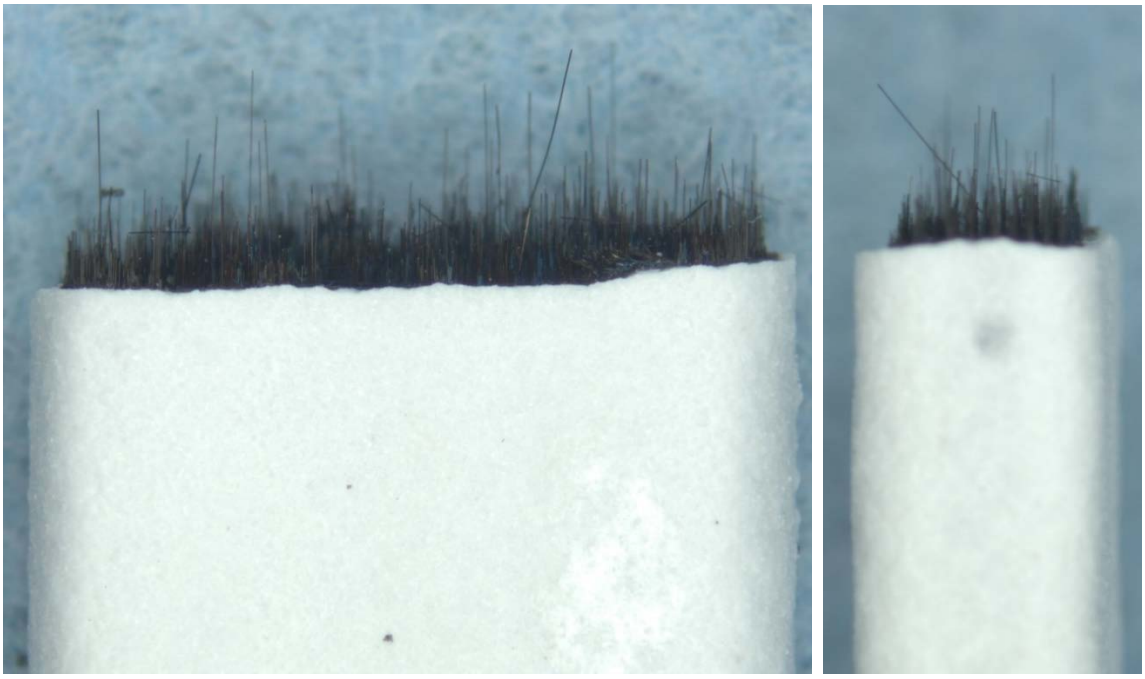

Figure 4.24: Optical micrograph of specimen P15005-5 subjected to tension-tension fatigue testing to run-out at 1200ºC in steam. Specimen brought to failure by a monotonic tension test following run-out. σ_{max} = 120 MPa, N_f > 200,000 cycles

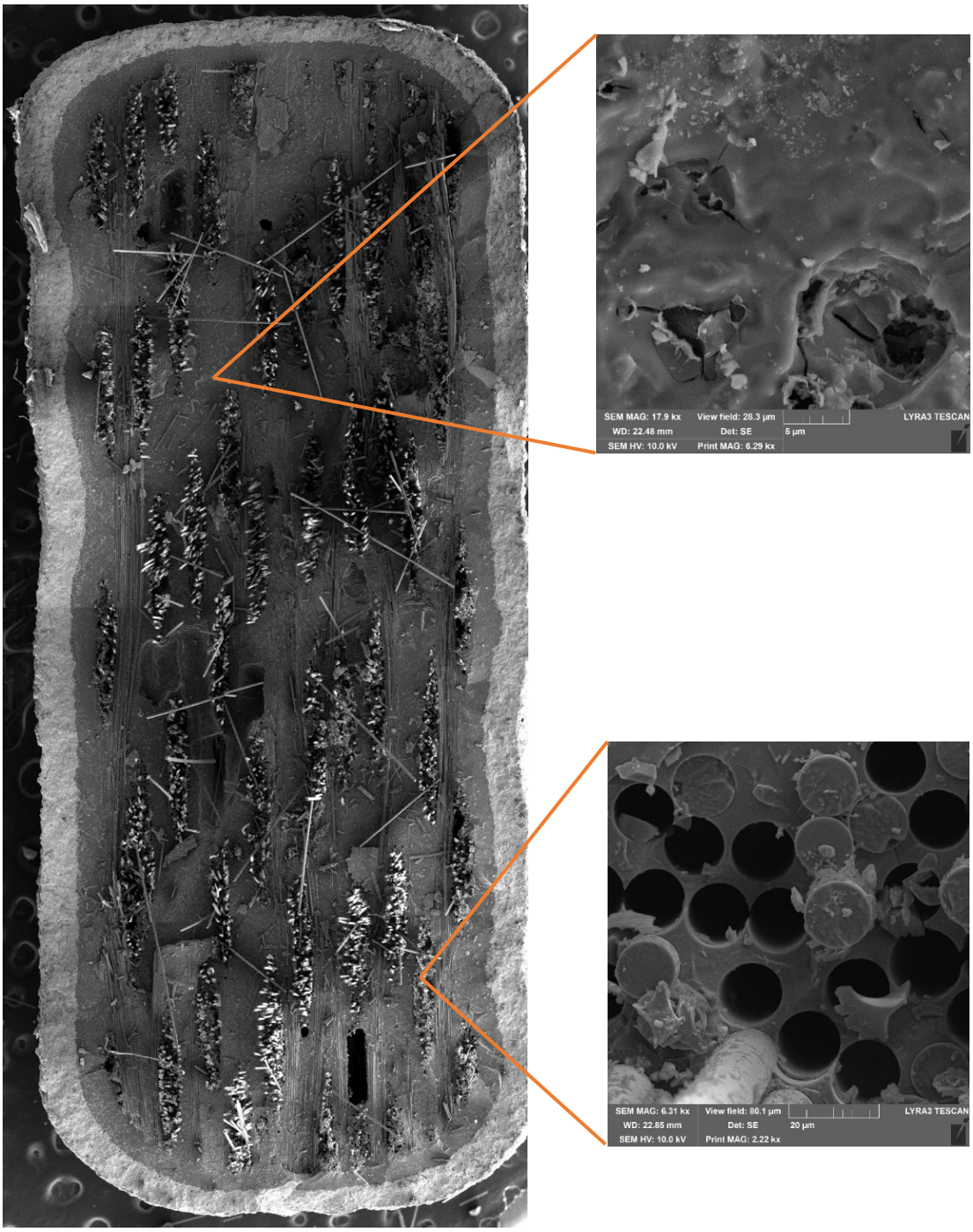

Figure 4.25: Optical micrograph of specimen P15005-5 subjected to tension-tension fatigue testing to run-out at 1200ºC in steam. Specimen brought to failure by a monotonic tension test following run-out. σ_{max} = 120 MPa, N_f > 200,000 cycles

4.6.4 Comparison of Microstructure to Uncoated Specimens

Figure 4.26-Figure 4.28 provide comparisons of the present work on EBC/Hi-N/MI-SiC and the work performed by Boucher [25] on uncoated Hi-N/MI-SiC. Boucher discovered that oxidation was confined to the external regions of the fracture surface on the specimen which achieved run-out in air. The same type of specimen coated with an EBC which achieved run-out displays a very similar microstructure with fiber pullout as the dominant structure on the interior of the fracture surface. Thus, it is concluded that oxidation embrittlement was not a significant issue for these test runs and the threshold stress level for subcritical crack growth was not achieved.

Figure 4.27 compares uncoated and coated specimens at similar high maximum stress levels (σ_{max} = 140 MPa, σ_{max} = 130 MPa) which exhibited short fatigue life (N_f = 2,200, N_f = 8,869). Processed identically, both specimens show large internal flaws. The specimen coated with an EBC displays less prominent fiber tow pullout. Both specimens suffer from large regions of oxidation which indicates oxidation embrittlement and the prevention of large-scale fiber pullout across the fracture surface leading to early catastrophic failure.

The comparison of run-out specimens in steam shown in Figure 4.28 displays very little difference between the specimen with an EBC and the one without. The coated specimen has less localized oxidized fracture surface area but has intermittent oxidation in and around fiber tows.

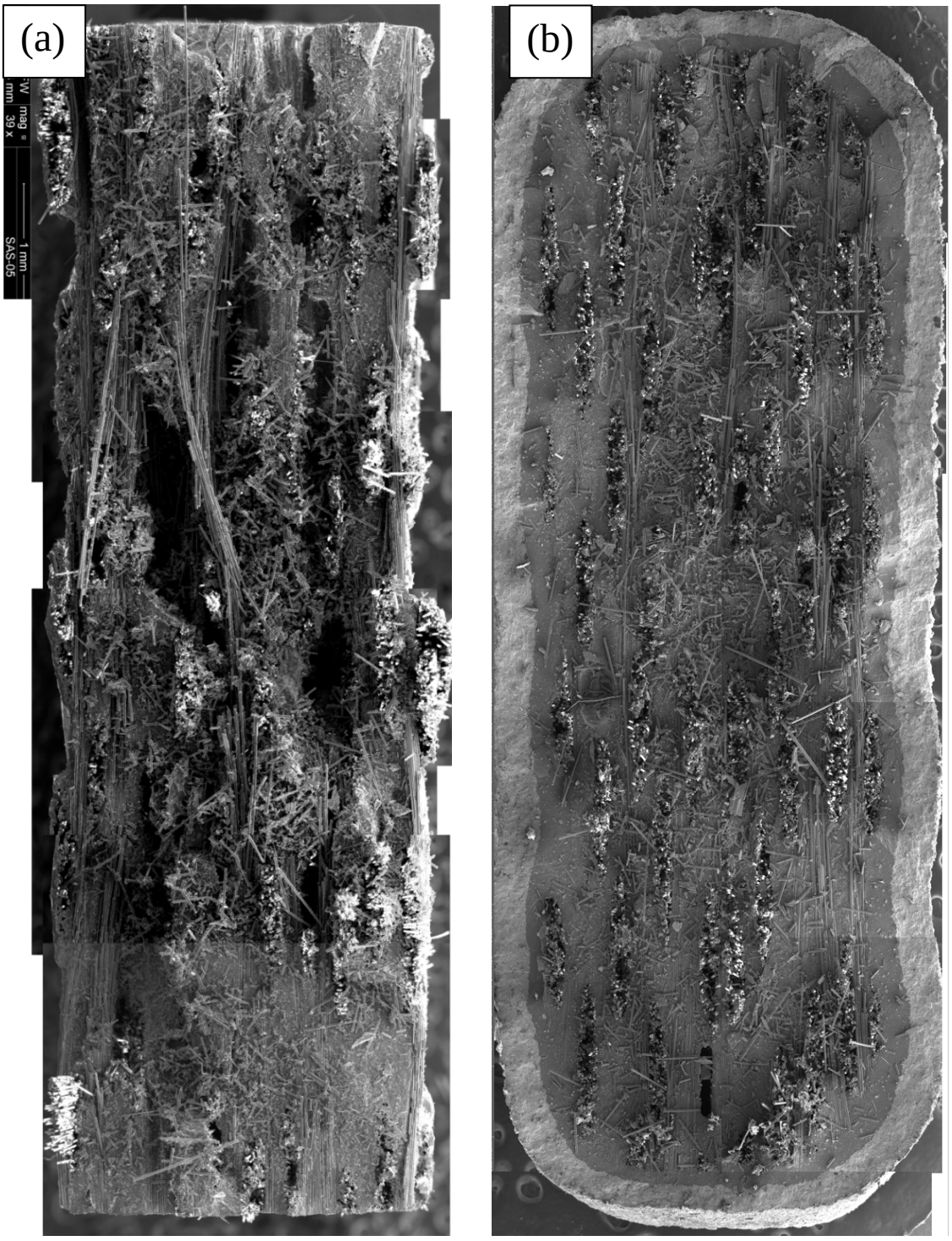

Figure 4.26: Micrographs of uncoated Hi-N/MI-SiC (a) compared to EBC/Hi-N/MI-SiC (b). Both specimens were subjected to fatigue testing at 1200ºC and reached run-out (N_f > 200,000 cycles) in air

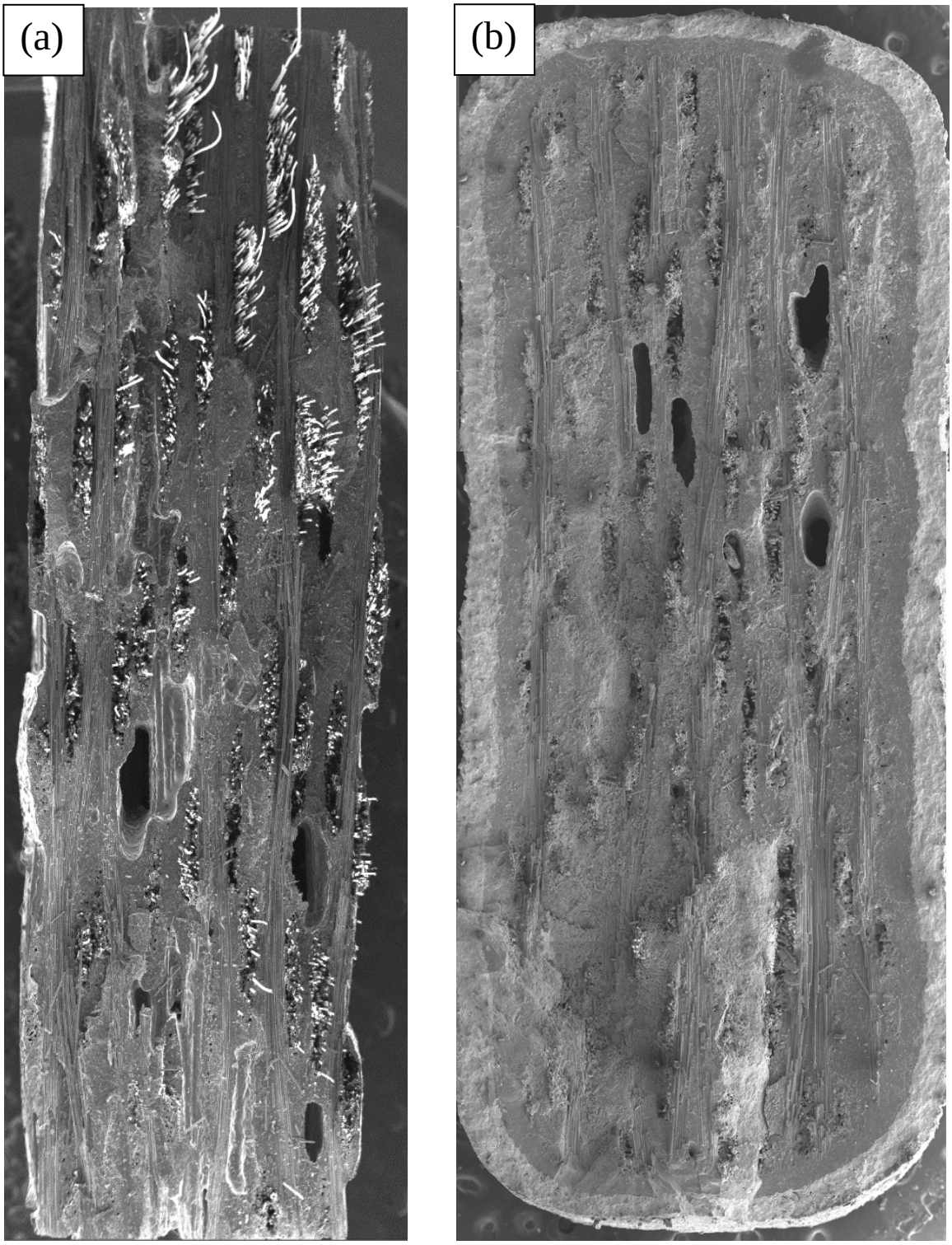

Figure 4.27: Micrographs of uncoated Hi-N/MI-SiC, σ_{max} = 140 MPa, N_f = 2,200 cycles (a) compared to EBC/Hi-N/MI-SiC, σ_{max} = 130 MPa, N_f = 8,869 cycles (b). Both specimens were subjected to fatigue testing at 1200ºC until failure

Figure 4.28: Micrographs of uncoated Hi-N/MI-SiC (a) compared to EBC/Hi-N/MI-SiC (b). Both specimens were subjected to fatigue testing at 1200ºC and reached run-out (N_f > 200,000 cycles) in steam

Chapter 5 Conclusions and Recommendations

5.1 Conclusions

Prior to the fatigue behavior study explored in this research, tensile tests were performed in air at 1200°C to determine the tensile properties of a melt-infiltrated SiC/SiC composite with an ytterbium disilicate environmental barrier coating that was applied following grit-blasting. The UTS was 200 MPa, the elastic modulus was 120 GPa, the proportional limit was 119 MPa, and the failure strain was 0.45% [27]. Notably, the tensile test specimens which were grit-blasted showed significantly decreased tensile properties compared to the virgin specimens of the same composite layup studied in previous research efforts. Boucher [25] reported a UTS of 239 MPa, an elastic modulus of 217 GPa, a proportional limit of 135 MPa, and a failure strain of 0.41%.

The tension-tension fatigue behavior of EBC/Hi-N/MI-SiC was examined in this study to determine the benefits, if any, of applying an EBC to a melt-infiltrated SiC/SiC composite. Fatigue data was collected on tests operating at 1200°C in laboratory air and steam conditions with a loading frequency of 1 Hz and maximum stresses ranging from 110-140 MPa. Fatigue run-out was defined as 200,000 cycles and was achieved at 120 MPa (~55% UTS) in air and 110 MPa (~60% UTS) in steam. Research on uncoated specimens measured run-out at 110 MPa (~50% UTS) in air and 120 MPa (~45% UTS) in steam [25]. Maximum stress levels are similar although the coated specimens were able to reach run-out closer to their measured UTS. Although the grit-blasting process decreased the overall tensile properties, it did not have a significant effect on the maximum stress at which run-out is achieved. Additionally, the EBC prevented the environment from having a significant effect on the fatigue performance of the CMC.

Boucher's [25] results showed a clear decrease in fatigue performance in the presence of steam which did not occur in the coated EBC/Hi-N/MI-SiC.

The EBC/Hi-N/MI-SiC specimen fatigue performance displayed a more gradual decrease in fatigue life with an increase in maximum stress compared to the uncoated specimens. In the case of the uncoated CMC, the cycles to failure were approximately two orders of magnitude less than run-out when a slightly greater maximum stress was applied. The cyclic crack threshold stress level for EBC/Hi-N/MI-SiC was between 110 MPa to 120 MPa in air and between 120 MPa and 130 MPa in steam. Similarly, Boucher [25] reports uncoated specimen threshold stress levels of 120 MPa to 130 MPa in air and 110 MPa to 120 MPa in steam. The cyclic crack threshold stress levels are similar but EBC/Hi-N/MI-SiC displays a larger region II of the crack growth rate versus stress intensity factor plot. This may be due to the filling of surface flaws with EBC and the resulting decrease in regions of high stress intensity on the surface of the CMC since the stress intensity factor range (ΔK) is dependent upon crack geometry. However, the prevalence of internal processing voids that cannot be filled remains a primary factor in the failure of the material.

Regarding retained tensile properties after run-out, EBC/Hi-N/MI-SiC outperformed the uncoated specimen strength with a ~0% decrease in air and ~1% decrease in steam as opposed to ~3% decrease in air and ~10-18% decrease in steam [25]. One coated specimen only retained 31% of its stiffness in steam which can be similarly seen in the results of the uncoated material tested in steam where only ~38% stiffness is maintained. The other two coated specimens which achieved run-out fully maintained their stiffness.

The EBC effectiveness is demonstrated in all but one test case to stymie oxidation of the composite. This led to increased lifetimes at higher maximum fatigue stresses in regards to %UTS compared to the uncoated specimens. The EBC also prevented the aggressive steam environment from dramatically affecting the lifetime of the composite. However, the benefits produced by the EBC are hindered by the detrimental grit-blasting process prior to EBC application which degrades the tensile and fatigue properties of the material. Finally, the melt-infiltration process of EBC/Hi-N/MI-SiC production leaves significant voids in the microstructure. For this reason the targeted maximum fatigue stress is consistently exceeded due to the reduced specimen cross-sectional area.

5.2 Recommendations

Due to the damage induced by grit-blasting the composite specimens prior to EBC application, it is recommended that evaluations be performed on more robust composites which do not suffer from so many large internal flaws. The EBC application does show benefits to the material fatigue life specifically when examined as the maximum applied stress as a percentage of ultimate tensile strength. Additionally, a larger number of samples would need to be tested to fully understand the fatigue behavior of the composite since this current study was limited in scope.

Appendix A – Optical Micrographs of Specimen Fracture Surfaces.

Figure A 1: Fracture surfaces of specimen P15002-5, tested in fatigue at 1200°C in air. σ_{max} = 120 MPa, N_f = 100,128 cycles

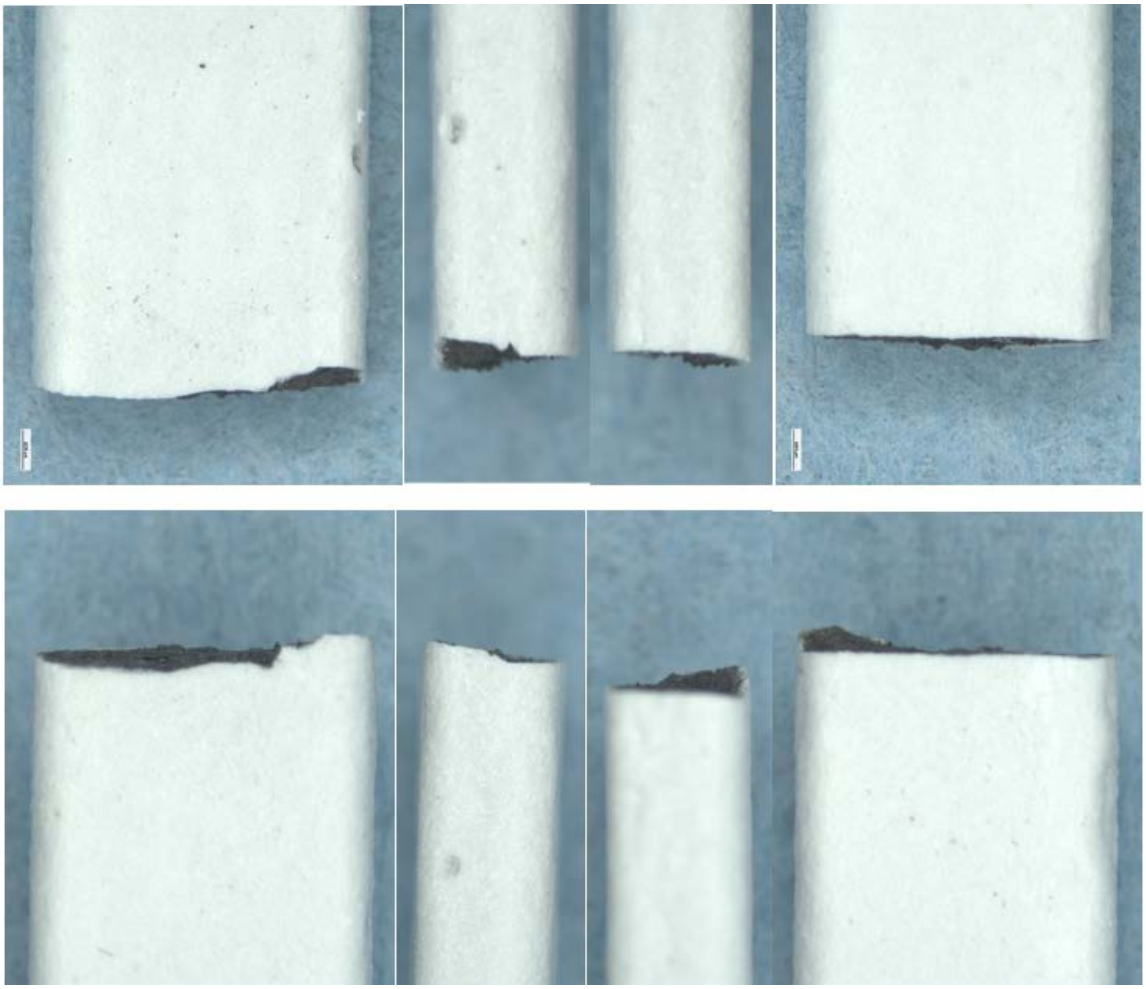

Figure A 2: Fracture surfaces of specimen P15002-7, tested in fatigue at 1200°C in air. σ_{max} = 130 MPa, N_f = 8,869 cycles

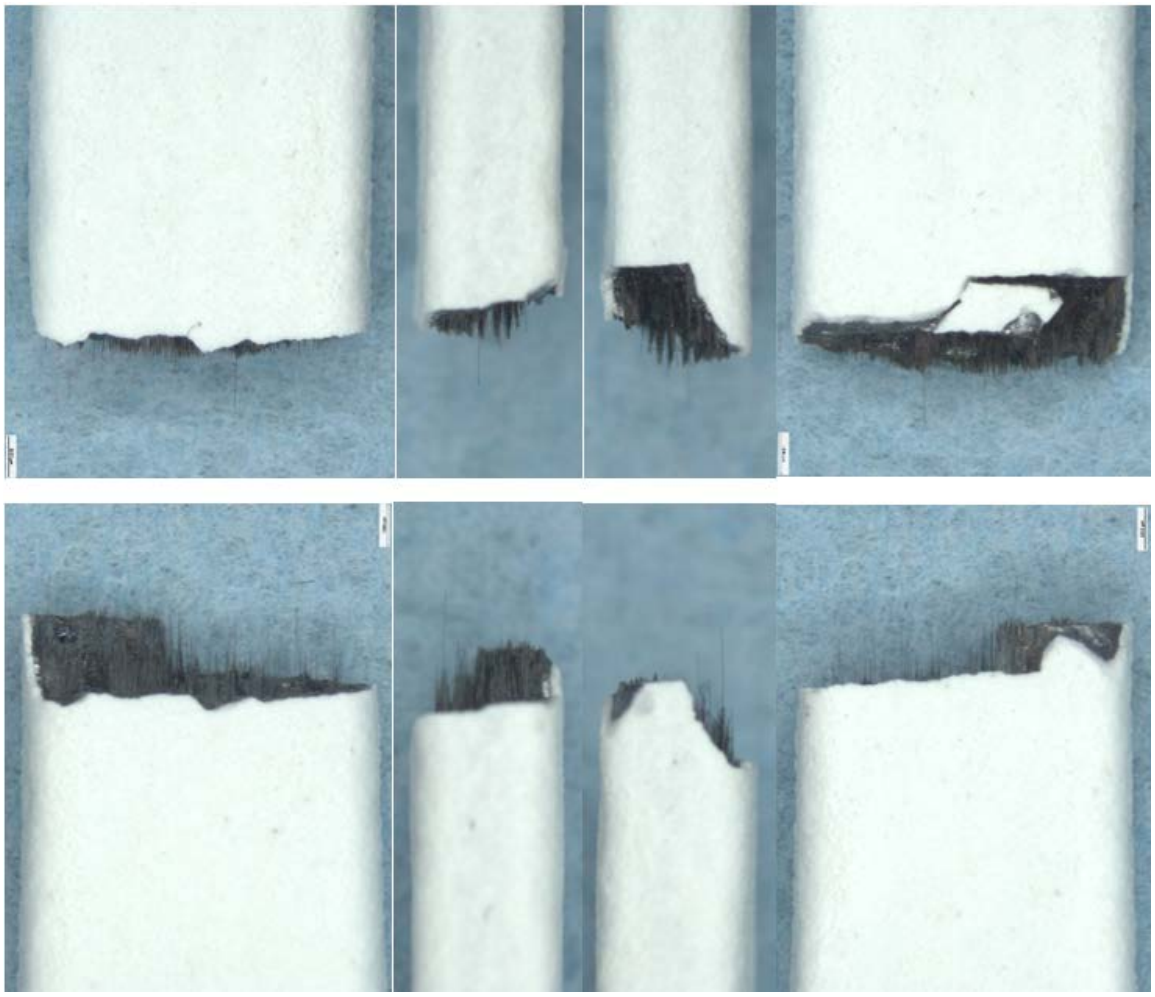

Figure A 3: Fracture surfaces of specimen P15004-7, tested in fatigue at 1200°C in air. σ_{max} = 140 MPa, N_f = 627 cycles

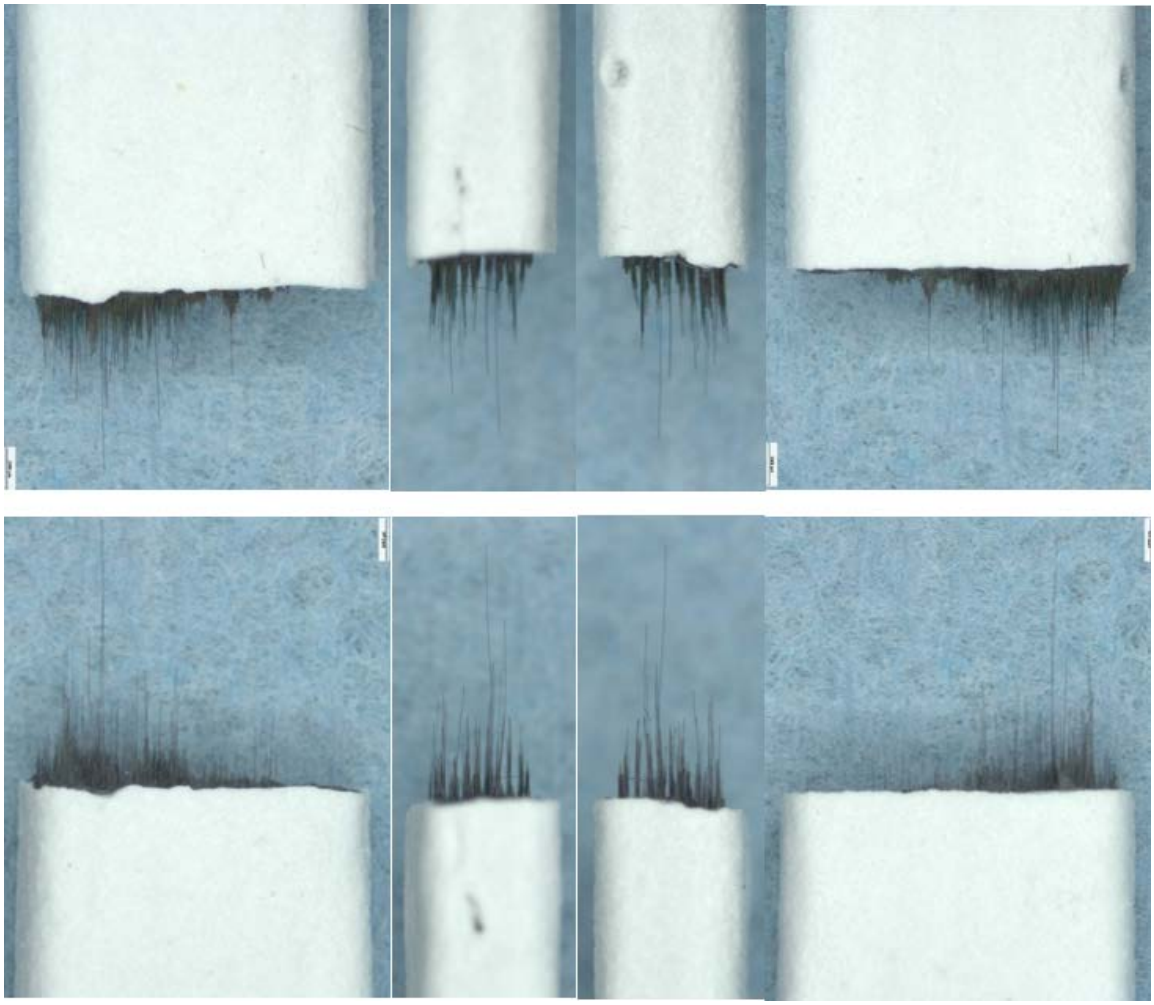

Figure A 4: Fracture surfaces of specimen P15004-8, tested in fatigue at 1200°C in air. σ_{max} = 110 MPa, N_f = 29,547 cycles

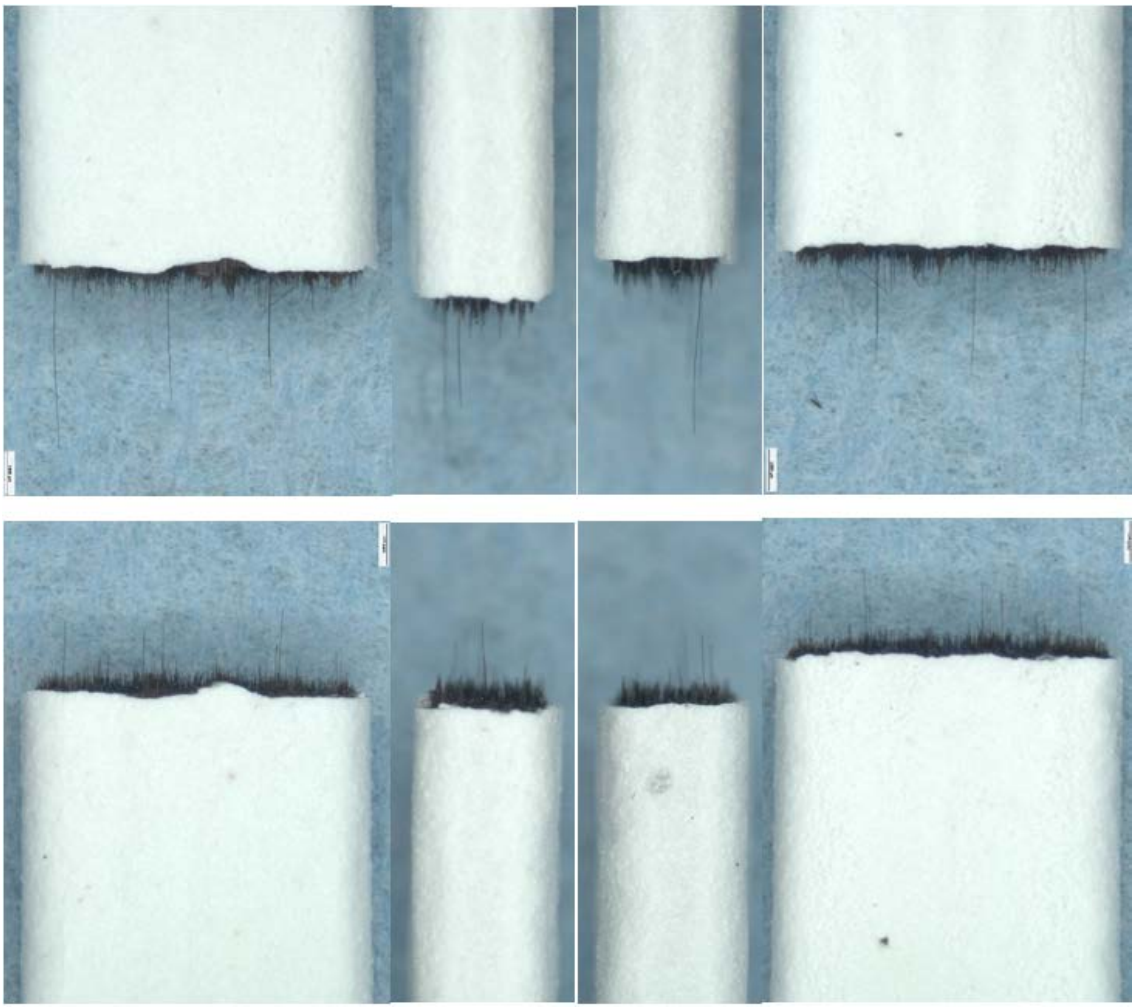

Figure A 5: Fracture surfaces of specimen P15006-13, tested in fatigue at 1200°C in air. σ_{max} = 110 MPa, N_f > 200,000 cycles

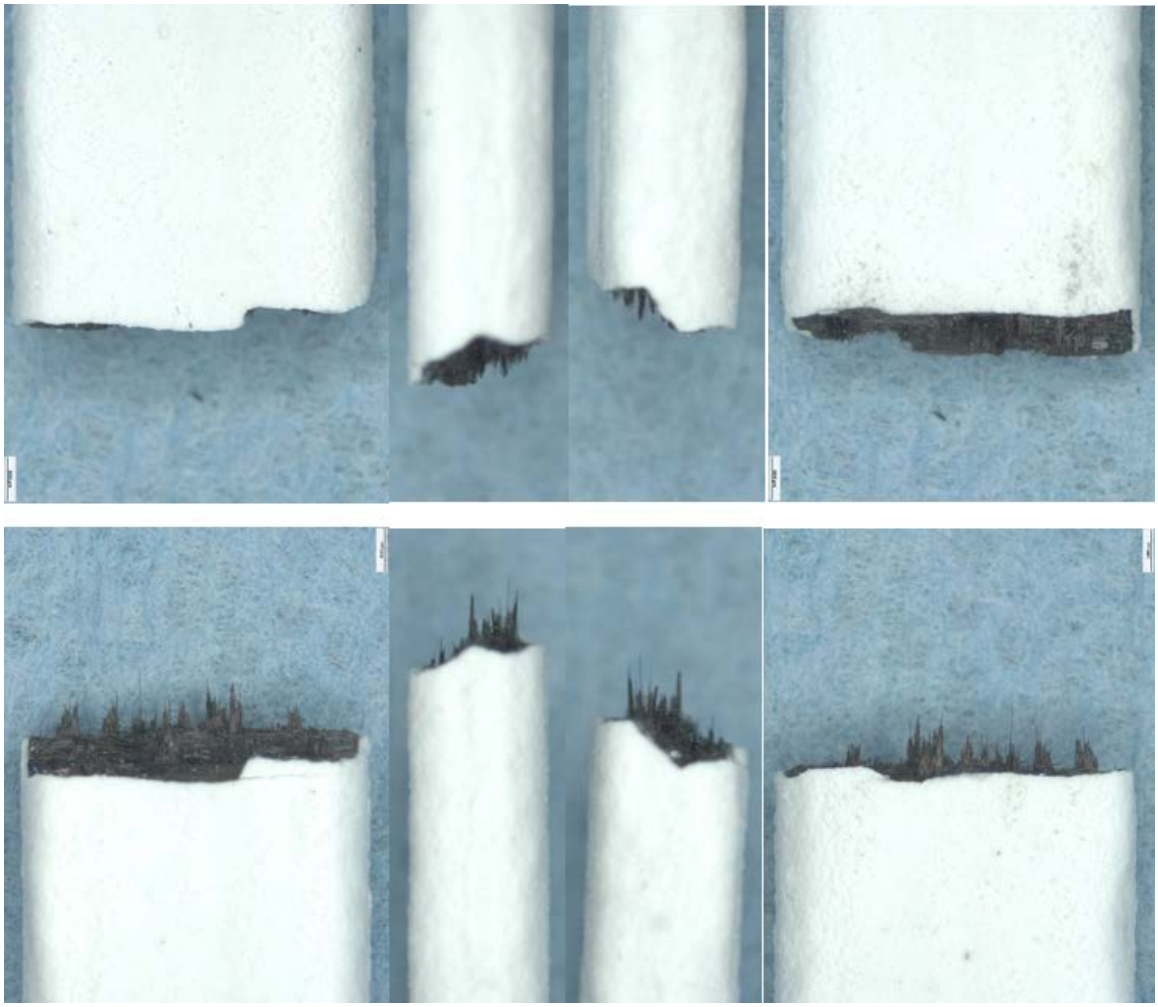

Figure A 6: Fracture surfaces of specimen P15001-13, tested in fatigue at 1200°C in steam.
σ_{max} = 140 MPa, N_f = 342 cycles

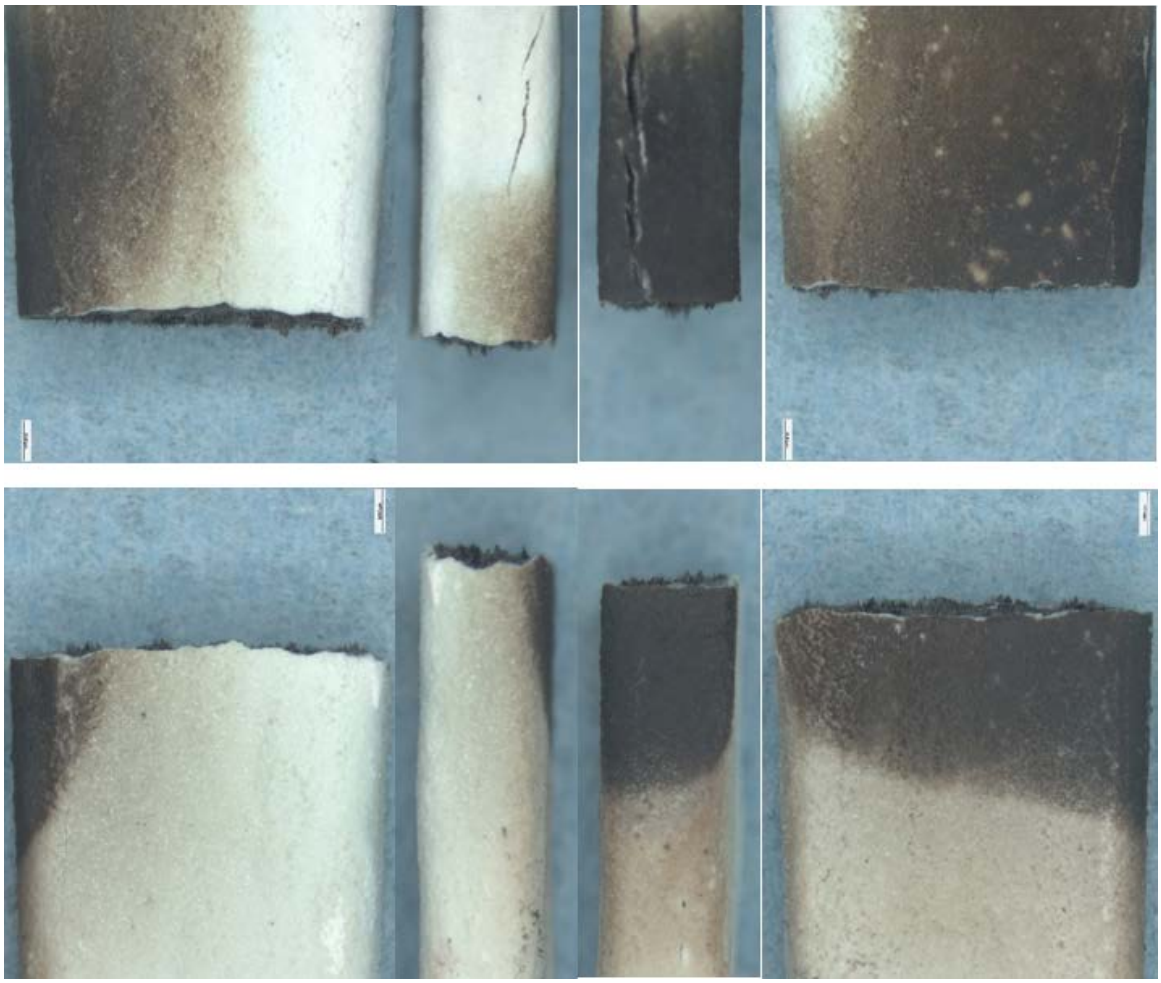

Figure A 7: Fracture surfaces of specimen P15005-2, tested in fatigue at 1200°C in steam.
σ_{max} = 135 MPa, N_f > 200,000 cycles

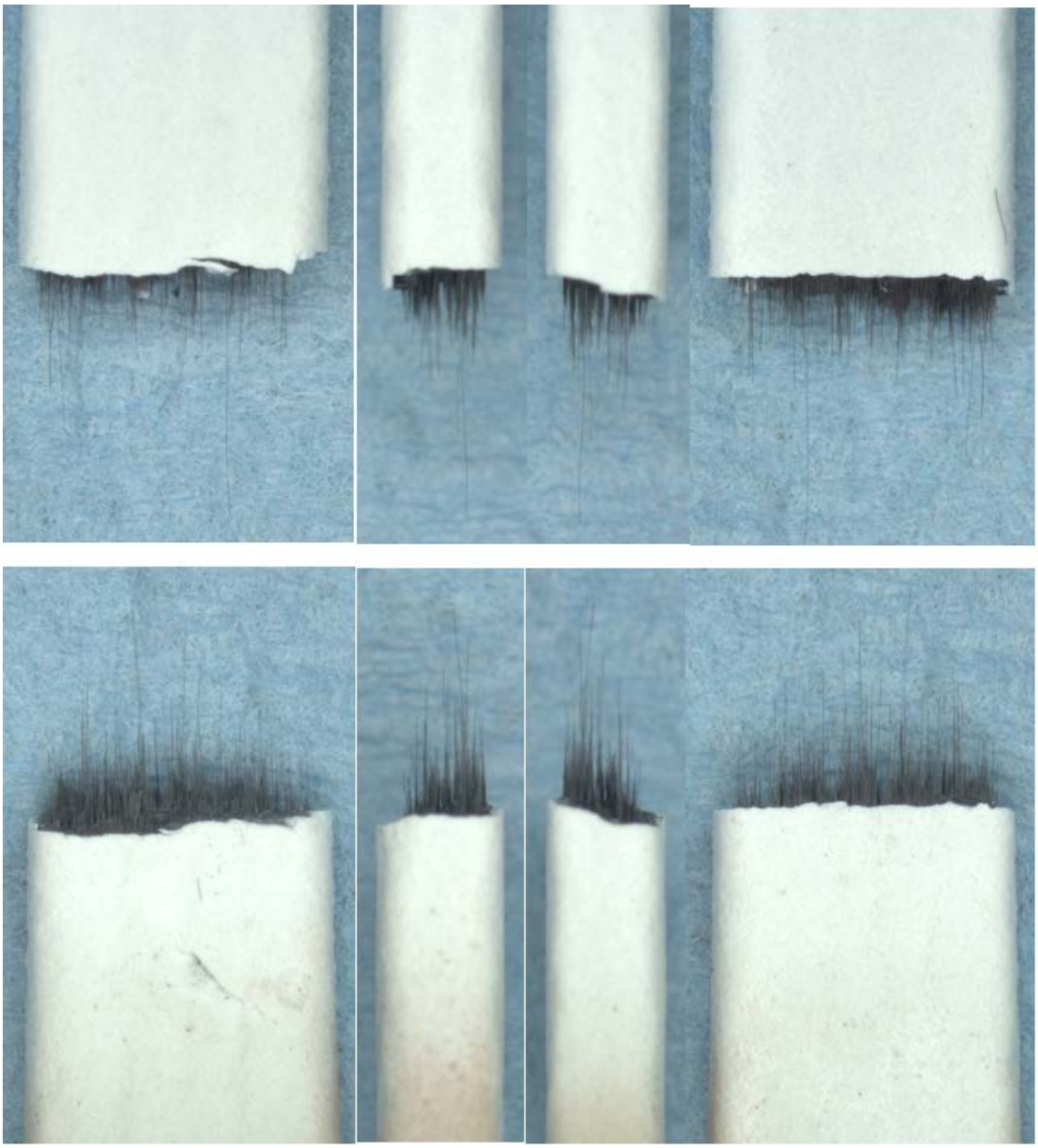

Figure A 8: Fracture surfaces of specimen P15005-4, tested in fatigue at 1200°C in steam.
σ_{max} = 135 MPa, N_f = 19,781 cycles

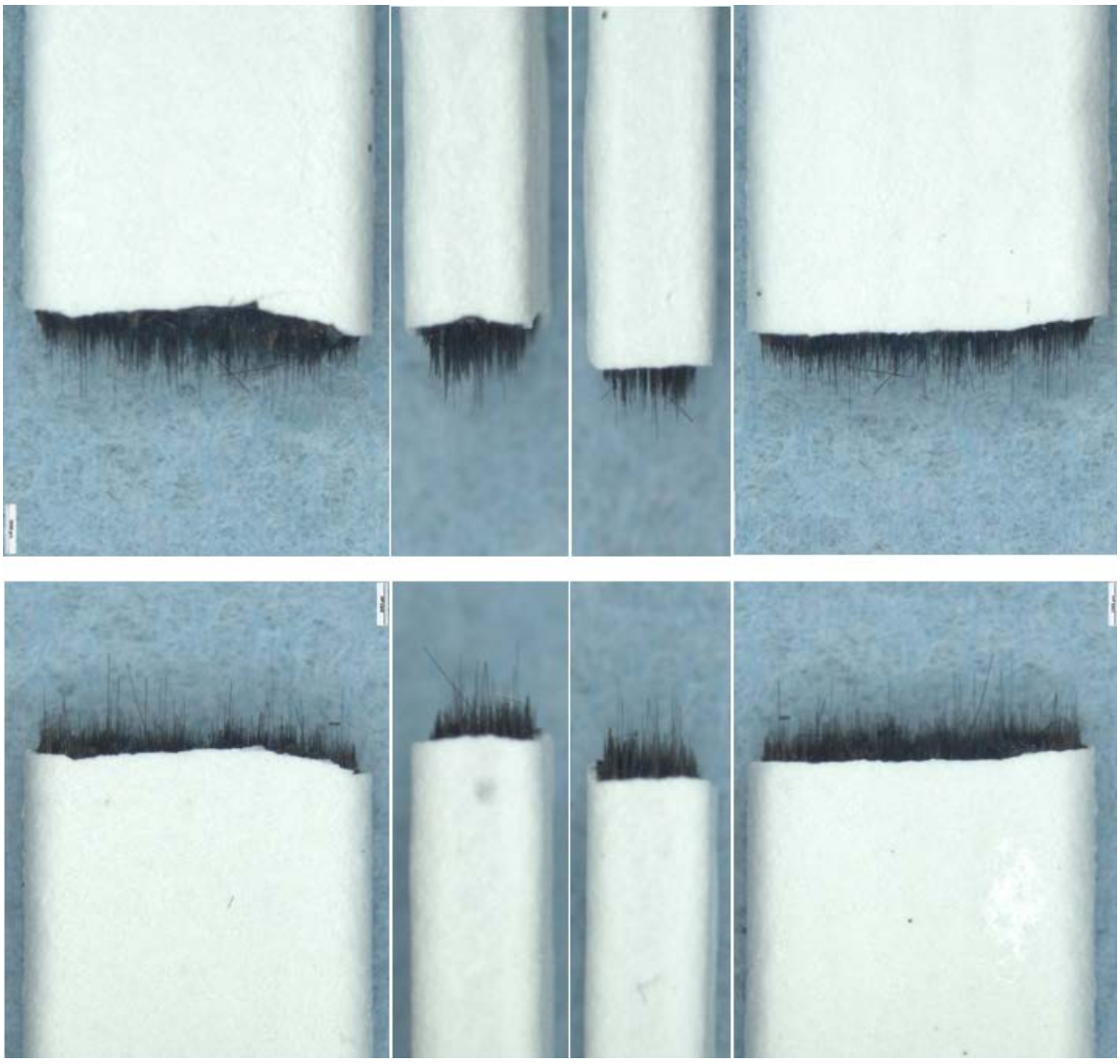

Figure A 9: Fracture surfaces of specimen P15005-5, tested in fatigue at 1200°C in steam.
σ_{max} = 120 MPa, N_f > 200,000 cycles

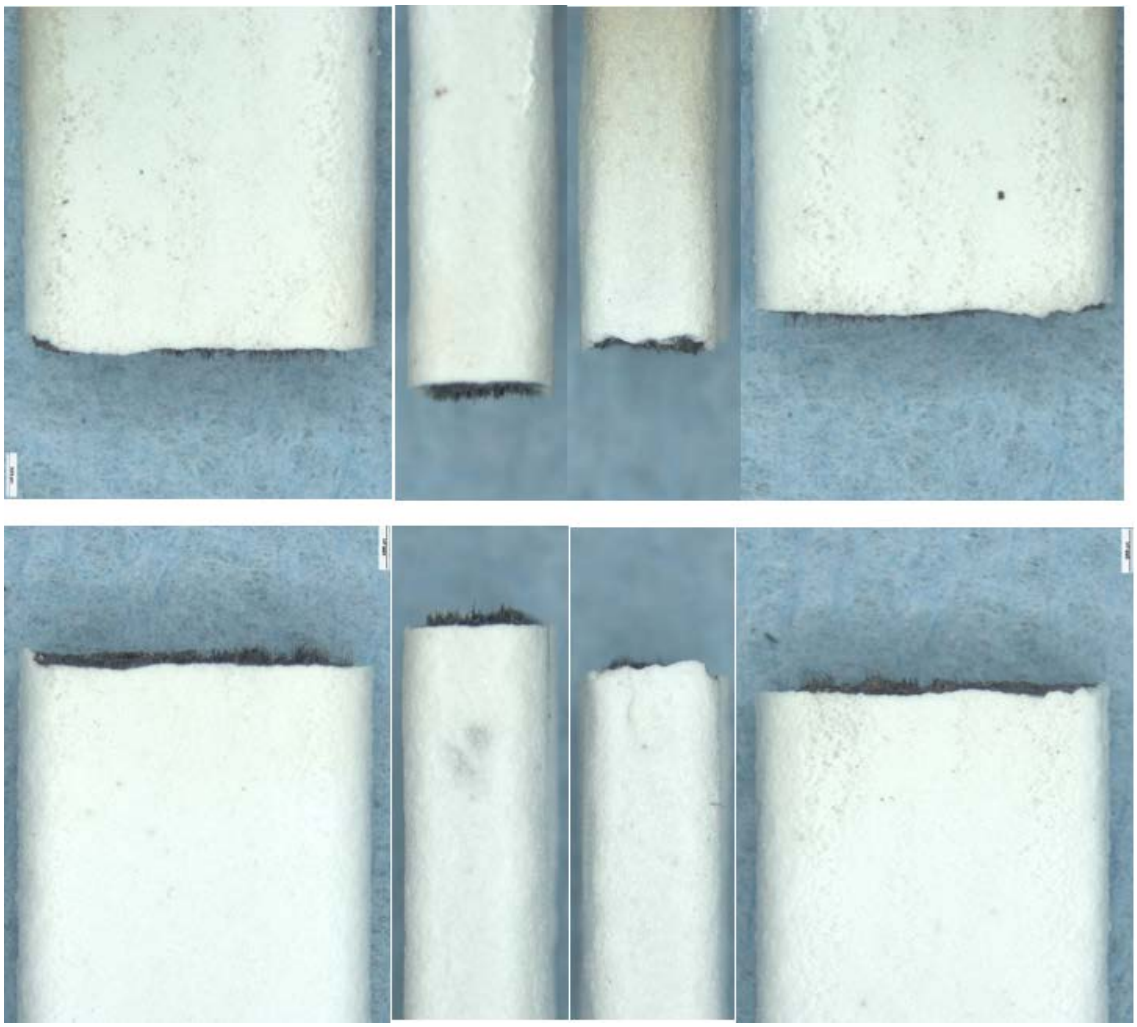

Figure A 10: Fracture surfaces of specimen P15006-12, tested in fatigue at 1200°C in steam.
σ_{max} = 130 MPa, N_f = 46,674 cycles

Appendix B – SEM Micrographs of Specimen Fracture Surfaces

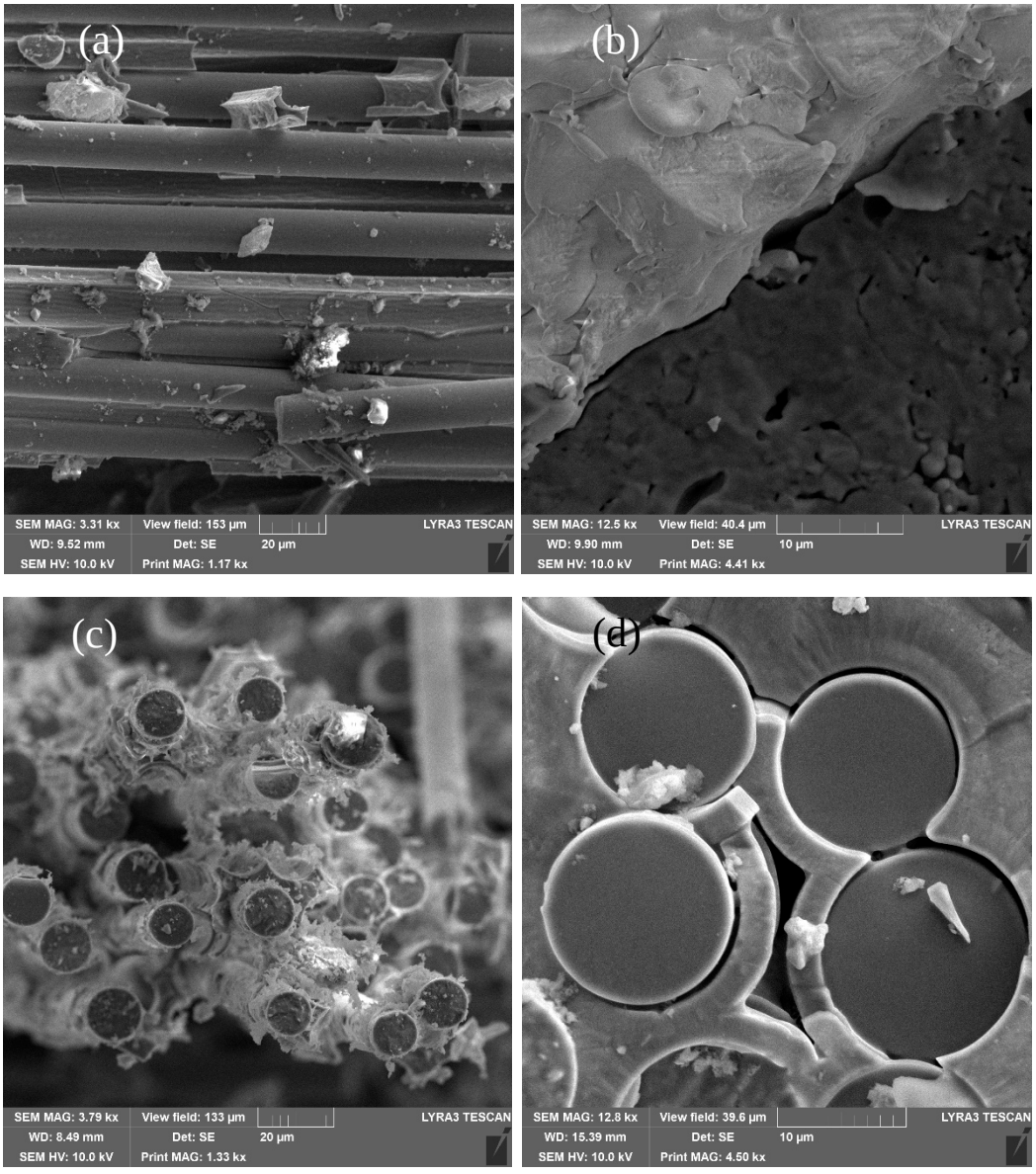

Figure B 1: Fracture surfaces of specimen P15001-12, tested in monotonic tension at 1200°C in air. (a) Transverse fiber tow fracture, (b) EBC topcoat and bond coat interface, (c) Fiber pullout, (d) Fiber fracture showing BN fiber coating, SiC CVI layer around fibers, weakly bonded interphase.

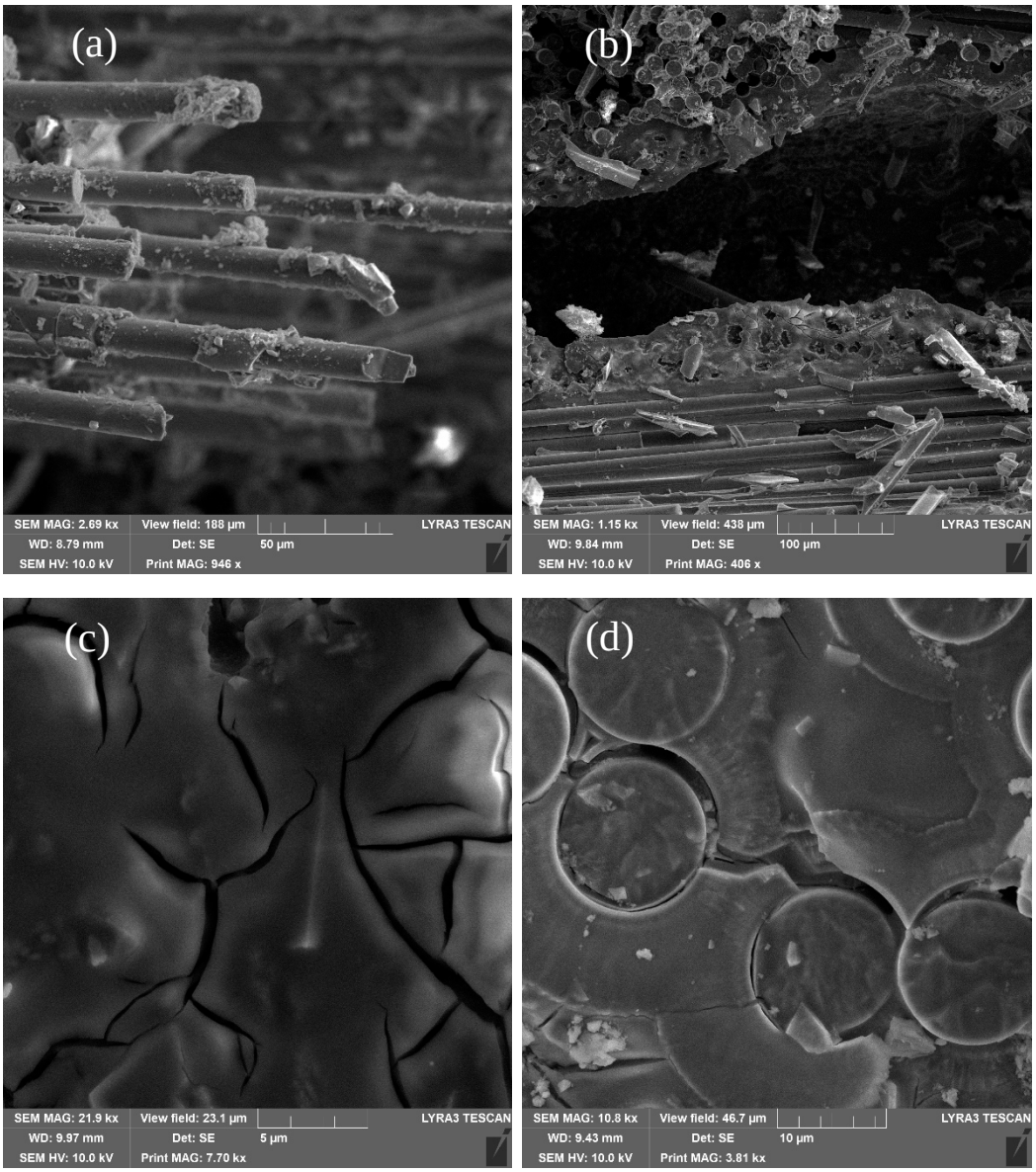

Figure B 2: Fracture surfaces of specimen P15001-12, tested in monotonic tension at 1200°C in air. (a) Transverse fiber tow fracture, (b) Internal flaw between fiber tows, (c) Matrix microcracking, (d) Fiber fracture with weakly bonded fibers and strongly bonded fibers.

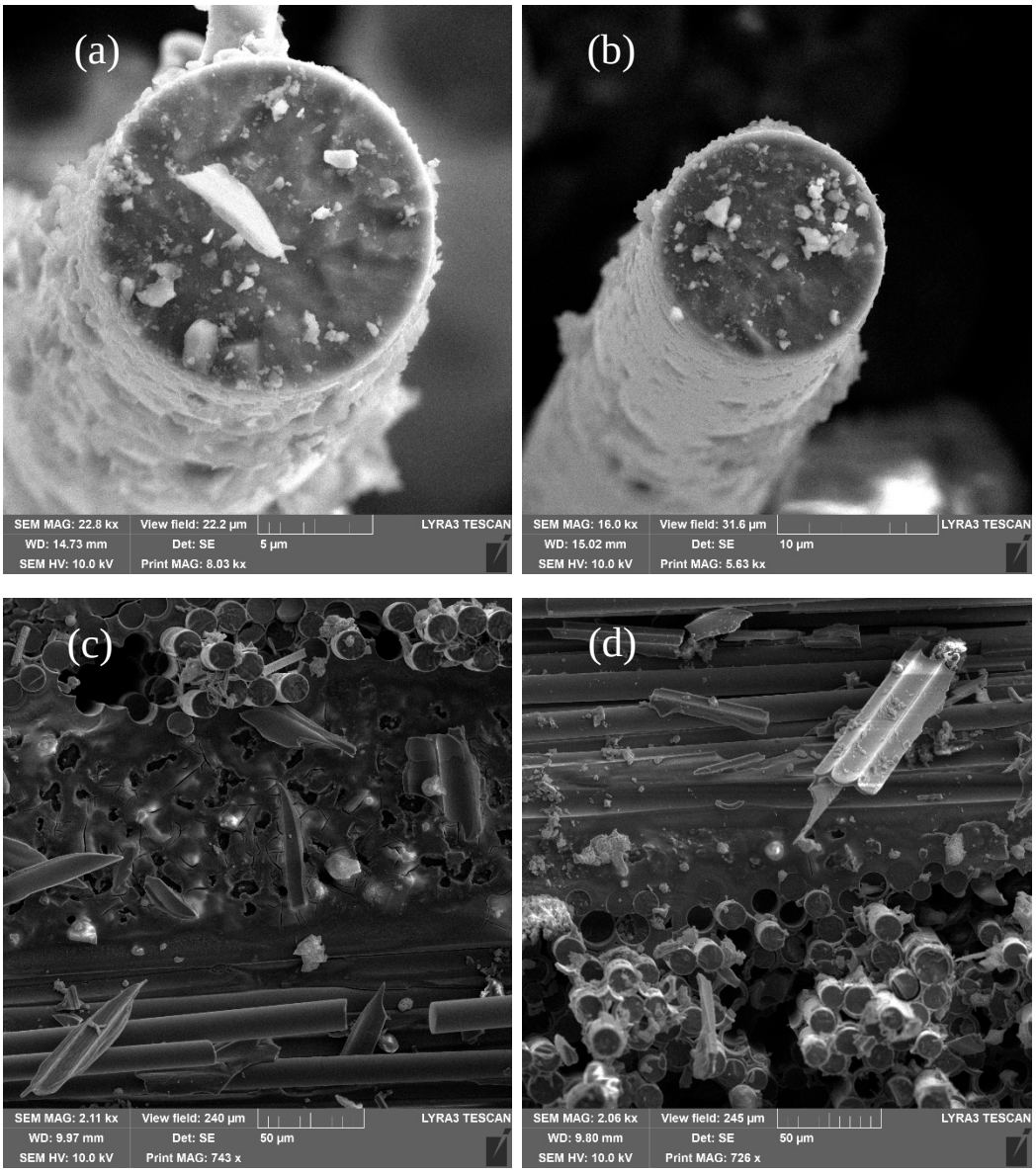

Figure B 3: Fracture surfaces of specimen P15001-12, tested in monotonic tension at 1200°C in air. (a) single fiber fracture showing BN fiber coating, (b) single fiber fracture, (c) matrix rich region between fiber tows, (d) basic topography of the fracture surface showing 0º and 90º fibers and fiber pullout.

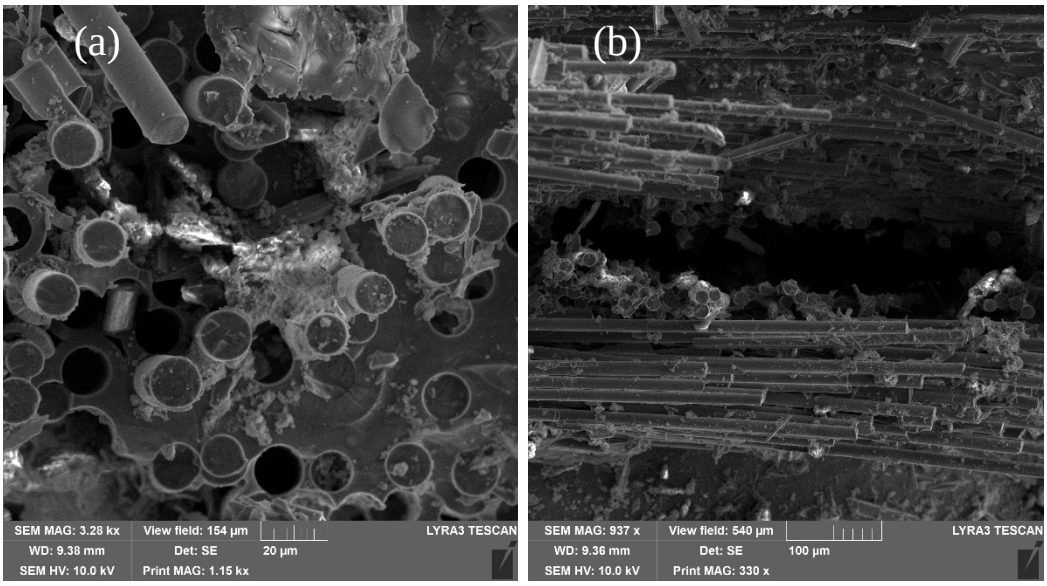

Figure B 4: Fracture surfaces of specimen P15001-12, tested in monotonic tension at 1200°C in air. (a) fiber pullout, (b) large internal processing flaw.

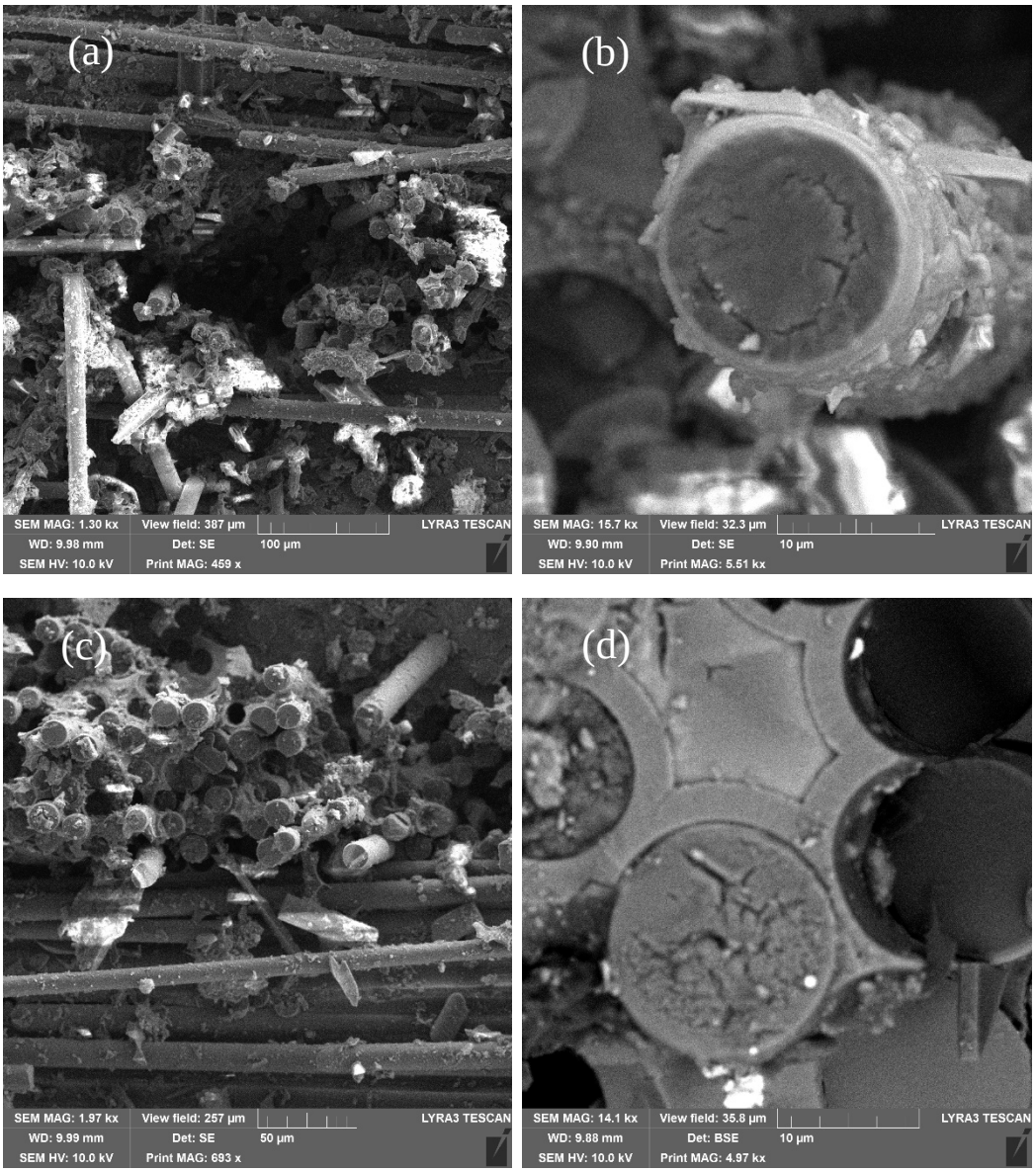

Figure B 5: Fracture surfaces of specimen P15005-3, tested in monotonic tension at 1200°C in air. (a) large internal processing flaw surrounded by fiber pullout, (b) single fiber fracture showing BN fiber coating, (c) lower magnification of fibrous fracture region, (d) fiber fracture, fiber pullout, successful matrix infiltration.

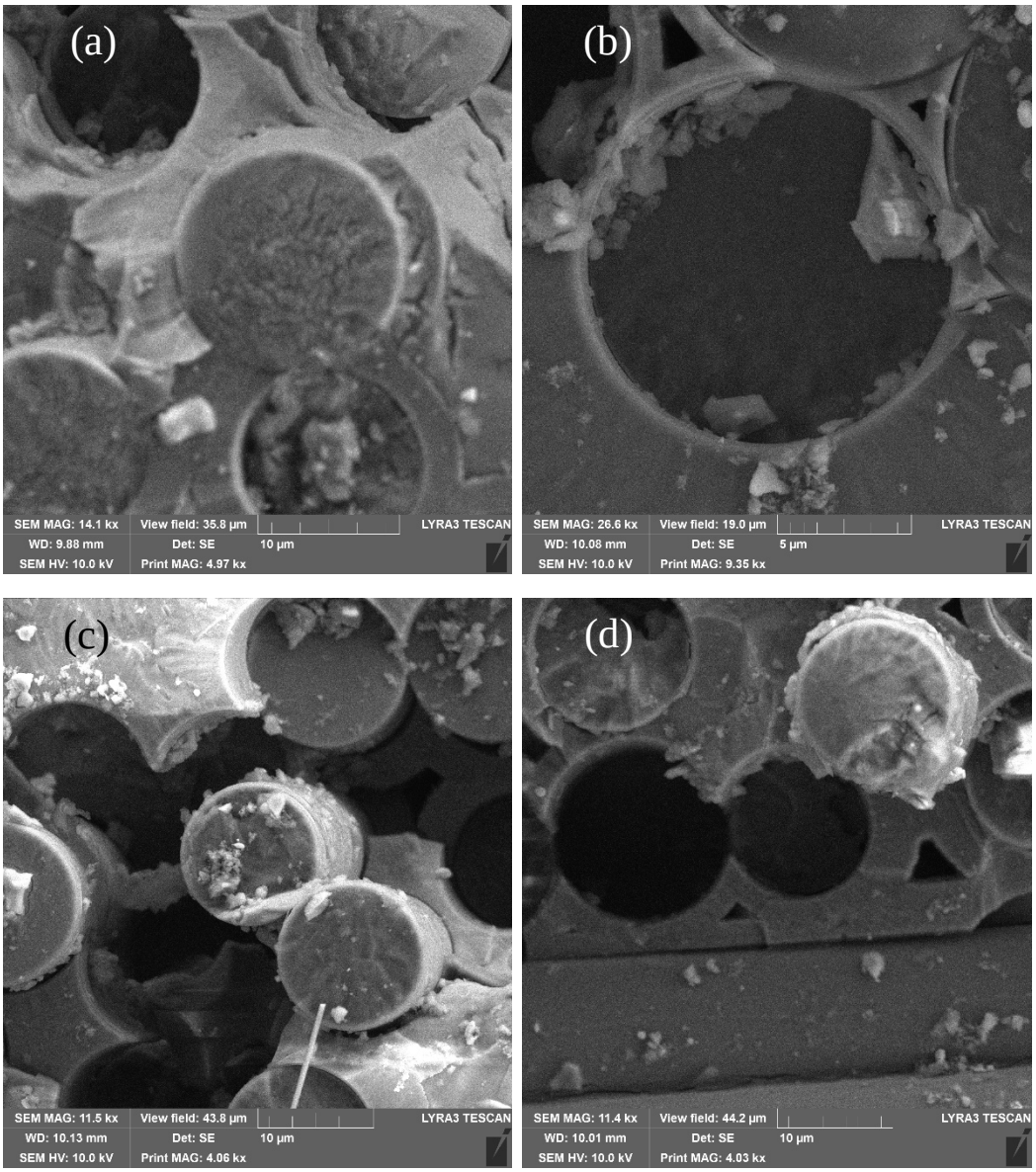

Figure B 6: Fracture surfaces of specimen P15005-3, tested in monotonic tension at 1200°C in air. (a) high magnification of non-oxidized fiber fracture, (b) single fiber pullout, (c) fiber pullout and fracture, (d) 0/90 fiber tow interface with fiber pullout.

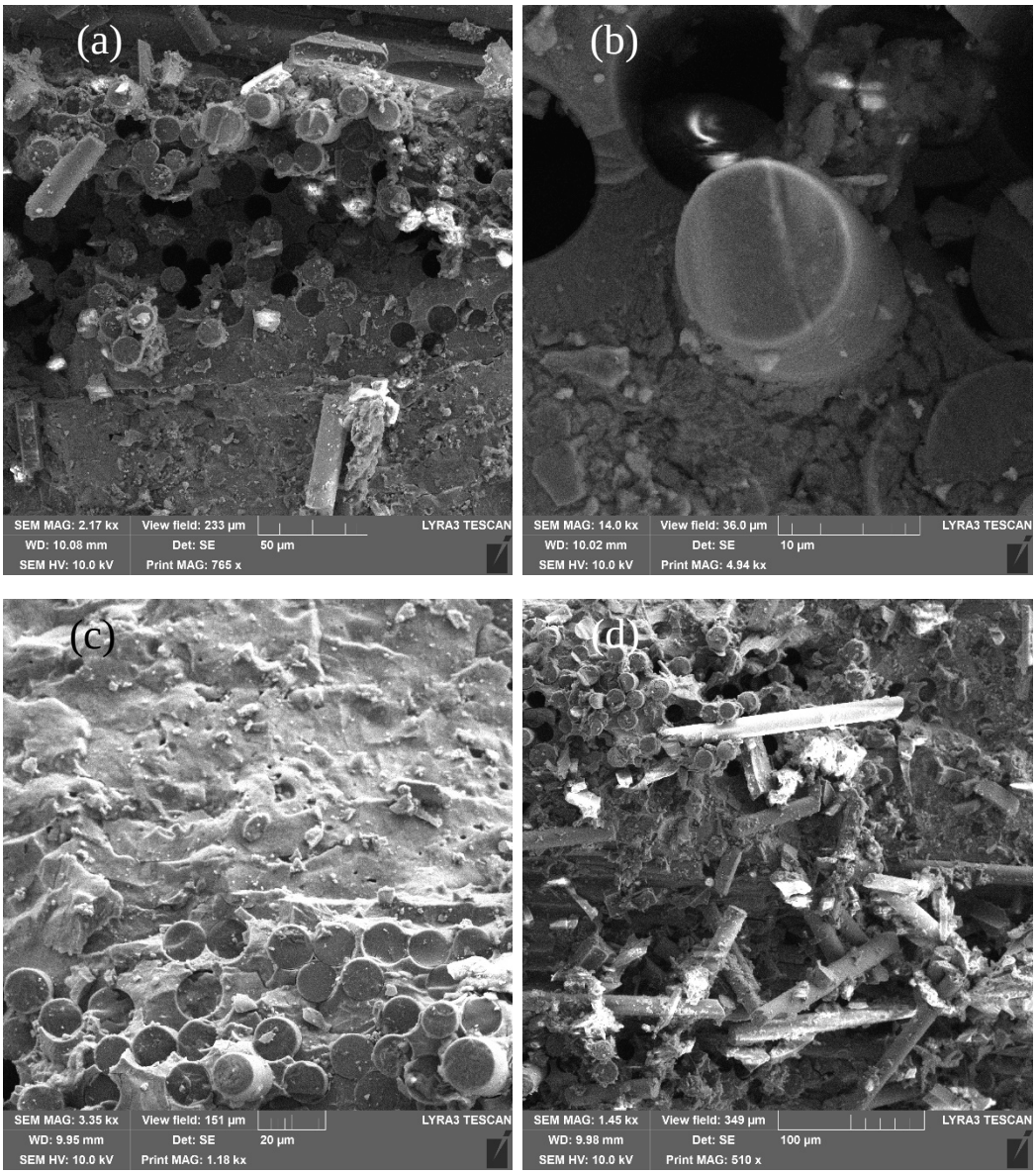

Figure B 7: Fracture surfaces of specimen P15005-3, tested in monotonic tension at 1200°C in air. (a) basic topography displaying fiber pullout, matrix rich region, and internal flaws, (b) single fiber fracture surface, (c) matrix rich region above well-bonded fibers, (d) matrix rich regions between fiber debris.

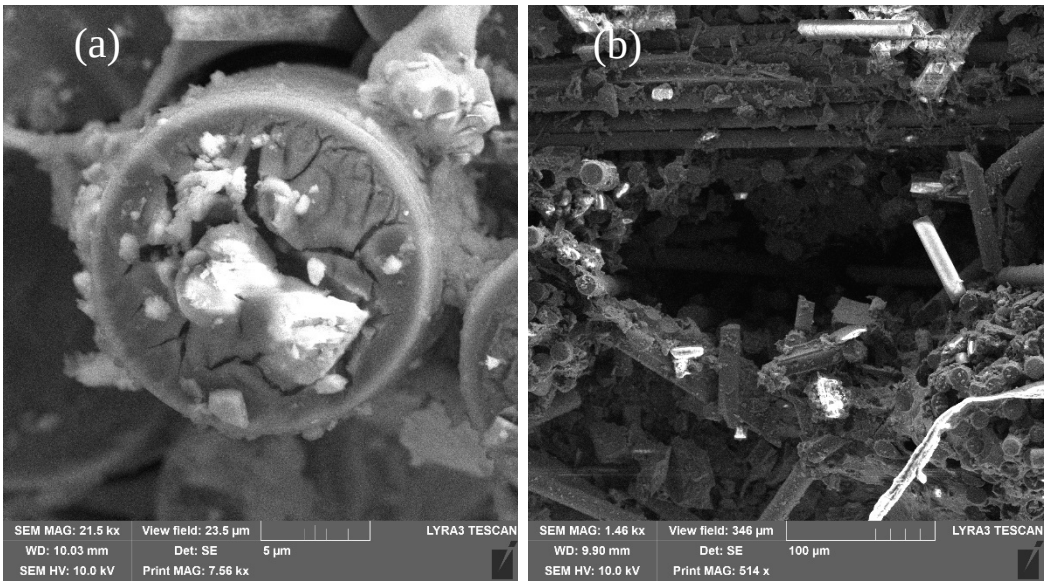

Figure B 8: Fracture surfaces of specimen P15005-3, tested in monotonic tension at 1200°C in air. (a) non-oxidized single fiber fracture, (b) large internal processing flaw.

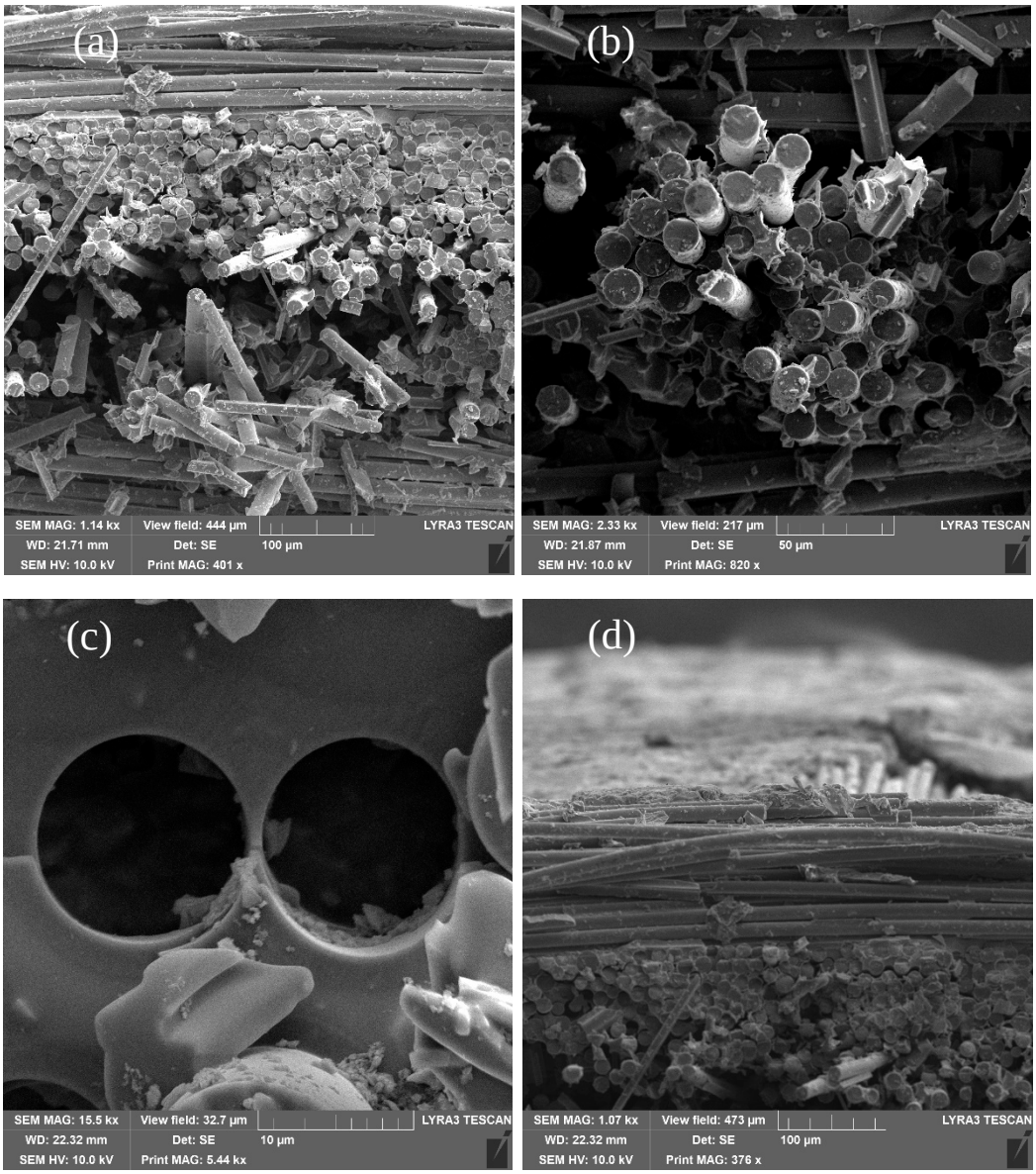

Figure B 9: Fracture surfaces of specimen P15006-4, tested in monotonic tension at 1200°C in air. (a) basic topography displaying fiber pullout, and internal flaws, (b) multiple fiber pullout, (c) fiber pullout, (d) grit blasting damage on upper surface of transverse fiber tow.

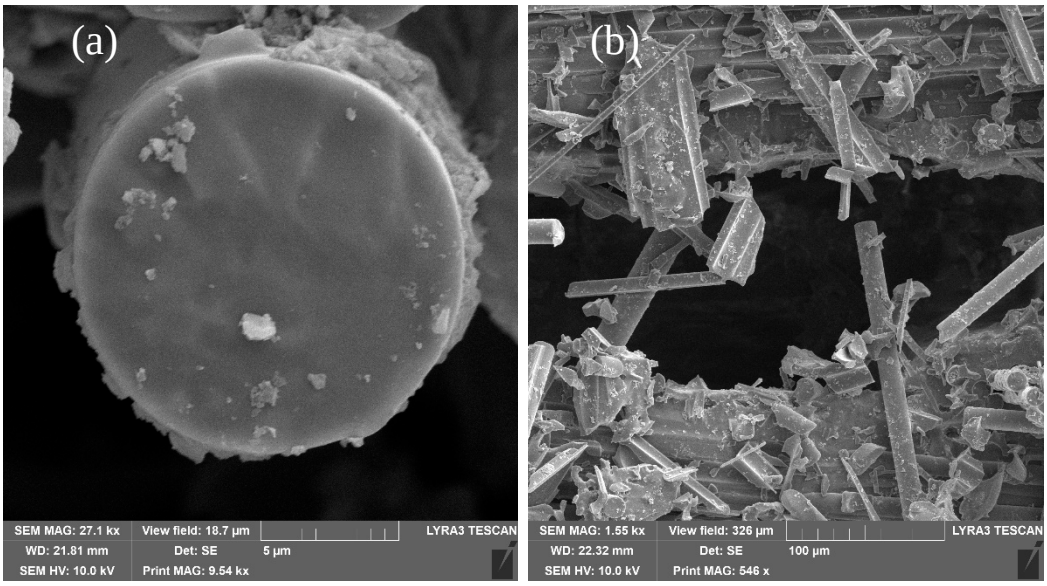

Figure B 10: Fracture surfaces of specimen P15006-4, tested in monotonic tension at 1200°C in air. (a) oxidized fiber fracture surface, fiber pullout, and internal flaws, (b) internal processing flaw.

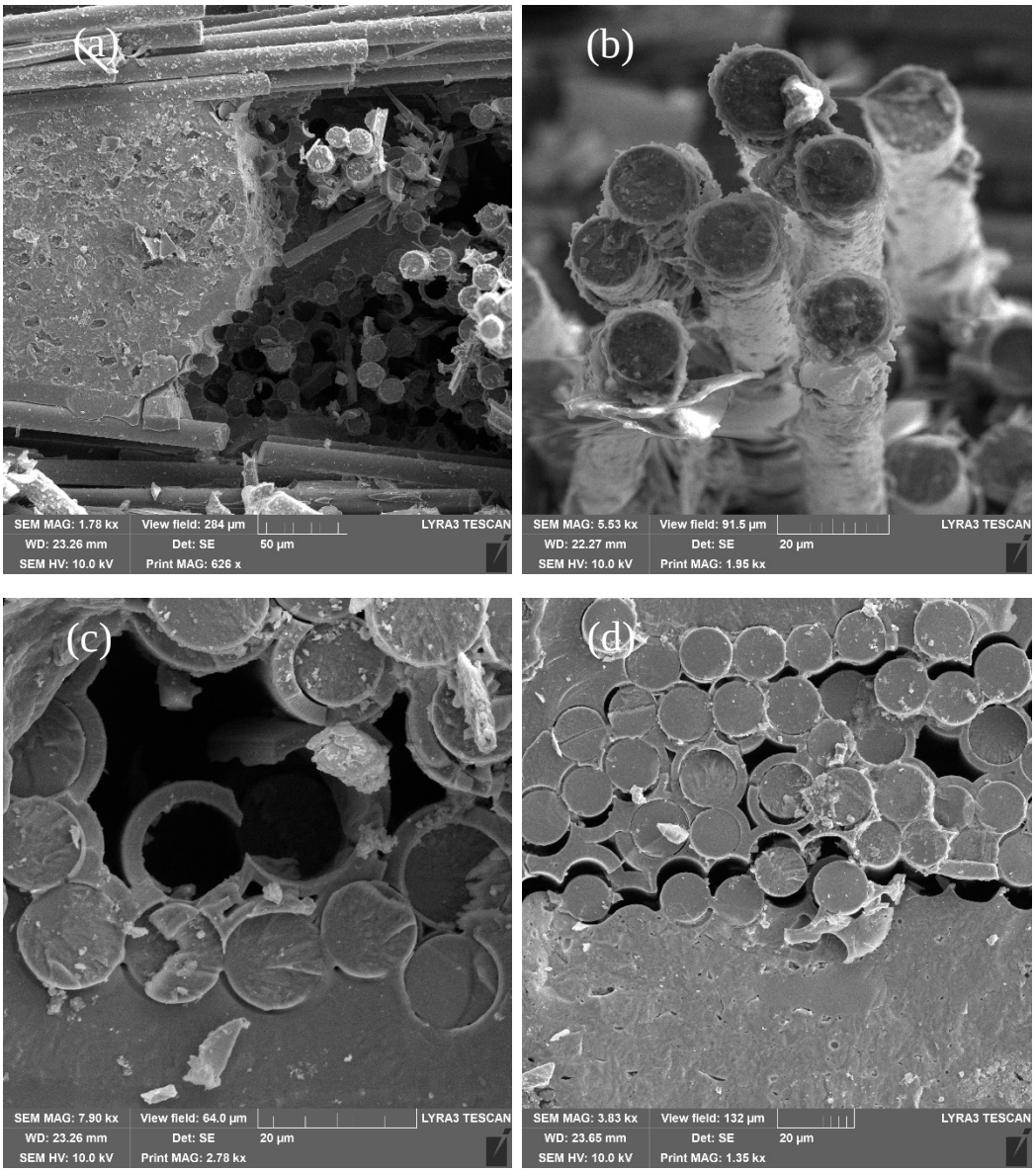

Figure B 11: Fracture surfaces of specimen P15001-13, tested in tension-tension fatigue at 1200°C in steam; σ_{max} = 140 MPa, N_f = 342 cycles. (a) large scale fiber pullout near matrix rich region, (b) fiber pullout, (c) fiber pullout and fiber to fiber bonding, (d) weakly bonded fibers separating from the SiC CVI layer above a matrix rich area, some fiber to fiber bonding present.

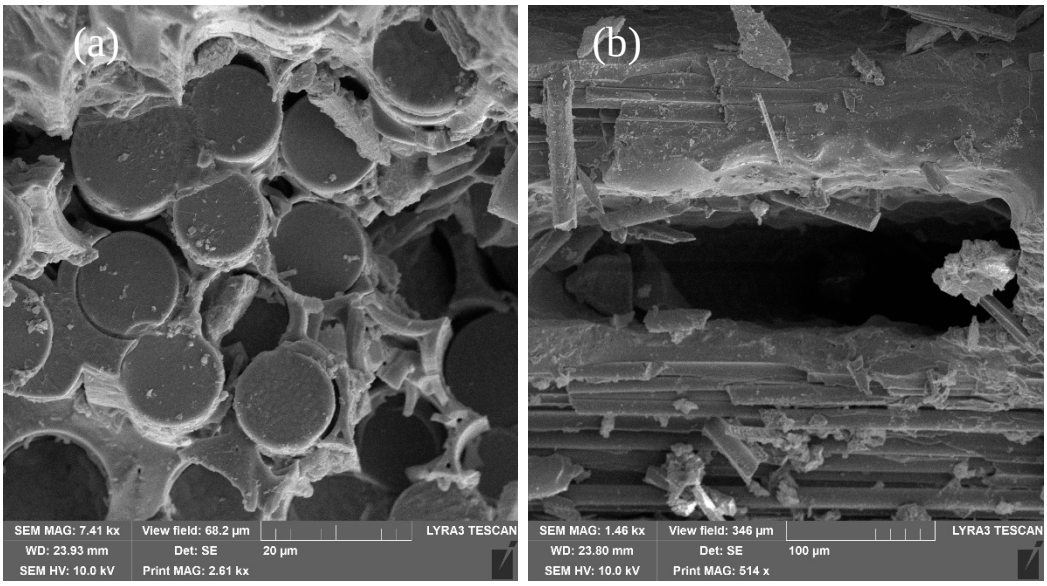

Figure B 12: Fracture surfaces of specimen P15001-13, tested in tension-tension fatigue at 1200°C in steam; σmax = 140 MPa, Nf = 342 cycles. (a) fiber bonding and fracture, (b) large internal processing flaw surrounded by oxidized glassy region.

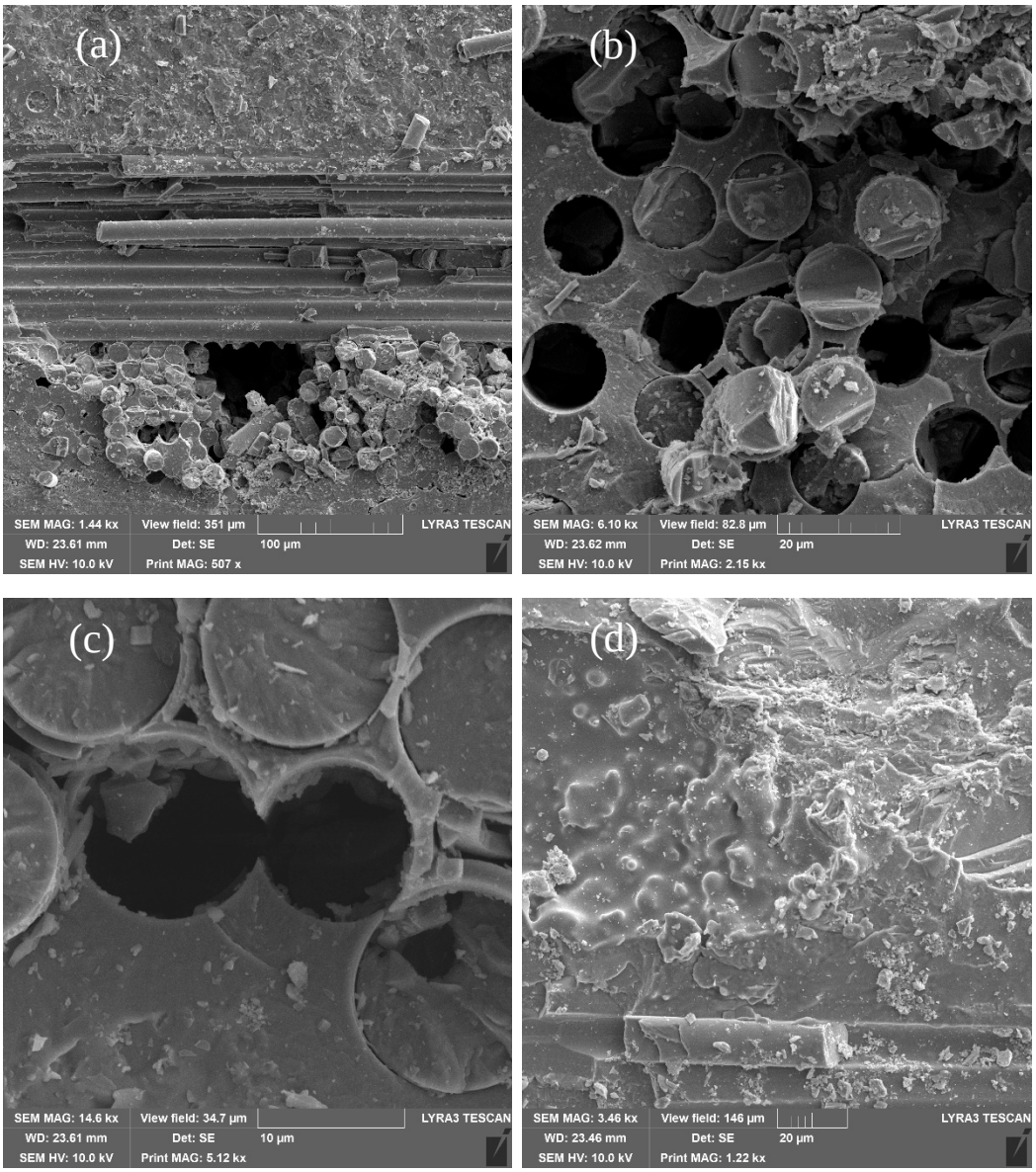

Figure B 13: Fracture surfaces of specimen P15002-7, tested in tension-tension fatigue at 1200°C in air; σmax = 130 MPa, Nf = 8,869 cycles. (a) matrix rich regions above and below fiber tows, multiple fiber pullout present (b) fiber pullout, (c) fiber pullout at higher magnification, (d) oxidized glassy matrix phase.

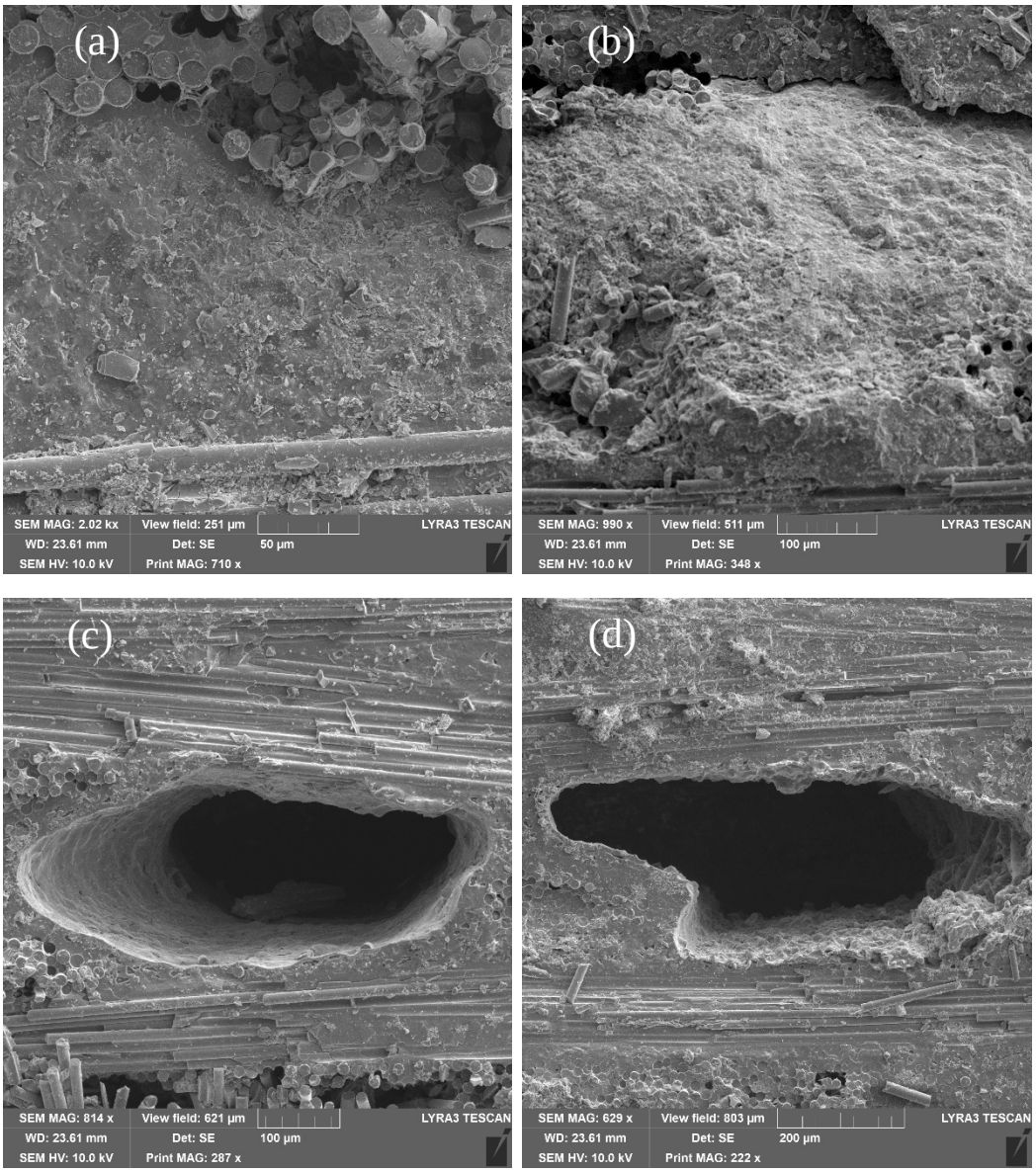

Figure B 14: Fracture surfaces of specimen P15002-7, tested in tension-tension fatigue at 1200°C in air; σmax = 130 MPa, Nf = 8,869 cycles. (a) (b) matrix rich regions between fiber tows, (c) (d) large internal processing flaws surrounded by fused fibers.

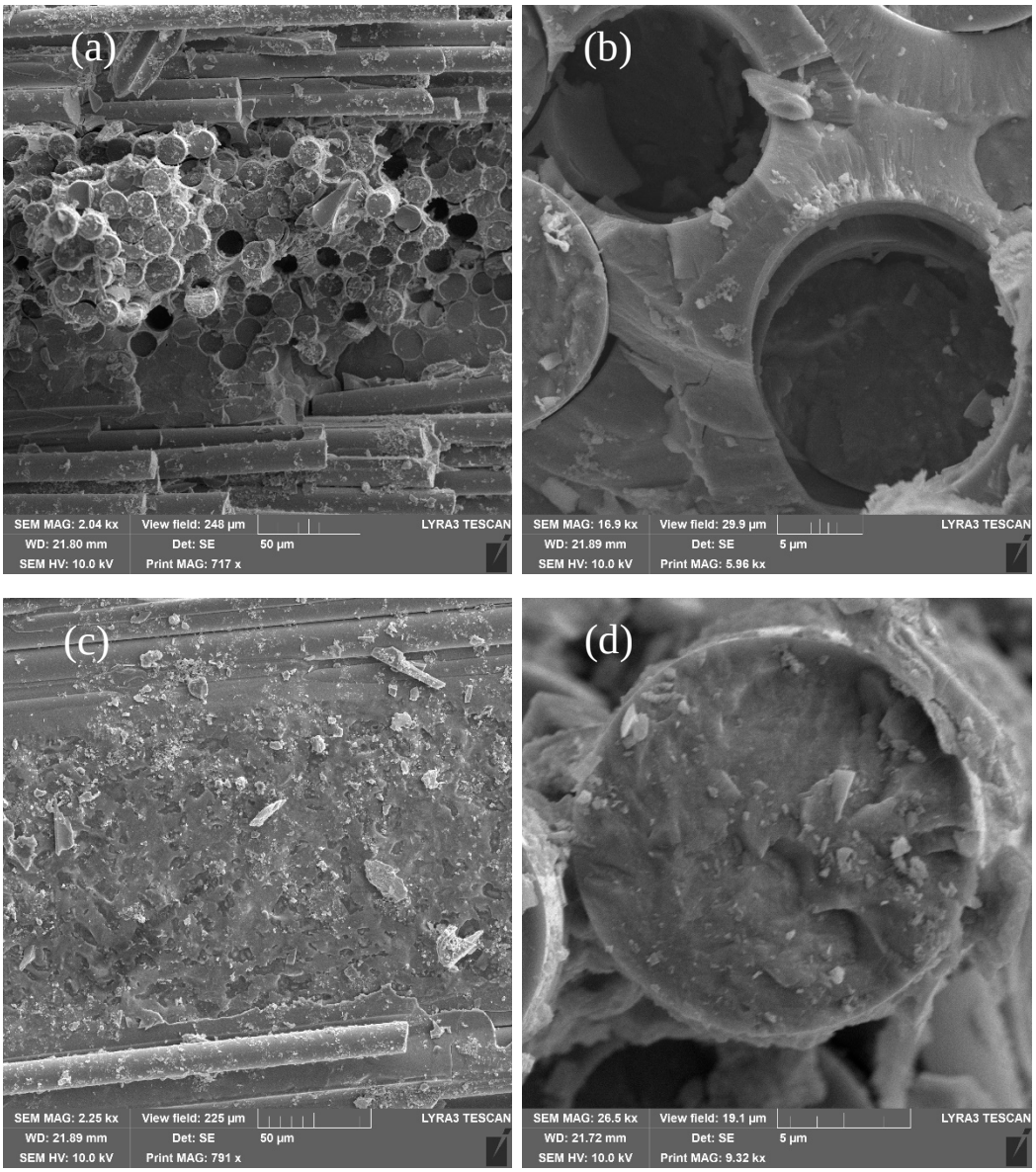

Figure B 15: Fracture surfaces of specimen P15004-7, tested in tension-tension fatigue at 1200°C in air; σmax = 140 MPa, Nf = 627 cycles. (a) minimal fiber pullout with fused fibers, (b) fiber pullout, (c) matrix rich region, (d) non-oxidized fiber fracture.

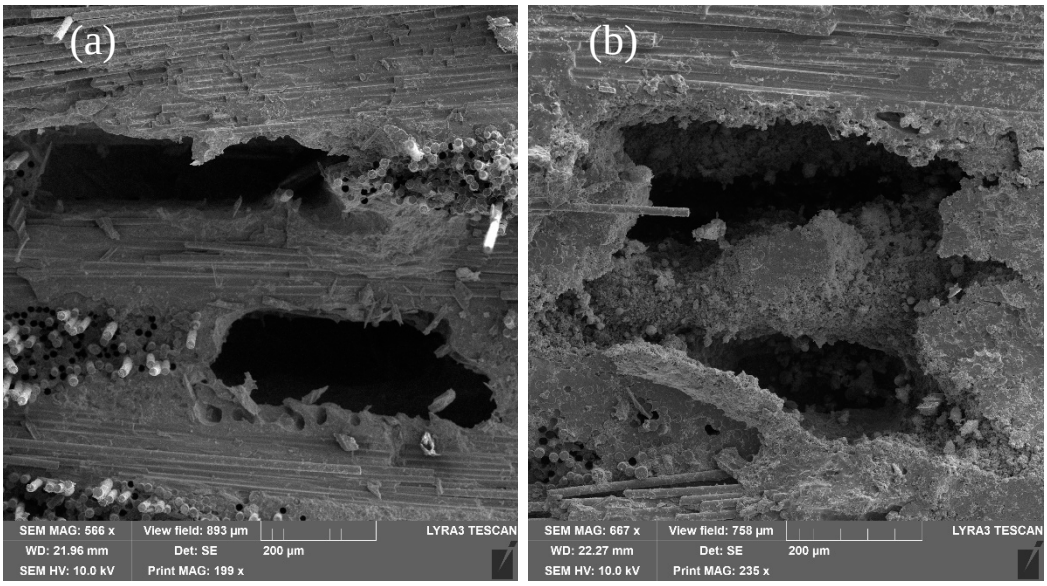

Figure B 16: Fracture surfaces of specimen P15004-7, tested in tension-tension fatigue at 1200°C in air; σmax = 140 MPa, Nf = 627 cycles. (a) (b) ~400 µm internal processing flaws.

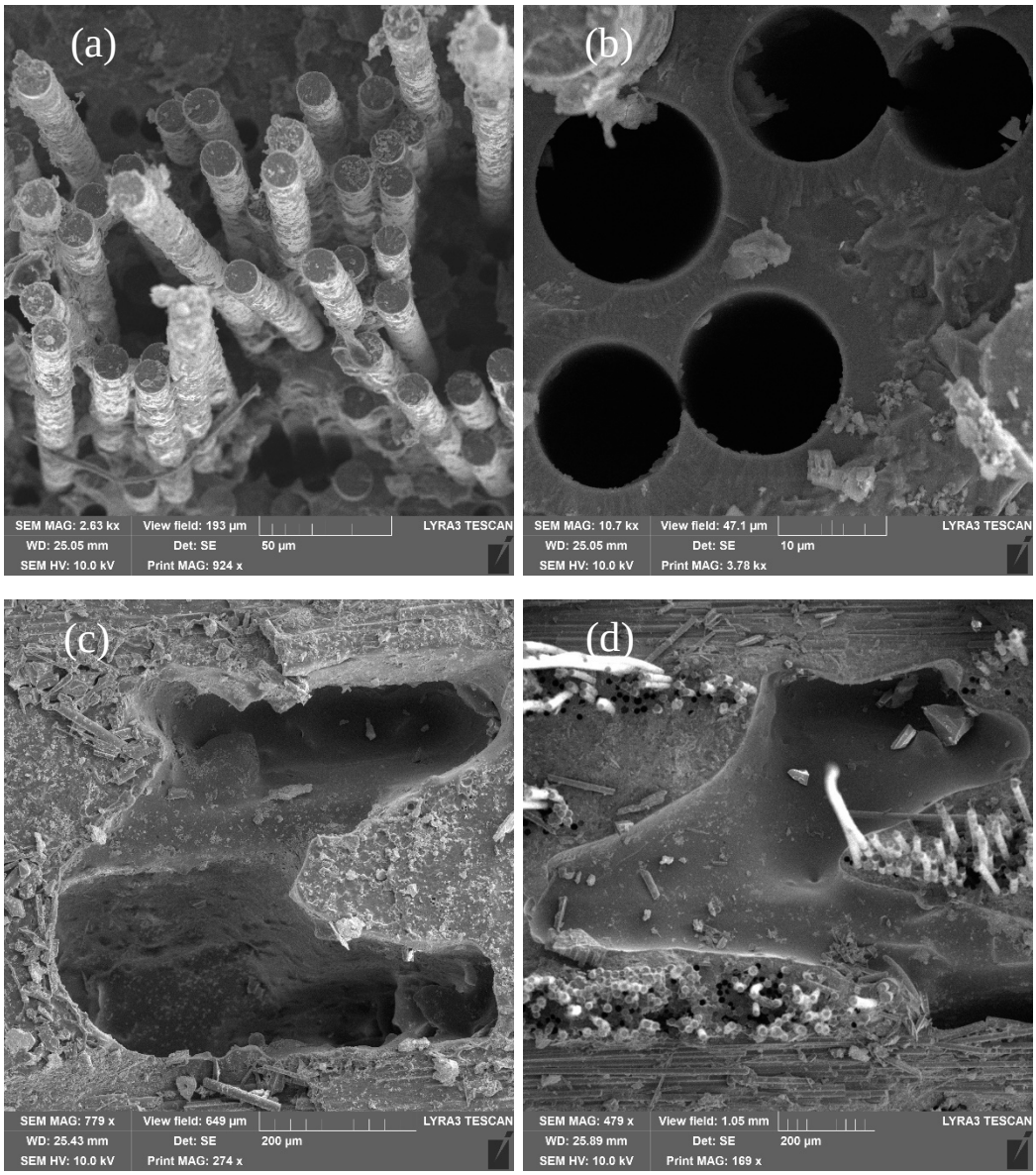

Figure B 17: Fracture surfaces of specimen P15005-4, tested in tension-tension fatigue at 1200°C in steam; σmax = 135 MPa, Nf = 19,781 cycles. (a) non-oxidized fiber pullout, (b) fiber pullout surrounded by intact matrix, (c) non-oxidized internal processing flaw inside matrix, (d) oxidized internal processing flaw surrounded by fiber pullout.

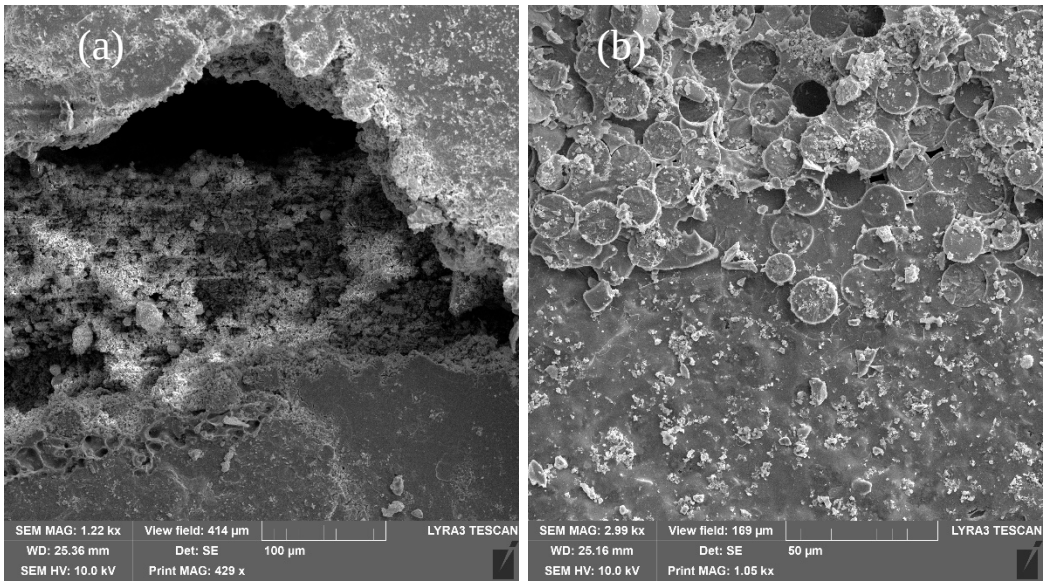

Figure B 18: Fracture surfaces of specimen P15005-4, tested in tension-tension fatigue at 1200°C in steam; σmax = 135 MPa, Nf = 19,781 cycles. (a) large internal flaw, (b) fused fibers above matrix rich region.

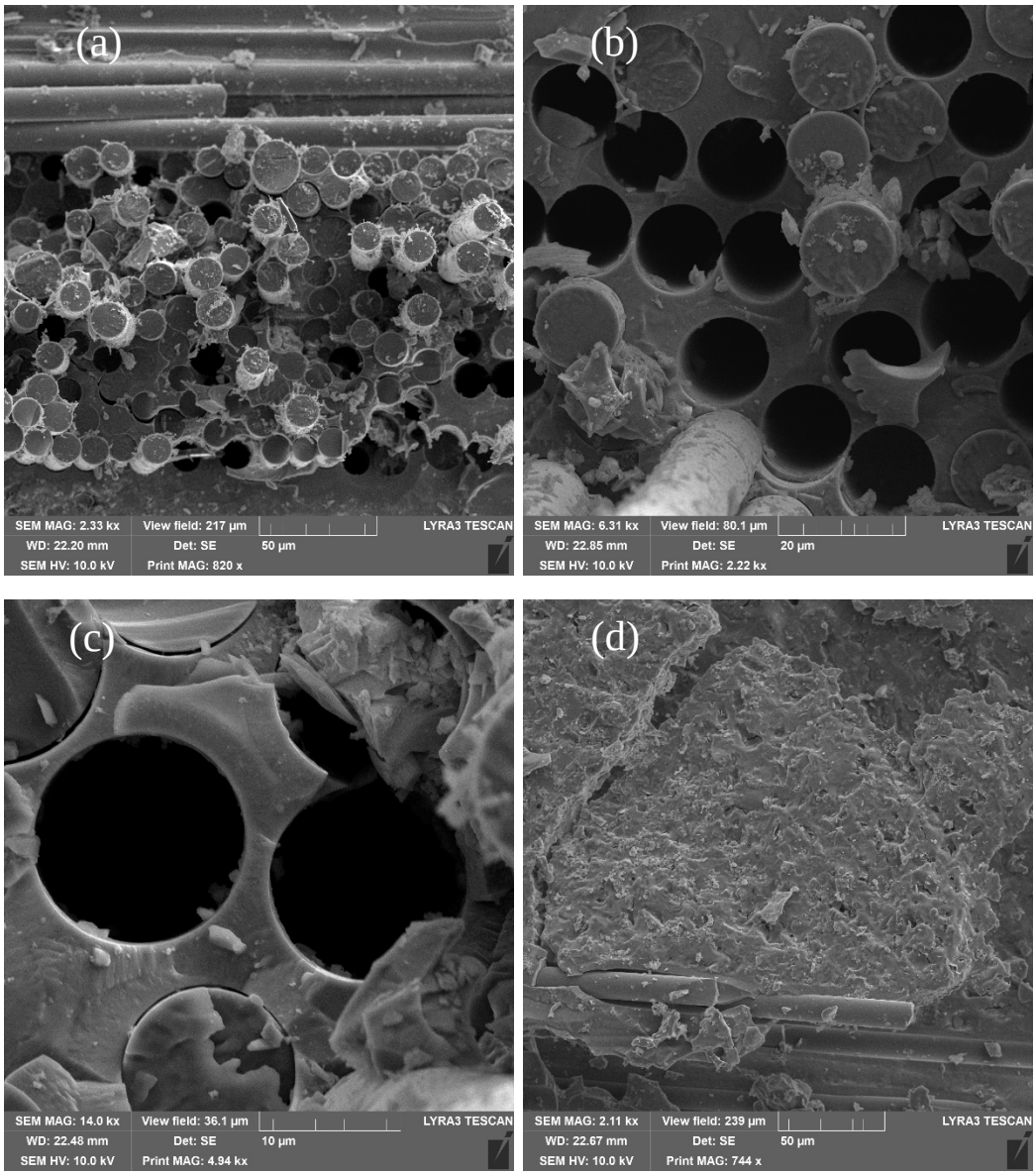

Figure B 19: Fracture surfaces of specimen P15005-5, tested in tension-tension fatigue at 1200°C in steam; σmax = 120 MPa, Nf > 200,000 cycles. (a) non-oxidized fiber pullout with some fiber to fiber bonding, (b) fiber pullout, (c) fiber pullout, (d) matrix rich region.

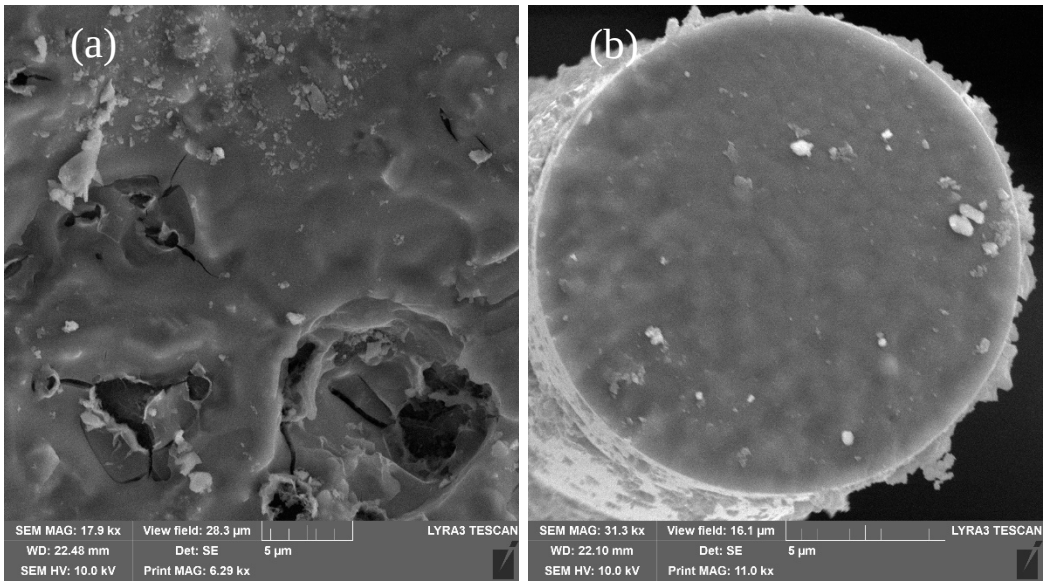

Figure B 20: Fracture surfaces of specimen P15005-5, tested in tension-tension fatigue at 1200°C in steam; σmax = 120 MPa, Nf > 200,000 cycles. (a) oxidized matrix region, (b) oxidized fiber fracture surface.

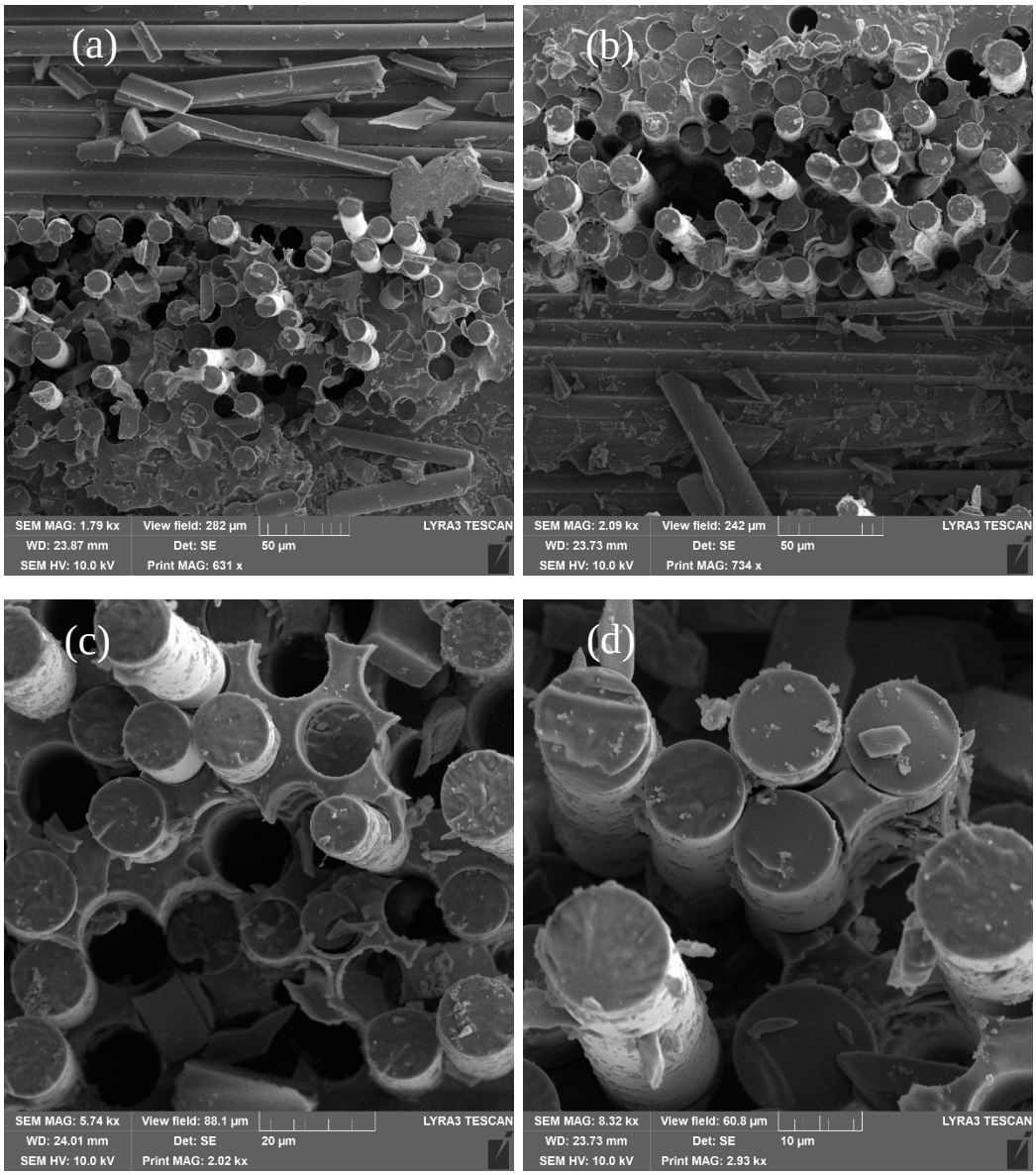

Figure B 21: Fracture surfaces of specimen P15006-13, tested in tension-tension fatigue at 1200°C in air; σmax = 110 MPa, Nf > 200,000 cycles. (a) non-oxidized fiber pullout, (b) non-oxidized fiber pullout with some fiber to fiber bonding, (c) fiber pullout, (d) oxidized and non-oxidized fiber fracture.

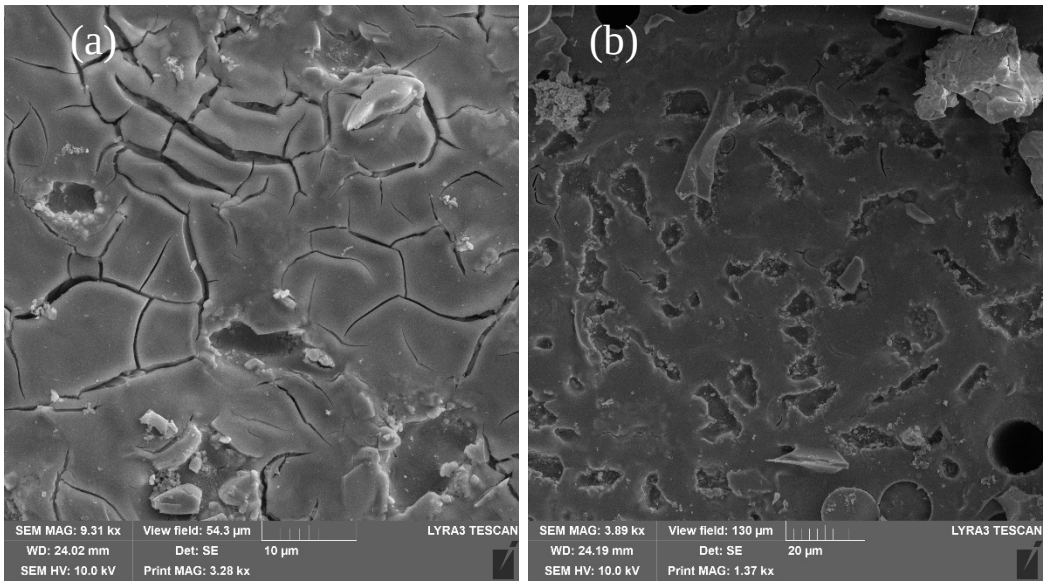

Figure B 22: Fracture surfaces of specimen P15006-13, tested in tension-tension fatigue at 1200°C in air; σmax = 110 MPa, Nf > 200,000 cycles. (a) high magnification of SiC matrix phase showing microcracks, (b) matrix region without microcracks.

Bibliography

[1] F. Breede and M. FrieB, "Development of Advanced CMC Materials for Dual-bell Rocket Nozzles," *Sonderforschungsbereich Transregio*, vol. 40, no. Annual Reports, 2009.

[2] "SiC-SiC Matrix Composite," Wikimedia Foundation, 4 June 2019. [Online]. Available: en.wikipedia.org/wiki/SiC%E2%80%93SiC_matrix_composite.

[3] "Silicon Carbide, SiC Ceramic Properties," Accuratus, 2013. [Online]. Available: accuratus.com/silicar.html. [Accessed 10 June 2019].

[4] K. K. Chawla, Ceramic Matrix Comosites, 2nd ed., Norwell, MA: Kluwer Academic Publishers, 2003.

[5] N. E. Dowling, Mechanical Behavior of Materials: Engineering Methods for Deformation, Fracture, and Fatigue, Pearson Education, Inc., 2019.

[6] S. Hampshire, Non-Oxide Technical and Engineering Ceramics, Elsevier Applied Science, 1986.

[7] T. L. Anderson, "Ceramics and ceramic composites," in *Fracture Mechanics: Fundamentals and Applications*, 3rd ed., Boca Raton, Florida: Taylor and Francis Group, 2005, pp. 282-290.

[8] K. L. Luthra, "Emerging Applications and Challenges in using Ceramics at General Electric," in *Ceramic Leadership Summit*, 2011.

[9] D. W. Richerson, Modern Ceramic Engineering: Properties, Processing, and Use in Design, 3rd ed., Boca Raton, Florida: CRC Press, 2006.

[10] W. D. Callister, Materials Science and Engineering: an Introduction, John Wiley, 2014.

[11] S. Chetty, "The Structural Integrity of Nanoclay Filled Epoxy Polymer under Cyclic Loading," MS Thesis, Durban University of Technology, 2017.

[12] D. Koch, "Microstructural modeling and thermomechanical properties," in *Ceramic Matrix Composites: Fiber Reinforced Ceramics and their Applications*, Weinstein, Wiley, 2008.

[13] S. Schmidt, S. Beyer, H. Knabe, H. Immich, R. Meistring and A. Gessler, "Advanced ceramic matrix composite materials for current and future propulsion technology applications," *Acta Astronautica*, vol. 55, no. 3-9, pp. 409-420, 2004.

[14] B. Budiansky, J. W. Hutchinson and A. G. Evans, "Matrix fracture in fiber-reinforced ceramics," *Journal of the Mechanics and Physics of Solids,* vol. 34, no. 2, pp. 167-189, 1986.

[15] A. Evans and D. B. Marshall, "The mechanical behavior of ceramic matrix composites," *Acta Metallurgica,* vol. 37, no. 10, pp. 2567-2583, 1989.

[16] M. Braginskya and C. P. Przybyla, "Simulation of crack propagation/deflection in ceramic matrix continuous fiber reinforced composites with weak interphase via the extended finite element method," *Composite Structures,* vol. 136, pp. 538-545, 2016.

[17] B. Heidenreich, "Carbon fibre reinforced sic materials based on melt infiltration," in *Ceramic Matrix Composites: Fiber Reinforced Ceramics and their Applications*, Weinheim, Wiley, 2008.

[18] K. N. Lee, "Environmental Barrier Coatings Enhance Performance of SiC/SiC Ceramic Matrix Composites," *American Ceramic Society Bulletin,* vol. 98, no. 3, pp. 46-53, 2019.

[19] K. N. Lee, D. S. Fox, R. C. Robinson and N. P. Bansal, "Environmental Barrier Coatings for Silicon-Based Ceramics," NASA Glenn Research Center.

[20] S. Ramasamy, S. N. Tewari, K. N. Lee, R. T. Bhatt and D. S. Fox, "Mullite-gadolinium silicate environmental barrier coatings for melt-infiltrated SiC/SiC composites," *Surface and Coatings Technology,* 2010.

[21] K. N. Lee, "Yb2Si2O7 Environmental barrier coatings with reduced bond coat oxidation rates via chemical modifications for long life," *Journal of the American Ceramic Society,* p. 1515, 2018.

[22] J. Delepasse, "Fatige Behavior of an Advanced SiC/SiC Composite with an Oxidation Inhibited Matrix at 1200C in Air and in Steam," MS Thesis, AFIT/GAE/ENY/10-M07, 2010.

[23] M. Lee, "Fatigue Behavior of an Advanced SiC/SiC Composite at 1300C in Air and Steam," MS Thesis, Air Force Institute of Technology, 2016.

[24] D. Christensen, "Fatigue Behavior of an Advanced SiC/SiC Composite at Elevated Temperature in Air and Steam," MS Thesis, AFIT/GAE/ENY/09-D02, 2009.

[25] N. Boucher, "Fatigue Behavior of an Advanced Melt-Infiltrated SiC/SiC Composite at 1200C in Air and in Steam," MS Thesis, AFIT/GAE/ENY/17-M242, 2017.

[26] H. E. Boyer, "Fatigue Testing," in *Atlas of Fatigue Curves,* ASM International, 2010.

[27] S. Minor, *Creep of Nextel 720/A Ceramic Matrix Composite with Laser Drilled Effusion Holes at 1200C in Air and in Steam.*

[28] G. Hoflinger, "Brief Introduction to Coating Technology for Electron Microscopy," Leica Microsystems, 28 August 2013. [Online]. Available: https://www.leica-microsystems.com/science-lab/brief-introduction-to-coating-technology-for-electron-microscopy/. [Accessed 19 November 2019].

[29] T. Anderson, Fracture Mechanics: Fundamentals and Applications, Boca Raton: Taylor and Francis Group, 2005.

[30] E. Lawrence, "ASTM D638: The Definitive Guide to Plastic Tensile Testing," [Online]. Available: www.instron.us/Testing%20Solutions/By%20Standard/ASTM/Multiple%20Testing%20Solutions/ASTM%20D638. [Accessed 10 June 2019].

REPORT DOCUMENTATION PAGE

Form Approved
OMB No. 0704-0188

1. REPORT DATE *(DD-MM-YYYY)*	2. REPORT TYPE	3. DATES COVERED *(From - To)*
03/26/2020	Master's Thesis	January 2019 - March 2020

4. TITLE AND SUBTITLE
Fatigue Behavior of an Advanced Melt-Infiltrated SiC/SiC Composite with Environmental Barrier Coating at 1200°C in Air and in Steam

5a. CONTRACT NUMBER

5b. GRANT NUMBER

5c. PROGRAM ELEMENT NUMBER

6. AUTHOR(S)
Williams, Thaddeus M.

5d. PROJECT NUMBER

5e. TASK NUMBER

5f. WORK UNIT NUMBER

7. PERFORMING ORGANIZATION NAME(S) AND ADDRESS(ES)
Air Force Institute of Technology
Graduate School of Engineering and Management (AFIT/EN)
2950 Hobson Way
Wright-Patterson AFB OH 45433-7765

8. PERFORMING ORGANIZATION REPORT NUMBER
AFIT-ENY-MS-20-M-287

9. SPONSORING/MONITORING AGENCY NAME(S) AND ADDRESS(ES)
Intentionally Left Blank

10. SPONSOR/MONITOR'S ACRONYM(S)

11. SPONSOR/MONITOR'S REPORT NUMBER(S)

12. DISTRIBUTION/AVAILABILITY STATEMENT
Distribution Statement A. Approved for Public Release; Distribution Unlimited

13. SUPPLEMENTARY NOTES
This work is declared a work of the U.S. Government and is not subject to copyright protection in the United States

14. ABSTRACT
Tension-tension fatigue performance of a SiC/SiC composite with an EBC was investigated at 1200°C in laboratory air and in steam. The composite has a melt-infiltrated (MI) matrix consolidated by combining CVI-SiC with SiC particulate slurry and molten Si infiltration and is reinforced with laminated woven SiC (Hi-Nicalon™) fibers. The EBC consists of a Si bond coat and an Ytterbium disilicate top coat. To assess the efficacy of the EBC, experimental results obtained for the coated composite are compared to the results obtained for a control composite without the EBC. The presence of the EBC had a moderately beneficial effect on the composite performance.

15. SUBJECT TERMS
Ceramic Matrix Composite, SiC/SiC, Environmental Barrier Coating, Fatigue

16. SECURITY CLASSIFICATION OF:			17. LIMITATION OF ABSTRACT	18. NUMBER OF PAGES	19a. NAME OF RESPONSIBLE PERSON
a. REPORT	b. ABSTRACT	c. THIS PAGE			Dr. Marina Ruggles-Wrenn, AFIT/ENY
U	U	U	UU	127	19b. TELEPHONE NUMBER *(Include area code)* 93725536364641marina.ruggles-wrenn@afit.edu